

論文 / 著書情報  
Article / Book Information

題目(和文)	フェムト秒電子・振動分光による光受容タンパク質および基本分子における超高速光異性化反応の研究
Title(English)	Ultrafast Photoisomerization in Photoreceptor Proteins and Fundamental Molecules Studied by Femtosecond Electronic and Vibrational Spectroscopy
著者(和文)	田原 進也
Author(English)	Shinya Tahara
出典(和文)	学位:博士(工学), 学位授与機関:東京工業大学, 報告番号:甲第10176号, 授与年月日:2016年3月26日, 学位の種別:課程博士, 審査員:大谷 弘之,田口 英樹,櫻井 実,上野 隆史,藤井 正明,田原 太平
Citation(English)	Degree:., Conferring organization: Tokyo Institute of Technology, Report number:甲第10176号, Conferred date:2016/3/26, Degree Type:Course doctor, Examiner:,,,,,
学位種別(和文)	博士論文
Type(English)	Doctoral Thesis

**Ultrafast Photoisomerization in Photoreceptor  
Proteins and Fundamental Molecules Studied by  
Femtosecond Electronic and Vibrational Spectroscopy**

**2016**

**Tokyo Institute of Technology**

**Shinya Tahara**

# Table of Contents

## Chapter 1: General Introduction

1.1 Importance of studying photoisomerization dynamics	1
1.2 Femtosecond time-resolved spectroscopy for direct observation of photoisomerization	4
1.3 This dissertation	5
1.4 References	7

## Chapter 2: Experimental

2.1 Femtosecond time-resolved spectroscopy	11
2.1.1 Femtosecond time-resolved absorption spectroscopy	12
2.1.2 Femtosecond time-resolved Kerr-gate fluorescence spectroscopy	15
2.1.3 Femtosecond stimulated Raman spectroscopy	18
2.2 References	21

## Chapter 3: Ultrafast Photoreactions of the All-*Trans* and 13-*Cis* *Anabaena* Sensory Rhodopsins Studied by Femtosecond Time-Resolved Kerr-Gate Fluorescence Spectroscopy

3.1 Introduction	23
3.2 Experimental methods	26
3.3 Results & Discussion	28

3.4 Conclusions 38

3.5 References 39

## **Chapter 4: Ultrafast Photoreaction Dynamics of Light-Driven Sodium-Ion-Pumping Rhodopsin KR2 Revealed by Femtosecond Time-Resolved Absorption Spectroscopy**

4.1 Introduction 41

4.2 Experimental methods 44

4.3 Results & Discussion 46

4.4 Conclusions 53

4.5 References 54

## **Chapter 5: pH-Dependent Formation of Reactive and Non-Reactive Excited States of Sodium-Ion-Pumping Rhodopsin KR2 Revealed by Femtosecond Time-Resolved Absorption Spectroscopy**

5.1 Introduction 57

5.2 Experimental methods 60

5.3 Results & Discussion 62

5.4 Conclusions 72

5.5 References 73

## **Chapter 6: Structural Dynamics of Barrierless Photoisomerization Revealed by Femtosecond Stimulated Raman Spectroscopy**

6.1 Introduction	75
6.2 Experimental methods	78
6.3 Results & Discussion	84
6.4 Conclusions	100
6.5 References	101
6.6 Appendix	104

## **Chapter 7: General Conclusions**      113

### **List of Publications**

### **Acknowledgements**

# Chapter 1: General Introduction

## 1.1 Importance of studying photoisomerization dynamics

*Trans-cis* and *cis-trans* isomerizations do not take place thermally in most of polyene molecules. This is because *trans* and *cis* isomers are separated by a high energy barrier, which prohibits interconversion between the *trans* and *cis* isomers at room temperature. However, with absorption of a photon, *trans* isomer readily isomerizes to *cis* isomer, while the *cis* isomer readily generates the *trans* isomer. This is the reaction that we call photoisomerization. To depict the difference between the thermal isomerization and photoisomerization in a physicochemical way, the schematic energy diagram of the *trans-cis* isomerization reactions of stilbene is shown in Figure 1.1. The figure clearly rationalizes the reason why *trans-cis* thermal isomerization does not occur, while  $S_1$  *trans*-stilbene, which is generated with absorption of UV light, isomerizes to *cis*-stilbene<sup>1, 2</sup>. Since the photoisomerization realizes the isomerization reaction that is unfavorable in a thermal reaction, it is utilized as a key process for designing materials having novel optical response. For example, the photoisomerization of an azobenzene derivative has been used for a polymer film which curls in response to the illumination<sup>3</sup>. The photoisomerization is important in both fundamental science and application, and hence its mechanism has attracted much attention<sup>4-9</sup>.

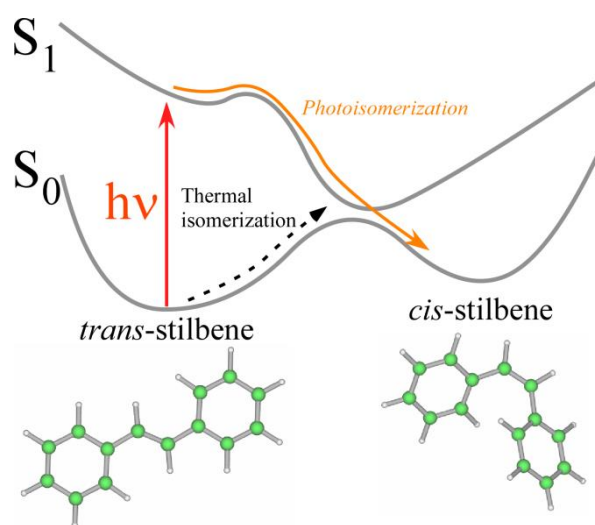


**Figure 1.1.** Schematic illustrations of the *trans-cis* thermal isomerization (broken black arrow) and photoisomerization (orange arrow) of stilbene.

Photoisomerization is important also in living organisms. For example, vision of higher animal is realized by the photoisomerization of the 11-*cis* retinal in rhodopsin<sup>10-12</sup> (Figure 1.2a), which exists in the membrane of rod outer segment in the retina<sup>13, 14</sup>. After absorption of a photon, the 11-*cis* retinal chromophore in the S<sub>1</sub> state undergoes isomerization to generate the all-*trans* form<sup>15, 16</sup>. Subsequently, the successive reaction involving several intermediates including the Metarhodopsin II, a long-lived intermediate, takes place<sup>17-21</sup> (Figure 1.2b). The Metarhodopsin II finally closes the cation channel by decreasing the level of cGMP through the cascade reaction, generating the neural signal<sup>22</sup>. The *cis-trans* photoisomerization of the 11-*cis* retinal is the essential first step in the physiological function of the rhodopsin, because it provides the energy required in all the cascade reactions involved in the visual process.

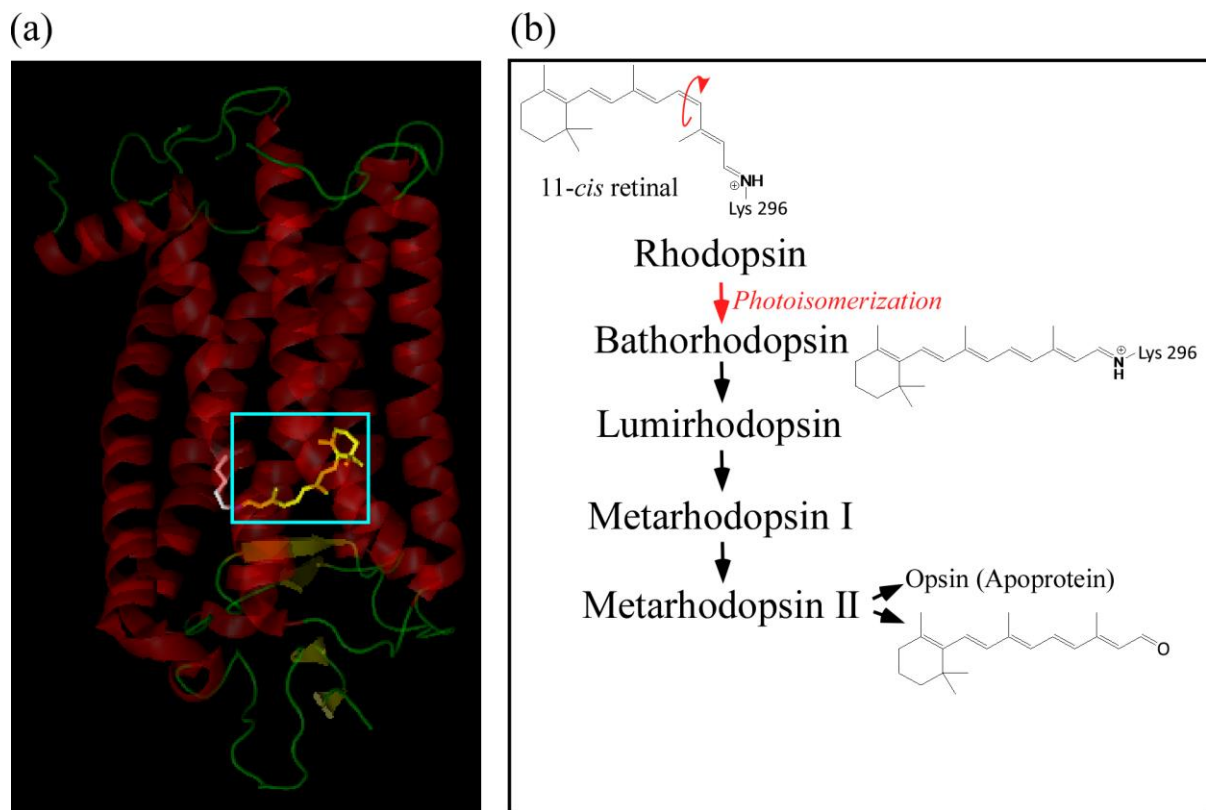


**Figure 1.2.** Schematic illustrations of (a) the molecular structure of bovine rhodopsin (PDB ID:1F88) and (b) the photoreaction and structures of the retinal chromophore.

Three decades ago, studies on the photoreaction of the rhodopsin started thanks to the developments and improvements of relevant technologies (e.g. detectors and light sources) that enable the photochemical researches of the photoreceptor proteins. In particular, highly stabilized ultrashort pulsed lasers became available<sup>23, 24</sup>, enabling us to investigate the primary process of the photoreceptor proteins<sup>25, 26</sup>. As for the rhodopsin, a spectroscopic study directly captured the deactivation of the excited state within 200 fs accompanied by the *cis-trans* isomerization of the retinal<sup>27</sup> (Figure 1.3). This deactivation is extremely fast compared with that of ordinary organic dyes whose excited-state lifetime are typically in the order of nanoseconds. Such an ultrafast deactivation realizes a photoisomerization with a high quantum yield ( $\sim 0.7$ ), yielding the Metarhodopsin II efficiently (see Figure 1.2b)<sup>28</sup>. After the discovery of the visual rhodopsin, it has been shown that the photoisomerization of the chromophore is utilized in many important photoreceptor proteins such as microbial rhodopsins and photoactive yellow proteins<sup>29, 30</sup>. In these photoreceptor proteins, the proteins guide the efficient photoisomerization reaction of the chromophore. For example, it has been shown that the all-*trans* retinal in bacteriorhodopsin, a microbial rhodopsin, isomerizes to the 13-*cis* retinal with a quantum yield of 0.64 while that in solution generates either 9-*cis*, 11-*cis* or 13-*cis* retinal by photoexcitation with a quantum yield of 0.2~0.06.<sup>31, 32</sup> The direct observation of the photoisomerization process can provide us knowledges how the proteins control the photoisomerization reaction, and thus it is important for protein science.

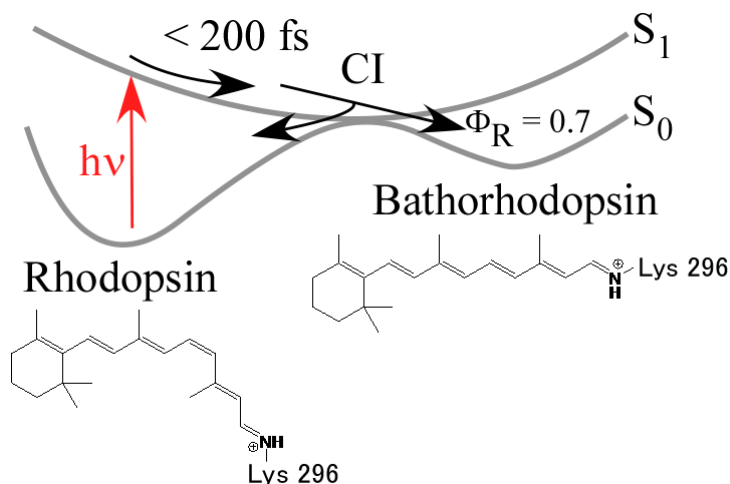


**Figure 1.3.** Schematic illustration of the photoisomerization dynamics of 11-*cis* retinal in rhodopsin. CI: conical intersection.

Considering a vast number of studies carried out for photoisomerization so far, one may think that the photoisomerization is a well-understood reaction. However, the microscopic mechanisms of the photoisomerization reaction still remain unclear. Especially,

1. In solution, *cis-trans* photoisomerizations have been found to be faster than *trans-cis* photoisomerizations in general based on the studies on various molecules such as stilbene<sup>2, 33</sup> and protonated retinal Schiff base (PRSB)<sup>34-36</sup>. However, *cis-trans* and *trans-cis* photoisomerization in the same protein matrix have not been studied well.
2. Recently, rhodopsins having unique functions, such as light-driven sodium ion pump rhodopsin, were found<sup>37, 38</sup>. However, the dynamics of these rhodopsins and mechanisms for their functions have not been fully elucidated. Especially, photoisomerization dynamics and mechanisms of these rhodopsins are unexplored.
3. The structural dynamics (including the structure in the transition state) during photoisomerization has been rarely observed. This is because the energy barrier exists in the pathway of most of the photoisomerization reaction, and the reaction rate is limited by the time required for reactants to obtain sufficient energy to surmount the energy barrier.

To address these issues, in this dissertation, ultrafast photoisomerization in chromophores in photoreceptor proteins and fundamental molecules were studied by femtosecond time-resolved spectroscopies.

## **1.2 Femtosecond time-resolved spectroscopies for direct observation of photoisomerization**

As exemplified by retinal photoisomerization in rhodopsins, photoisomerization reactions take place in the femto-to-picosecond time region. Therefore, femto/picosecond time-resolved measurements are necessary to examine the photoisomerization dynamics. Femtosecond time-resolved spectroscopy is a powerful tool for direct observation of the chemical events that take place on an ultrafast timescale. In fact, femtosecond time-resolved spectroscopy has been used to observe not only the dynamics of photoisomerizations<sup>1, 2, 39</sup> but also the dynamics of the

dissociation reactions,<sup>40, 41</sup> excited-state proton transfers,<sup>42</sup> and other ultrafast chemical reactions<sup>43</sup>.

Femtosecond time-resolved spectroscopy has been diversified. The most widely utilized techniques are femtosecond time-resolved absorption and fluorescence spectroscopies. These techniques are classified as femtosecond time-resolved “electronic” spectroscopy. This is because these techniques monitor the ultrafast dynamics through the change of the electronic spectral response. On the other hand, femtosecond time-resolved mid-IR absorption and Raman spectroscopies are classified as femtosecond time-resolved “vibrational” spectroscopy, because they provide us the information of the structural dynamics through the change of the vibrational spectrum. In this dissertation, both femtosecond time-resolved “electronic” and “vibrational” spectroscopies are used to study the photoisomerization dynamics.

### **1.3 This dissertation**

In this dissertation, the microscopic mechanisms of photoisomerization were studied using femtosecond spectroscopies. The construction and brief explanations of each chapter of this dissertation are as follows.

In this dissertation, several femtosecond time-resolved spectroscopic methods are utilized. In chapter 2, detailed explanation of these methods, including their advantages and comparisons, are described in chapter 2.

In solution, *cis-trans* photoisomerization proceeds faster than *trans-cis* photoisomerization in general. However, it is not directly shown yet that this is the case in protein matrix because a protein usually possesses only one isomer. To address this issue, in chapters 3, the photoisomerization dynamics in *Anabaena* sensory rhodopsin (ASR)<sup>38, 44</sup>, is investigated by femtosecond time-resolved fluorescence spectroscopy. ASR is a unique rhodopsin that can possess not only the all-*trans* retinal but also the 13-*cis* retinal in the same protein cavity<sup>45</sup>. Therefore, the dynamics of the all-*trans* and 13-*cis* retinals can be directly compared. Based on the fluorescence data, it is shown how the difference in conformation of the chromophore (all-*trans* vs. 13-*cis*) affects the photoisomerization rate.

In chapter 4, the photoisomerization of the all-*trans* retinal in KR2<sup>38</sup>, which is a newly discovered light-driven sodium ion pump, is investigated by femtosecond time-resolved absorption spectroscopy. Based on the obtained data and comparison between previously reported crystal structures of KR2<sup>46</sup> and all-*trans* bacteriorhodopsin<sup>47</sup>, it is shown that the difference in the Schiff base structure affects the photoisomerization rate of the all-*trans* retinal chromophore. In the following chapter 5, pH dependence of the reactivity of KR2 is investigated by femtosecond time-resolved absorption spectroscopy. It is known that Asp 116, the counterion of the PRSB, is protonated at pH below 7<sup>38</sup>, disrupting the interaction between the Asp 116 and the PRSB. The obtained femtosecond absorption data clearly show that the interaction between the PRSB and the Asp116 clearly affects the photoisomerization of PRSB in KR2.

Direct observation of the structural dynamics during photoisomerization is still very rare. In chapter 6, aiming at full tracking of the structural dynamics of a “isomerizing” molecule which gradually twists in the excited state, the structural dynamics of the barrierless photoisomerization of a cyanine dye<sup>48</sup> is investigated by femtosecond stimulated Raman spectroscopy. Based on the Raman pump wavelength dependence of the obtained time-resolved Raman spectra, the structural changes during photoisomerization were successfully visualized.

## 1.4 References

- (1) Hochstrasser, R. M., Picosecond Processes in the Isomerism of Stilbenes. *Pure Appl. Chem.* **1980**, *52*, 2683-2691.
- (2) Rothenberger, G.; Negus, D. K.; Hochstrasser, R. M., Solvent Influence on Photoisomerization Dynamics. *J. Chem. Phys.* **1983**, *79*, 5360-5367.
- (3) Yu, Y.; Nakano, M.; Ikeda, T., Photomechanics: Directed Bending of a Polymer Film by Light. *Nature* **2003**, *425*, 145-145.
- (4) Rau, H.; Lueddecke, E., On the Rotation-Inversion Controversy on Photoisomerization of Azobenzenes. Experimental Proof of Inversion. *J. Am. Chem. Soc.* **1982**, *104*, 1616-1620.
- (5) RAU, H., Further Evidence for Rotation in the N-Pi\* and Inversion in the N-Pi\* Photoisomerization of Azobenzenes. *J. Photochem.* **1984**, 221-225.
- (6) Tatsuya Fujino, S. Y. A., and Tahei Tahara, Femtosecond Time-Resolved Fluorescence Study of Photoisomerization of Trans-Azobenzene. *J. Phys. Chem. A* **2001**, *105*, 8123-8129.
- (7) Kropf, A.; Hubbard, R., The Photoisomerization of Retinal. *Photochem. Photobiol.* **1970**, *12*, 249-260.
- (8) Menger, E. L.; Kliger, D. S., Photoisomerization Kinetics of 11-Cis-Retinal, Its Schiff Base, and Its Protonated Schiff Base. *J. Am. Chem. Soc.* **1976**, *98*, 3975-3979.
- (9) Veyret, B.; Davis, S. G.; Yoshida, M.; Weiss, K., Laser Photolysis Study of the Photoisomerization of Retinals. *J. Am. Chem. Soc.* **1978**, *100*, 3283-3290.
- (10) Palczewski, K.; Kumasaka, T.; Hori, T.; Behnke, C. A.; Motoshima, H.; Fox, B. A.; Trong, I. L.; Teller, D. C.; Okada, T.; Stenkamp, R. E.; Yamamoto, M.; Miyano, M., Crystal Structure of Rhodopsin: A G Protein-Coupled Receptor. *Science* **2000**, *289*, 739-745.
- (11) Okada, T.; Sugihara, M.; Bondar, A.-N.; Elstner, M.; Entel, P.; Buss, V., The Retinal Conformation and Its Environment in Rhodopsin in Light of a New 2.2 Å Crystal Structure. *J. Mol. Biol.* **2004**, *342*, 571-583.
- (12) Kumauchi, M.; Ebrey, T. G., Visual Pigments as Photoreceptors. In *Handbook of Photosensory Receptors*, Wiley-VCH Verlag GmbH & Co. KGaA: 2005; pp 43-76.
- (13) Rhodopsin in the Rod Outer Segment Plasma Membrane. *J. Cell Biol.* **1976**, *69*, 29-42.
- (14) Abdulaev, N. G.; Ridge, K. D., Structural and Functional Aspects of the Mammalian Rod-Cell Photoreceptor Rhodopsin. In *Handbook of Photosensory Receptors*, Wiley-VCH Verlag GmbH & Co. KGaA: 2005; pp 77-92.
- (15) Bagley, K. A.; Balogh-Nair, V.; Croteau, A. A.; Dollinger, G.; Ebrey, T. G.; Eisenstein, L.; Hong, M. K.; Nakanishi, K.; Vittitow, J., Fourier-Transform Infrared Difference Spectroscopy of Rhodopsin and Its Photoproducts at Low Temperature. *Biochemistry* **1985**, *24*, 6055-6071.
- (16) Barry Honig, A. D. G., Uri Dinur, and Thomas G. Ebrey, Visual-Pigment Spectra: Implications of the Protonation of the Retinal Schiff Base. *Biochemistry* **1976**, *15*, 4593-4599.
- (17) Penn, R. D.; Hagins, W. A., Kinetics of the Photocurrent of Retinal Rods. *Biophys. J.* **12**, 1073-1094.

- (18) Baylor, D. A.; Lamb, T. D.; Yau, K. W., The Membrane Current of Single Rod Outer Segments. *J. Physiol.* **1979**, *288*, 589-611.
- (19) Ganter, U. M.; Gaertner, W.; Siebert, F., Rhodopsin-Lumirhodopsin Phototransition of Bovine Rhodopsin Investigated by Fourier Transform Infrared Difference Spectroscopy. *Biochemistry* **1988**, *27*, 7480-7488.
- (20) Matthews, R. G.; Hubbard, R.; Brown, P. K.; Wald, G., Tautomeric Forms of Metarhodopsin. *J. Gen. Phys.* **1963**, *47*, 215-240.
- (21) Kuwata, O.; Yuan, C.; Misra, S.; Govindjee, R.; Ebrey, T. G., Kinetics and Ph Dependence of Light-Induced Deprotonation of the Schiff Base of Rhodopsin: Possible Coupling to Proton Uptake and Formation of the Active Form of Meta II. *Biochemistry (Moscow)* **2001**, *66*, 1283-1299.
- (22) Stryer, L., Visual Excitation and Recovery. *J. Biol. Chem.* **1991**, *266*, 10711-10714.
- (23) Shirakawa, A.; Sakane, I.; Kobayashi, T., Pulse-Front-Matched Optical Parametric Amplification for Sub-10-Fs Pulse Generation Tunable in the Visible and near Infrared. *Opt. Lett.* **1998**, *23*, 1292-1294.
- (24) Cerullo, G.; Nisoli, M.; Stagira, S.; De Silvestri, S., Sub-8-Fs Pulses from an Ultrabroadband Optical Parametric Amplifier in the Visible. *Opt. Lett.* **1998**, *23*, 1283-1285.
- (25) Polli, D.; Luer, L.; Cerullo, G., High-Time-Resolution Pump-Probe System with Broadband Detection for the Study of Time-Domain Vibrational Dynamics. *Rev. Sci. Instrum.* **2007**, *78*, 103108.
- (26) Kobayashi, T.; Saito, T.; Ohtani, H., Real-Time Spectroscopy of Transition States in Bacteriorhodopsin During Retinal Isomerization. *Nature* **2001**, *414*, 531-534.
- (27) Schoenlein, R.; Peteanu, L.; Mathies, R.; Shank, C., The First Step in Vision: Femtosecond Isomerization of Rhodopsin. *Science* **1991**, *254*, 412-415.
- (28) Dartnall, H. J. A., The Photosensitivities of Visual Pigments in the Presence of Hydroxylamine. *Vis. Res.* **1968**, *8*, 339-358.
- (29) van der Horst, M. A.; Hellingwerf, K. J., Photoreceptor Proteins, "Star Actors of Modern Times": A Review of the Functional Dynamics in the Structure of Representative Members of Six Different Photoreceptor Families. *Acc. Chem. Res.* **2004**, *37*, 13-20.
- (30) Sundström, V., Femtobiology. *Annu. Rev. Phys. Chem.* **2008**, *59*, 53-77.
- (31) Tittor, J.; Oesterhelt, D., The Quantum Yield of Bacteriorhodopsin. *FEBS Lett.* **1990**, *263*, 269-273.
- (32) Koyama, Y.; Kubo, K.; Komori, M.; Yasuda, H.; Mukai, Y., Effect of Protonation on the Isomerization Properties of N-Butylamine Schiff Base of Isomeric Retinal as Revealed by Direct Hplc Analyses: Selection of Isomerization Pathways by Retinal Proteins. *Photochem. Photobiol.* **1991**, *54*, 433-443.
- (33) Doany, F. E.; Hochstrasser, R. M.; Greene, B. I.; Millard, R. R., Femtosecond-Resolved Ground-State Recovery of Cis-Stilbene in Solution. *Chem. Phys. Lett.* **1985**, *118*, 1-5.
- (34) Logunov, S. L.; Song, L.; El-Sayed, M. A., Excited-State Dynamics of a Protonated Retinal Schiff Base in Solution. *J. Phys. Chem.* **1996**, *100*, 18586-18591.

- (35) Kandori, H.; Katsuta, Y.; Ito, M.; Sasabe, H., Femtosecond Fluorescence Study of the Rhodopsin Chromophore in Solution. *J. Am. Chem. Soc.* **1995**, *117*, 2669-2670.
- (36) Sasabe, H. K. a. H., Excited-State Dynamics of a Protonated Schiff Base of All-Trans Retinal in Methanol Probed by Femtosecond Fluorescence Measurement. *Chem. Phys. Lett.* **1993**, 126-172.
- (37) Inoue, K.; Koua, F. H. M.; Kato, Y.; Abe-Yoshizumi, R.; Kandori, H., Spectroscopic Study of a Light-Driven Chloride Ion Pump from Marine Bacteria. *J. Phys. Chem. B* **2014**, *118*, 11190-11199.
- (38) Inoue, K.; Ono, H.; Abe-Yoshizumi, R.; Yoshizawa, S.; Ito, H.; Kogure, K.; Kandori, H., A Light-Driven Sodium Ion Pump in Marine Bacteria. *Nat. Commun.* **2013**, *4*, 1678.
- (39) Nuss, M. C.; Zinth, W.; Kaiser, W.; Kölling, E.; Oesterhelt, D., Femtosecond Spectroscopy of the First Events of the Photochemical Cycle in Bacteriorhodopsin. *Chem. Phys. Lett.* **1985**, *117*, 1-7.
- (40) Rose, T. S.; Rosker, M. J.; Zewail, A. H., Femtosecond Real - Time Probing of Reactions. Iv. The Reactions of Alkali Halides. *J. Chem. Phys.* **1989**, *91*, 7415-7436.
- (41) Rose, T. S.; Rosker, M. J.; Zewail, A. H., Femtosecond Real - Time Observation of Wave Packet Oscillations (Resonance) in Dissociation Reactions. *J. Chem. Phys.* **1988**, *88*, 6672-6673.
- (42) Chattoraj, M.; King, B. A.; Bublitz, G. U.; Boxer, S. G., Ultra-Fast Excited State Dynamics in Green Fluorescent Protein: Multiple States and Proton Transfer. *Proc. Natl. Acad. Sci. USA* **1996**, *93*, 8362-8367.
- (43) Fujisawa, T.; Takeuchi, S.; Masuda, S.; Tahara, T., Signaling-State Formation Mechanism of a Bluf Protein Papb from the Purple Bacterium Rhodospseudomonas Palustris Studied by Femtosecond Time-Resolved Absorption Spectroscopy. *J. Phys. Chem. B* **2014**, *118*, 14761-14773.
- (44) Jung, K.-H.; Trivedi, V. D.; Spudich, J. L., Demonstration of a Sensory Rhodopsin in Eubacteria. *Mol. Microbiol.* **2003**, *47*, 1513-1522.
- (45) Vogeley, L.; Sineshchekov, O. A.; Trivedi, V. D.; Sasaki, J.; Spudich, J. L.; Luecke, H., Anabaena Sensory Rhodopsin: A Photochromic Color Sensor at 2.0 Å. *Science* **2004**, *306*, 1390-1393.
- (46) Kato, H. E.; Inoue, K.; Abe-Yoshizumi, R.; Kato, Y.; Ono, H.; Konno, M.; Hososhima, S.; Ishizuka, T.; Hoque, M. R.; Kunitomo, H.; Ito, J.; Yoshizawa, S.; Yamashita, K.; Takemoto, M.; Nishizawa, T.; Taniguchi, R.; Kogure, K.; Maturana, A. D.; Iino, Y.; Yawo, H.; Ishitani, R.; Kandori, H.; Nureki, O., Structural Basis for Na<sup>+</sup> Transport Mechanism by a Light-Driven Na<sup>+</sup> Pump. *Nature* **2015**, *521*, 48-53.
- (47) Schobert, B.; Cupp-Vickery, J.; Hornak, V.; Smith, S. O.; Lanyi, J. K., Crystallographic Structure of the K Intermediate of Bacteriorhodopsin: Conservation of Free Energy after Photoisomerization of the Retinal. *J. Mol. Biol.* **2002**, *321*, 715-726.
- (48) Åberg, U.; Åkesson, E.; Sundström, V., Excited State Dynamics of Barrierless Isomerization in Solution. *Chem. Phys. Lett.* **1993**, *215*, 388-394.



## Chapter 2: Experimental

In this chapter, spectroscopic methods that are used in this study are described.

### 2.1 Femtosecond time-resolved spectroscopy

Femtosecond time-resolved spectroscopy primarily requires more than one optical pulse including a pump pulse that triggers the photoreaction of the sample and a probe pulse (or gate pulse) that is used to observe the property of the sample. To generate these pulses, the output of femtosecond pulsed laser is divided into several portions by beam splitters, and their wavelengths are converted to wavelengths desirable for the measurement.

The sample is first irradiated by a pump pulse, inducing the photoreaction. Then, after certain delay time ( $\Delta T$ ), a probe pulse probes the optical properties of the sample such as optical density or reflectance. The delay time ( $\Delta T$ ) is adjusted by changing the difference in the path length (from the position of the beam splitter to the position of the sample) between the pump and probe pulses<sup>1, 2</sup> with sub-micrometer precision using motorized delay stage (pump-probe experiment, Figure 2.1). For example, if the path length of the pump pulse is 300  $\mu\text{m}$  shorter than that of the probe pulse, the probe pulse arrives at the sample position at 1 ps after the pump pulse initiates the photoreaction, reporting the optical property of the sample at  $\Delta T=1$  ps. By scanning the difference in the path length between the pump and probe pulses, time-resolved spectra at various delays are obtained. The details of the experimental techniques of femtosecond time-resolved absorption, fluorescence, and Raman spectroscopies are explained in the following sections.

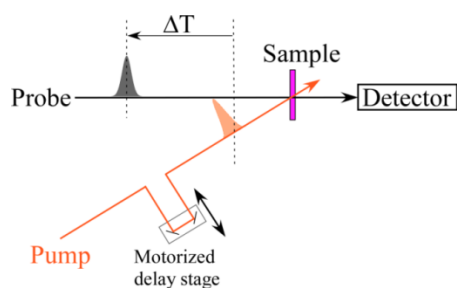


**Figure 2.1.** Schematic illustration of the pump-probe experiment.

### 2.1.1 Femtosecond time-resolved absorption spectroscopy

Although various femtosecond spectroscopies have been developed, femtosecond time-resolved absorption spectroscopy remains the most used technique. This is because this method provides fundamental information such as the lifetime or the electronic spectrum of the transient species.

In femtosecond time-resolved absorption spectroscopy, the probe pulse is used to monitor the absorbance of the sample at  $\Delta T$ . The femtosecond time-resolved absorption spectrum is the change in the absorption spectrum induced by the pump pulse

$$\Delta A(\lambda, \Delta T) = -\log_{10} \frac{I_{ON}^{SAM}(\lambda, \Delta T)}{I_{OFF}^{SAM}(\lambda, \Delta T)}$$

where  $I_{ON}^{SAM}(\lambda, \Delta T)$  and  $I_{OFF}^{SAM}(\lambda, \Delta T)$  are the probe intensities at probing wavelength  $\lambda$ , i.e., the probe spectra after passing through the sample with and without pump pulse at  $\Delta T$ .

In actual experiment, not only the probe spectra after pathing through the sample  $I_{ON}^{SAM}(\lambda_{pr}, \Delta T)$  but also the reference spectra (the probe spectra before pathing through the sample)  $I^{REF}(\lambda, \Delta T)$  are measured simultaneously (Figure 2.2), and the probe spectra after passing through the sample  $I_{ON}^{SAM}(\lambda_{pr}, \Delta T)$  are divided by the reference spectra  $I^{REF}(\lambda, \Delta T)$  so that the fluctuations of the probe spectra are compensated. Then, the time-resolved absorption spectrum  $\Delta A(\lambda, \Delta T)$  is calculated as

$$\Delta A(\lambda, \Delta T) = -\log_{10} \frac{I_{ON}^{SAM}(\lambda, \Delta T)}{I_{ON}^{REF}(\lambda, \Delta T)} \cdot \frac{I_{OFF}^{REF}(\lambda, \Delta T)}{I_{OFF}^{SAM}(\lambda, \Delta T)}$$

where  $I_{ON}^{SAM}(\lambda, \Delta T)$  and  $I_{OFF}^{SAM}(\lambda, \Delta T)$  are the probe spectra after passing through the sample with and without pump pulse at  $\Delta T$ , and  $I_{ON}^{REF}(\lambda, \Delta T)$  and  $I_{OFF}^{REF}(\lambda, \Delta T)$  are the reference spectra with and without pump pulse at  $\Delta T$ .

(a) Pump ON

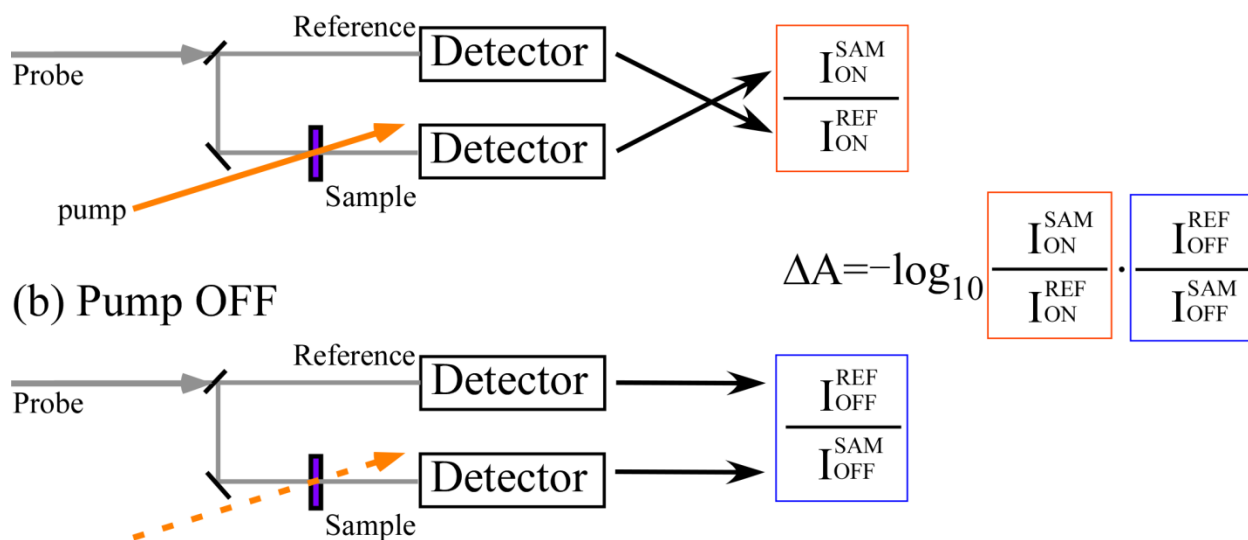


**Figure 2.2.** Schematic illustration of the scheme of the femtosecond time-resolved absorption measurement and the calculation of the femtosecond absorption spectrum. The femtosecond absorption spectrum is calculated using the observed probe spectra (a) with and (b) without pump.

The time-resolved absorption spectrum exhibits several characteristic signals, which are called bleaching, transient absorption, and stimulated emission. The bleaching signal appears as a negative peak in the wavelength region where the steady-state absorption band appears, reflecting the decrease in the ground-state molecules upon excitation. The transient absorption appears as a positive peak, indicating the absorption of the transient species, such as the photoproduct or the excited-state species. The stimulated emission is an emission induced by the probe light, and appears as a negative peak in the wavelength region longer than the excitation wavelength. Since the transient absorption due to the excited state and the stimulated emission are observed only when the population exists in the excited states, the decay of their amplitudes can be used to analyze the excited-state lifetime.

As an example, femtosecond absorption spectrum of KR2 at pH 4 immediately after  $S_1 \leftarrow S_0$  photoexcitation (at 0.1 ps) is shown in Figure 2.3. A positive band observed around 500 nm corresponds to the transient absorption from the  $S_1$  state to the higher excited state (excited-state

absorption, ESA). A negative band around 550 nm is the bleaching (BL) signal due to the decrease in the  $S_0$  population. Another negative band around 720 nm corresponds to the  $S_1 \rightarrow S_0$  stimulated emission (SE).

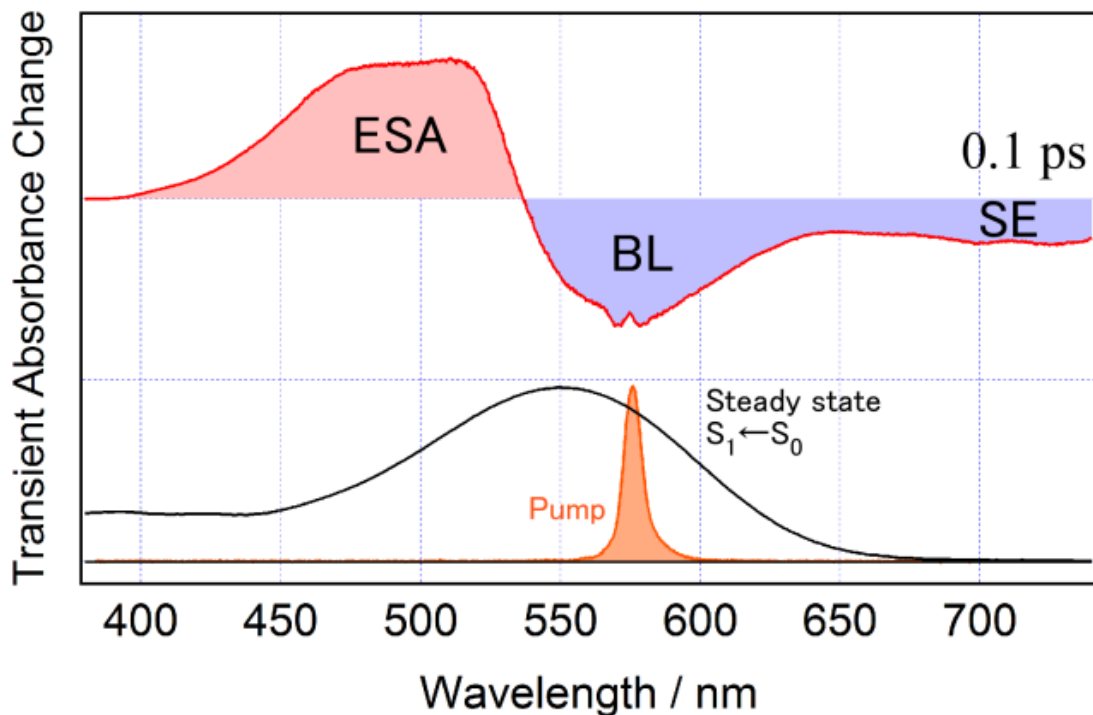


**Figure 2.3.** An example of femtosecond absorption spectrum (KR2 at pH4 at 0.1 ps). The upper (red curve filled to zero by red or blue) depicts the femtosecond absorption spectrum. The lower spectrum (black) depicts the steady-state absorption spectrum. The pump spectrum (filled orange) is also shown. ESA: excited-state absorption, BL: bleaching, SE: stimulated emission

### 2.1.2 Femtosecond Kerr-gate fluorescence spectroscopy

The transient absorption, the bleaching, and the stimulated emission are simultaneously observed in the femtosecond time-resolved absorption measurement. However, if these signals are significantly overlapped, the analysis and interpretation of the obtained data can be difficult. On the other hand, fluorescence spectroscopy provides the pure signal of the excited-state because the fluorescence is emitted only by the molecules in the singlet excited state. Therefore, femtosecond time-resolved fluorescence spectroscopy is a powerful tool for selective observation of the excited-state dynamics.

There are two major femtosecond time-resolved fluorescence spectroscopies using “upconversion” and “Kerr-gate” methods. Femtosecond time-resolved upconversion fluorescence spectroscopy is the most used time-resolved fluorescence technique. In this method, the sample is first excited by a pump pulse, and then emits the fluorescence. This fluorescence and another pulsed light called “gate pulse” are focused into the nonlinear crystal, and generate the sum frequency. The sum frequency is generated only when the fluorescence and the gate pulse are focused into the nonlinear crystal simultaneously. Therefore, if the gate pulse is sufficiently short with respect to the fluorescence decay time, the fluorescence intensity at delay time  $\Delta T$  is measured by monitoring the intensity of the sum frequency light. However, the measurement of the fluorescence intensities at various wavelengths, i.e., the time-resolved fluorescence spectrum using this method is time consuming. This is because the nonlinear crystal needs to be rotated so that the fluorescence at each wavelength and the gate pulse satisfy the phase matching condition. On the other hand, femtosecond time-resolved Kerr-gate fluorescence spectroscopy enables us to obtain the time-resolved fluorescence spectra at once. Herein, the experimental technique of femtosecond Kerr-gate fluorescence spectroscopy<sup>3-6</sup> is described.

In this method, an ultrafast optically controlled shutter called “Kerr shutter” is used. Kerr shutter consists of two polarizers and an isotropic material (“Kerr medium”) arranged between these polarizers (Figure 2.4). The polarizations of these polarizers are set to vertical and horizontal, respectively.

The sample is first excited by a pump pulse, and the fluorescence is emitted by the sample. Then, this fluorescence enters the first polarizer of the Kerr shutter. Here, only the vertical component of the fluorescence can transmit the first polarizer of the Kerr shutter (Figure 2.4a). And then, after passing through the Kerr medium, this vertically polarized fluorescence is blocked by the horizontal polarizer. Therefore, the fluorescence cannot pass through the Kerr shutter (the Kerr shutter is closed).

However, while a 45-degree polarized ultrashort pulse “gate pulse” irradiates the Kerr medium, the anisotropic change in the refractive index of the Kerr medium (called “Optical Kerr Effect”) is induced, giving rise to the transient birefringence of the Kerr medium (Figure 2.4b). If the vertically polarized fluorescence passes through the Kerr medium when the transient birefringence is induced, the polarization of the fluorescence is changed, and becomes elliptical in general. Since the polarization of the fluorescence is no longer vertical, the fluorescence can partially pass through the second horizontal polarizer (the Kerr shutter is open). Therefore, the fluorescence can pass through the Kerr shutter only when the gate pulse irradiates the Kerr medium. By scanning the path length of the gate pulse, time-resolved fluorescence spectra at various delays are obtained.

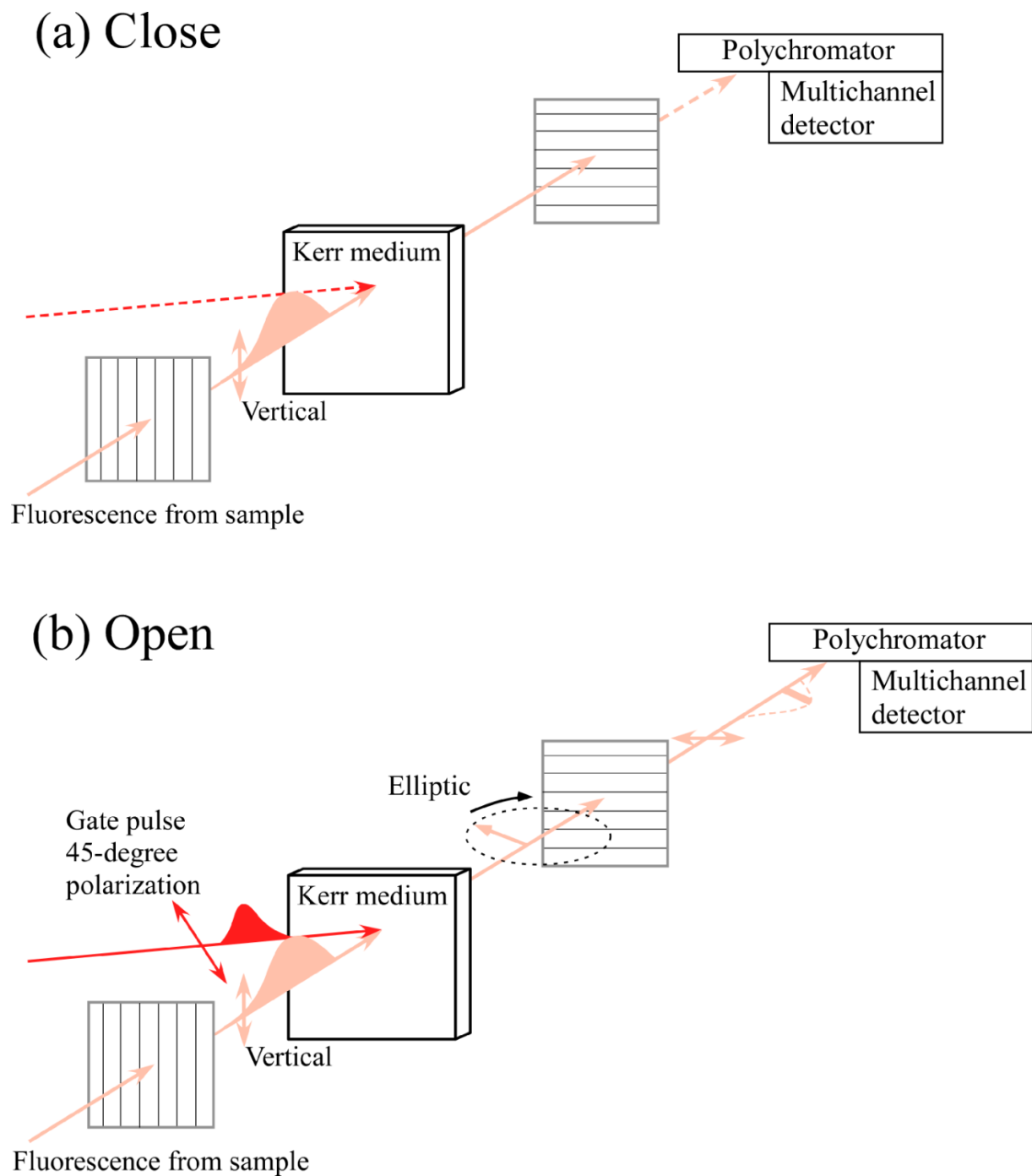


**Figure 2.4.** Schematic illustration of the Kerr shutter. (a) Kerr shutter is close in the absence of the gate pulse. (b) Kerr shutter is open while the gate pulse irradiates the Kerr medium.

### 2.1.3 Femtosecond stimulated Raman spectroscopy

Although femtosecond electronic spectroscopies provide important information such as the lifetime or electronic spectrum of the transient species, these techniques are not very sensitive to the structural change of the molecule. Recently, ultrafast X-ray diffraction method has been developed in order to observe the structural change of the molecule at the atomic scale in the femto/picosecond time region. This method has successfully captured the structures of the first intermediates of photoactive yellow protein.<sup>7, 8</sup> Although the X-ray method is powerful to determine the absolute atomic geometry of the molecule, the structural difference in the subatomic scale cannot be detected. Moreover, the crystallographic data provide only the electron density map, and thus this method does not provide any information about bonding strengths and binding modes. To obtain such detailed structural changes in the femto/picosecond time region, femtosecond time-resolved vibrational spectroscopy is usually employed. One of the most used femtosecond vibrational spectroscopic techniques is femtosecond infrared absorption spectroscopy that utilizes the infrared pulse as a probe<sup>9</sup>. However, it is quite challenging to apply this technique to the photoreceptor proteins because protein backbone and water in the sample strongly absorb the infrared probe pulse. For the measurement of the vibrational spectrum of photoreceptor proteins, Raman spectroscopy is primarily preferred. This is because the Raman spectroscopy employs the visible light, which is not primarily absorbed by protein backbone and water.

The frequency resolution and time resolution of the time-resolved spontaneous Raman spectroscopy are limited by the bandwidth and pulse duration of the Raman pump pulse, respectively. However, one cannot achieve both high frequency resolution and high time resolution simultaneously since the bandwidth and the pulse duration is limited by transform limit. In other words, if one increases the frequency resolution, the time resolution becomes worse, and vice versa. Typically,  $\sim 10\text{-cm}^{-1}$  frequency resolution is required to analyze the Raman spectrum, limiting the time resolution lower than several picoseconds<sup>10</sup>.

However, in the last decade, time-resolved impulsive stimulated Raman spectroscopy (TR-ISRS)<sup>11-13</sup> and femtosecond stimulated Raman spectroscopy (FSRS)<sup>14-18</sup> have been developed. These methods allow us to measure the Raman spectrum with sub-picosecond time precision and sufficient frequency resolution. TR-ISRS is a time-domain Raman spectroscopy.

In TR-ISRS measurement, the transient species is first created by an actinic pump pulse. Subsequently, the nuclear wavepacket motion of the transient species is induced by a broadband (and ultrashort (typically <10 fs)) pulse through the impulsive stimulated Raman process. The vibrational spectrum of the transient species is obtained by Fourier analysis of the periodic modulation of the absorbance due to the nuclear wavepacket motion. Because of the broadness of the spectrum of this pulse that is used to induce the nuclear wavepacket motion, it is sometimes difficult to adjust the pulse spectrum so that the pulse selectively excites the transient species of interest. On the other hand, FSRS is a frequency-domain Raman spectroscopy. This method does not need broadband pulse. Therefore, the transient species of interest can be selectively excited. Herein, the experimental technique of FSRS method is described.

In this method, the transient species is first created by an actinic pump pulse (Figure 2.5). After certain delay time ( $\Delta T$ ), a narrowband picosecond Raman pump pulse, which is resonant with the electronic transition of the transient species of interest, and a femtosecond supercontinuum probe pulse are simultaneously focused into the sample, yielding a resonantly enhanced stimulated Raman spectrum of the transient species. Due to the narrowness of the Raman pump bandwidth, Raman pump spectrum can be easily adjusted so that the transient species of interest is selectively observed. The frequency resolution of the FSRS spectrum is primarily determined by the bandwidth of the Raman pump pulse (typically 10-20  $\text{cm}^{-1}$ ). Moreover, since the stimulated Raman process occurs only when the Raman pump and supercontinuum probe pulses simultaneously irradiate the sample, the Raman process can be triggered with a temporal precision which is determined by the pulse duration of the femtosecond supercontinuum probe (typically  $\sim 100$  fs). The transmitted supercontinuum probe pulse, in which the stimulated Raman signal is contained, is spectrally analyzed by a polychromator and detected by a multichannel detector. By following this scheme, time-resolved stimulated Raman spectrum in a wide wavenumber region is observed simultaneously. By scanning the interval between the actinic pump pulse and the pair of the Raman pump and supercontinuum probe pulses, the stimulated Raman spectra at various delays ( $\Delta T$ ) are obtained (Figure 2.5).

The FSRS spectrum is measured as the transient absorbance change induced by the Raman pump. Therefore, the femtosecond stimulated Raman spectrum  $\Delta A(\nu_R, \Delta T)$  is calculated as follows

$$\Delta A(\nu_R, \Delta T) = -\log_{10} \frac{I_{ON}(\nu_R, \Delta T)}{I_{OFF}(\nu_R, \Delta T)}$$

where  $I_{ON}(\nu_R, \Delta T)$  and  $I_{OFF}(\nu_R, \Delta T)$  are the supercontinuum probe intensities at Raman shift  $\nu_R$  after passing through the sample with and without Raman pump pulse at  $\Delta T$ .

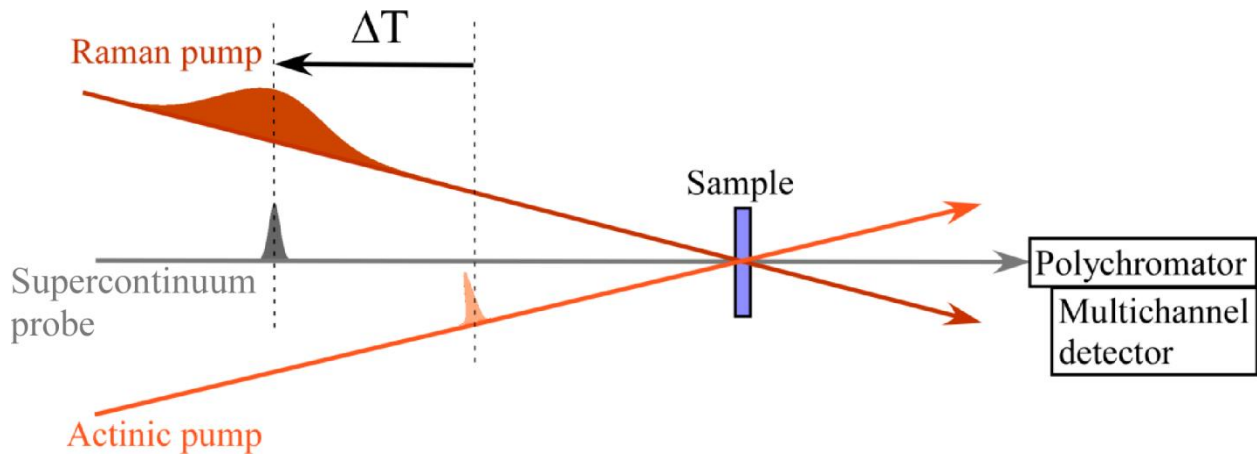


**Figure 2.5.** Schematic illustration of the measurement scheme of the FSRS.

## 2.2 References

- (1) Rose, T. S.; Rosker, M. J.; Zewail, A. H., Femtosecond Real - Time Observation of Wave Packet Oscillations (Resonance) in Dissociation Reactions. *J. Chem. Phys.* **1988**, *88*, 6672-6673.
- (2) Rose, T. S.; Rosker, M. J.; Zewail, A. H., Femtosecond Real - Time Probing of Reactions. Iv. The Reactions of Alkali Halides. *J. Chem. Phys.* **1989**, *91*, 7415-7436.
- (3) Duguay, M. A.; Hansen, J. W., An Ultrafast Light Gate. *Appl. Phys. Lett.* **1969**, *15*, 192-194.
- (4) Schmidt, B.; Sobotta, C.; Heinz, B.; Laimgruber, S.; Braun, M.; Gilch, P., Excited-State Dynamics of Bacteriorhodopsin Probed by Broadband Femtosecond Fluorescence Spectroscopy. *Biochim. Biophys. Acta (BBA) - Bioenergetics* **2005**, *1706*, 165-173.
- (5) Jaye, A. A.; Stoner-Ma, D.; Matousek, P.; Towrie, M.; Tonge, P. J.; Meech, S. R., Time-Resolved Emission Spectra of Green Fluorescent Protein. *Photochem. Photobiol.* **2006**, *82*, 373.
- (6) Nakamura, R.; Hamada, N.; Ichida, H.; Tokunaga, F.; Kanematsu, Y., Coherent Oscillations in Ultrafast Fluorescence of Photoactive Yellow Protein. *J. Chem. Phys.* **2007**, *127*, 215102.
- (7) Schotte, F.; Cho, H. S.; Kaila, V. R. I.; Kamikubo, H.; Dashdorj, N.; Henry, E. R.; Graber, T. J.; Henning, R.; Wulff, M.; Hummer, G.; Kataoka, M.; Anfinrud, P. A., Watching a Signaling Protein Function in Real Time Via 100-Ps Time-Resolved Laue Crystallography. *Proc. Natl. Acad. Sci. USA* **2012**, *109*, 19256-19261.
- (8) Jung, Y. O.; Lee, J. H.; Kim, J.; Schmidt, M.; Moffat, K.; Šrajcar, V.; Ihee, H., Volume-Conserving Trans–Cis Isomerization Pathways in Photoactive Yellow Protein Visualized by Picosecond X-Ray Crystallography. *Nat. Chem.* **2013**, *5*, 212-220.
- (9) Herbst, J.; Heyne, K.; Diller, R., Femtosecond Infrared Spectroscopy of Bacteriorhodopsin Chromophore Isomerization. *Science* **2002**, *297*, 822-5.
- (8) Zhu, L.; Kim, J.; Mathies, R. A., Picosecond Time-Resolved Raman System for Studying Photochemical Reaction Dynamics: Application to the Primary Events in Vision. *J. Raman Spec.* **1999**, *30*, 777-783.
- (9) Takeuchi, S.; Ruhman, S.; Tsuneda, T.; Chiba, M.; Taketsugu, T.; Tahara, T., Spectroscopic Tracking of Structural Evolution in Ultrafast Stilbene Photoisomerization. *Science* **2008**, *322*, 1073-1077.
- (10) Fujiyoshi, S.; Takeuchi, S.; Tahara, T., Time-Resolved Impulsive Stimulated Raman Scattering from Excited-State Polyatomic Molecules in Solution. *J. Phys. Chem. A* **2003**, *107*, 494-500.

- (11) Banin, U.; Ruhman, S., Ultrafast Vibrational Dynamics of Nascent Diiodide Fragments Studied by Femtosecond Transient Resonance Impulsive Stimulated Raman Scattering. *J. Chem. Phys.* **1993**, *99*, 9318-9321.
- (12) Yoshizawa, M.; Kurosawa, M., Femtosecond Time-Resolved Raman Spectroscopy Using Stimulated Raman Scattering. *Phys. Rev. A* **1999**, *61*, 013808.
- (13) Kukura, P.; McCamant, D. W.; Yoon, S.; Wandschneider, D. B.; Mathies, R. A., Structural Observation of the Primary Isomerization in Vision with Femtosecond-Stimulated Raman. *Science* **2005**, *310*, 1006-1009.
- (14) Kukura, P.; McCamant, D. W.; Mathies, R. A., Femtosecond Stimulated Raman Spectroscopy. *Annu. Rev. Phys. Chem.* **2007**, *58*, 461-488.
- (15) Kuramochi, H.; Takeuchi, S.; Tahara, T., Ultrafast Structural Evolution of Photoactive Yellow Protein Chromophore Revealed by Ultraviolet Resonance Femtosecond Stimulated Raman Spectroscopy. *J. Phys. Chem. Lett.* **2012**, *3*, 2025-2029.
- (16) Takaya, T.; Iwata, K., Relaxation Mechanism of B-Carotene from S<sub>2</sub> (1B<sub>u</sub><sup>+</sup>) State to S<sub>1</sub> (2A<sub>g</sub><sup>-</sup>) State: Femtosecond Time-Resolved near-Ir Absorption and Stimulated Resonance Raman Studies in 900–1550 Nm Region. *J. Phys. Chem. A* **2014**, *118*, 4071-4078.

# Chapter 3: Ultrafast Photoreactions of the *All-Trans* and *13-Cis Anabaena* Sensory Rhodopsins Studied by Femtosecond Time-Resolved Kerr-Gate Fluorescence Spectroscopy

## 3.1 Introduction

Rhodopsins are seven-helical transmembrane proteins having a retinal bound to the amino group of the side chain of a lysine via a protonated Schiff base linkage. The rhodopsins are classified into type-I and type-II rhodopsins<sup>1</sup>. The visual pigments of higher animals possessing *11-cis* retinal chromophore<sup>2</sup> are classified as type-II rhodopsin. On the other hand, the bacterial rhodopsins, such as bacteriorhodopsin (bR)<sup>3</sup> and halorhodopsin (hR)<sup>4</sup>, are type-I rhodopsin. The type-I rhodopsin accommodates either an *all-trans* or *13-cis* retinal chromophore. Therefore, in general, the type-I rhodopsins having these retinal isomers coexist.

The photoexcitation converts the rhodopsins into several long-lived intermediates, in which their physiological functions are achieved<sup>5</sup>. As for bR, the proton pump function is achieved through the photocycle reaction of the *all-trans* bR (bR having an *all-trans* retinal). Upon photoexcitation of the *all-trans* bR, the J intermediate is formed within a few picoseconds. Subsequently, the J intermediate is converted into the K intermediate, and the photocycle reaction starts. The photocycle reaction of the *all-trans* bR is accompanied by salient structural change of the protein, giving rise to the outward proton pumping. On the other hand, the photoexcitation of the *13-cis* bR (bR having a *13-cis* retinal) allegedly yields an intermediate, which is called <sup>610</sup>C (or <sup>620</sup>C) intermediate<sup>6-8</sup>. In analogy with the *all-trans* bR, it is tempting to consider that this intermediate relaxes back to the *13-cis* bR<sup>6</sup> through the photocycle reaction. However, it is also possible that this intermediate is converted to the *all-trans* bR<sup>7</sup>. As described above, the photoreaction of the *13-cis* is not well-known<sup>9</sup>. This is because the illumination induces the “light-adaptation” reaction that unidirectionally converts the *13-cis* bR to the *all-trans* bR (Figure 3.1a)<sup>1</sup> during the spectroscopic experiment, and decreases the concentration of the *13-cis* bR.



*Anabaena* sensory rhodopsin (ASR) is a rhodopsin discovered from eubacterium *Anabaena* sp. PCC 7120<sup>10</sup>. Differently from the typical microbial rhodopsins, the all-*trans* ASR (ASR having an all-*trans* retinal) is photoconverted to the 13-*cis* ASR (ASR having a 13-*cis* retinal) through the long-lived intermediates, and vice versa (“Light-adaptation”) as shown in Figure 3.1b. Therefore, ASR achieves the photochromic reaction (photointerconversion) between the all-*trans* ASR and the 13-*cis* ASR<sup>11-13</sup>, while the photoreactions of the other rhodopsins are primarily cyclic. To elucidate the mechanism for this intriguing photoreaction of ASR, the structure and photoreactions of ASR have been studied extensively<sup>14-18</sup>.

Another characteristic feature of ASR is that 72% of the ground-state ASR exists as the 13-*cis* ASR in the “Light-adapted” condition<sup>12,14</sup>, in which the sample is continuously illuminated, while 97% of the ground-state ASR is the all-*trans* ASR in the dark. Owing to the high concentration of the 13-*cis* ASR in the “Light-adapted” condition, it is expected that the photoreaction of the 13-*cis* rhodopsin can be clearly observed. Recently, the S<sub>1</sub>-state dynamics of the all-*trans* and 13-*cis* ASRs were observed by means of femtosecond time-resolved absorption spectroscopy<sup>19-21</sup>. However, in the previous studies<sup>19</sup>, the S<sub>1</sub> dynamics of the all-*trans* and 13-*cis* ASRs are not clearly characterized. Moreover, although it was suggested that the S<sub>1</sub> state of the 13-*cis* ASR deactivates within a picosecond, the S<sub>1</sub> lifetimes of the 13-*cis* ASR reported by two different groups are different from each other ( $\tau=160\pm 30$  fs in ref. 19 and  $\tau<100$  fs in ref. 21). It is considered that the signals due to all the relaxation processes including the reactions in the ground state are superimposed on the deactivation signal of the S<sub>1</sub> states of the all-*trans* and 13-*cis* ASRs in the femtosecond time-resolved absorption signal. On the other hand, femtosecond time-resolved fluorescence spectroscopy enables us to selectively observe the S<sub>1</sub> dynamics of ASR since the fluorescence is emitted only by the singlet excited states.

In this study, femtosecond time-resolved Kerr-gate spectroscopy was used to investigate the excited-state dynamics of the all-*trans* and 13-*cis* ASRs. Based on the obtained fluorescence spectra, the photoisomerization dynamics of the all-*trans* and 13-*cis* retinals in the ASR protein are discussed.

## 3.2 Experimental methods

### Sample preparation

The ASR protein was prepared by an established method<sup>10</sup>. Briefly, the C-terminally His-tagged full-length ASR was expressed by *Escherichia coli* BL21(DE7) strain. The cells were harvested by centrifugating the cell culture and sonicated. The ASR protein was solubilized with 1% w/w *n*-dodecyl  $\beta$ -D-maltoside (DDM) and purified by Ni<sup>2+</sup>-nitrilotriacetic acid (Ni<sup>2+</sup>-NTA) column. The purified ASR solution was dialyzed with pH 7 PIPES buffer (25 mM PIPES, 200 mM NaCl, 0.1% w/w DDM). The optical density of the sample, which is used in the following experiment, is 0.4 OD/ mm at 552 nm in “Dark-adapted” condition (kept in the dark for a day).

### Femtosecond time-resolved Kerr-gate fluorescence spectroscopy

The schematic of the experimental setup is depicted in Figure 3.2. The 4.0-mJ portion of the output of a Ti:sapphire amplifier system (800 nm, 8.0 mJ, 80 fs, 1 kHz, Legend Elite Duo, Coherent) was used to drive an optical parametric amplifier (TOPAS-C, Light Conversion), and its idler output at 2220 nm was frequency-doubled to generate a pulse at 1110 nm. The 1110-nm pulse was divided into two portions. One of them is introduced to the mirror pair to change the polarization to 45 degrees, and used as a gate pulse. The other is frequency-doubled to generate a pump pulse at 555 nm. The pump polarization was set at the magic angle (54.7°). The pump pulse (40 nJ / pulse, FWHM ~ 100 fs) was focused into a flow cell (1-mm path length), in which the sample solution was circulated. The circulation speed was optimized so that each laser shot irradiates a fresh portion of the sample. The fluorescence from the sample was collected by a parabolic mirror, and passed through a wire-grid polarizer, which is set to vertical polarization. The 45-degree polarized gate pulse (12  $\mu$ J / pulse, FWHM ~ 100 fs) and the vertically-polarized fluorescence were focused into a 1-mm path length quartz cell, in which bromobenzene is contained as a Kerr medium. The fluorescence after passing through the Kerr medium and a Glan-Taylor polarizer, which is set to horizontal polarization, were spectrally analyzed by a polychromator (iHR320, Horiba) equipped with a CCD camera (PIXIS-400F, Princeton Instruments). The group delay dispersion of the fluorescence was examined by measuring the Kerr-gate signal of a supercontinuum generated at the sample position. The temporal profile of the supercontinuum was used to calibrate the time origin at each wavelength.

The instrumental response, which was evaluated based on the Kerr-gate signal of the supercontinuum at 700 nm, was not symmetric because the birefringence of the Kerr medium was induced by the off-resonant impulsive stimulated Raman process of the librational mode of bromobenzene (Raman-induced Kerr effect), which persists until 1 ps. Therefore, the instrumental response function (IRF) was reconstructed (purple line in inset of Figure 3.2) by a superposition of three Gaussian functions (Red, green and blue lines in inset of Figure 3.2). The reconstructed IRF is taken into account by convoluting it with the multiexponential function when the fluorescence kinetics is analyzed by the fitting procedure. The most dominant Gaussian component has  $\sim 250$  fs FWHM. Therefore, the time resolution of this experiment is estimated to be 250 fs.

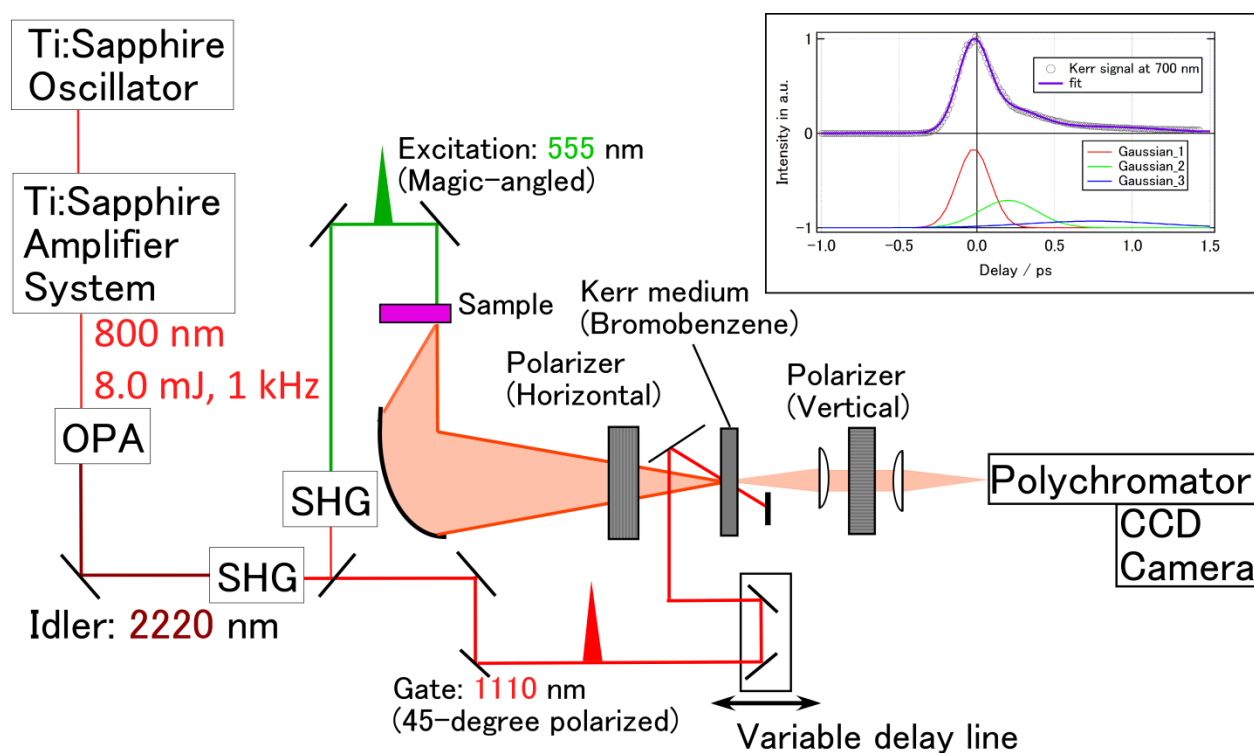


**Figure 3.2.** Schematic illustration of femtosecond Kerr-gate fluorescence apparatus. Kerr signal at 700 nm (gray circle), reconstructed instrumental response function (IRF, purple line) and Gaussians that are used to reconstruct the IRF (Red, green and blue lines) are shown in inset. OPA: Optical parametric amplifier, SHG: Second harmonic generator.

### 3.3 Results & Discussion

#### Absorption spectra of all-*trans* and 13-*cis* ASRs

The ASR sample is a mixture of the all-*trans* and 13-*cis* ASRs. It has been reported that the all-*trans* ASR:13-*cis* ASR ratio depends on the illumination condition<sup>10,12</sup>. In fact, the absorption spectra of “Dark-adapted” sample, which is kept in the dark for a day, was not identical to that of “Light-adapted” sample, which is illuminated by orange (>560 nm) light for 5 minutes (Figure 3.3a). According to the previous research, in the “Dark-adapted” condition, the all-*trans*:13-*cis* ratio reaches 0.97:0.03. On the other hand, in the “Light-adapted” sample, the all-*trans*:13-*cis* ratio is 0.28:0.72<sup>16</sup>. Based on the absorption spectra and the reported ratios in the “Dark-adapted” and “Light-adapted” conditions, the absorption spectra of the all-*trans* and 13-*cis* ASRs were calculated (Figure 3.3b). The absorption maximum wavelengths of the all-*trans* and 13-*cis* ASRs are 552 nm and 540 nm, respectively. These values are consistent with the previous reports<sup>11,13</sup>.

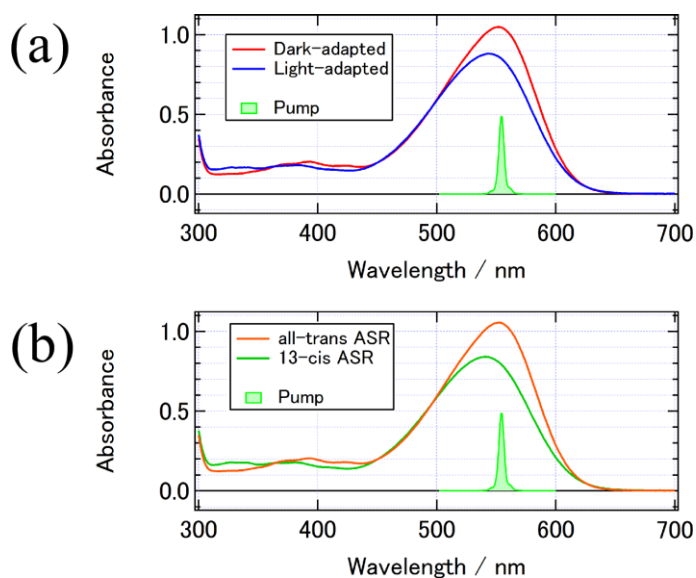


**Figure 3.3.** Absorption spectra of the ASR samples. (a) The absorption spectra of the “Dark-adapted” (red) and “Light-adapted” (blue) samples. (b) The absorption spectra of the all-*trans* (orange) and 13-*cis* (green) ASRs. The spectrum of the pump pulse used in the time-resolved experiment (555 nm, 5-nm FWHM) is depicted as a filled green spectrum. The “Dark-adapted” sample was prepared by keeping in the dark for a day. The “Light-adapted” sample was prepared by illuminating orange light for 5 minutes.

### **Femtosecond time-resolved Kerr-gate fluorescence measurements of “Dark-adapted” and “Light-adapted” ASRs**

To monitor the all-*trans*:13-*cis* ratio during the 200-minutes accumulation of the fluorescence signal in “Dark-adapted” condition, the absorption spectra of the sample were measured after 0, 100, 150, and 200 minutes from the start time of the measurement, and fitted by a sum of the absorption spectra of the all-*trans* and 13-*cis* ASRs. It was found that the molar fraction of the 13-*cis* ASR almost linearly increased from 0.03 to 0.17. This is because the pump pulse induces the photoreaction from the all-*trans* ASR to the 13-*cis* ASR through the “light-adaptation” reaction (Figure 3.1b). Based on the fitting of the absorption spectrum after 100 minutes, it is concluded that the time average of the molar fraction of the all-*trans* ASR during the measurement is 0.89 (all-*trans*:13-*cis* = 89:11). Therefore, hereafter, in the “Dark-adapted” condition, the all-*trans*:13-*cis* ratio is assumed to be 89:11.

Femtosecond time-resolved Kerr-gate fluorescence spectra of the “Dark-adapted” ASR at selected delays are shown in Figure 3.4a. The fluorescence intensity exhibited a peak around 0.1 ps, and almost completely decayed within 5 ps.

The femtosecond time-resolved Kerr-gate fluorescence spectra of the “light-adapted” ASR sample are shown in Figure 3.4b. On the basis of the absorption spectrum measured during the time-resolved fluorescence measurement, the all-*trans*:13-*cis* ratio was evaluated to be 28:72. Although the time evolution of the spectra was similar to that in the “Dark-adapted” condition, the observed time-resolved fluorescence intensity was weaker.

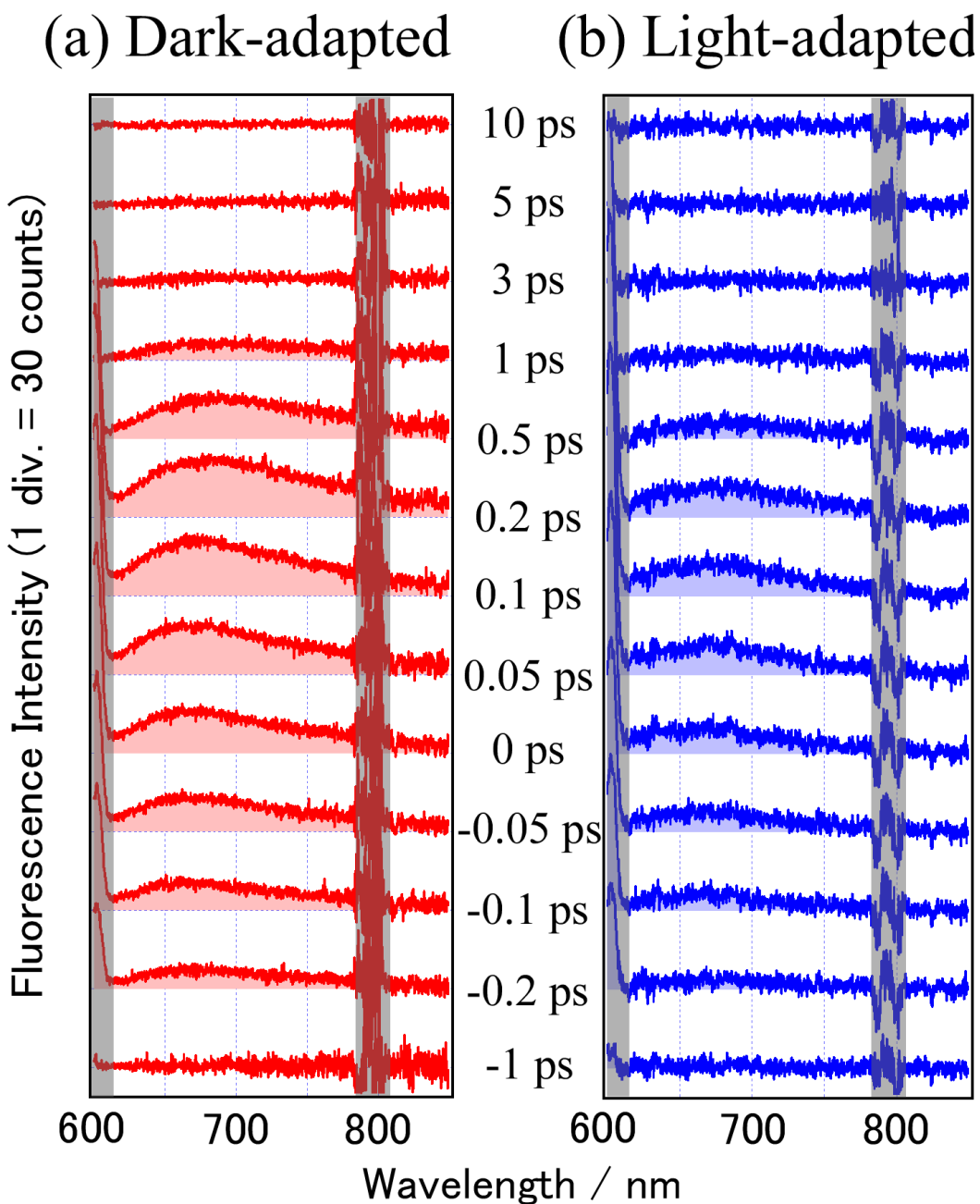


**Figure 3.4.** Femtosecond time-resolved Kerr-gate fluorescence spectra of (a) the “Dark-adapted” (red) and (b) the “Light-adapted” (blue) ASR samples at selected delays. The spectra in shaded wavelength regions are disturbed by the scattering of the pump pulse at 555 nm and the fundamental of the femtosecond laser at 800 nm. The energies of the pump and gate pulses were 40 nJ and 12  $\mu$ J, respectively. The FWHMs of the temporal profiles of these pulses were  $\sim$ 100 fs. The optical density of the sample (in the “Dark-adapted” condition) is 0.4 OD/ mm at 552 nm.

To extract the dynamics of ASR in the  $S_1$  state, the time-resolved fluorescence spectra in the 610-750 nm region were integrated, yielding the fluorescence kinetics (Figure 3.5). The direct comparison of these kinetics shows that the amplitude of the kinetics of the “Light-adapted” ASR (filled red circle) is smaller than that of the “Dark-adapted” ASR (filled blue circle). The kinetics of the “Dark-adapted” ASR was compared with the tail-matched kinetics of the “Light-adapted” ASR (multiplied by the factor of 3.2, open blue circle) in Figure 3.5. This comparison clearly shows that the “Light-adapted” ASR exhibits the fast decaying component within 1 ps. This rapid decay is attributable to the deactivation of the 13-*cis* ASR in the  $S_1$  state since the “Light-adapted” sample contains saliently high concentration of the 13-*cis* ASR (*all-trans*:13-*cis* = 28:72) compared with that of the “Dark-adapted” sample (89:11). On the other hand, in the picosecond region, the fluorescence decays are similar to each other, indicating that the fluorescence in this time region is attributable to the deactivation of the *all-trans* ASR in the  $S_1$  state.

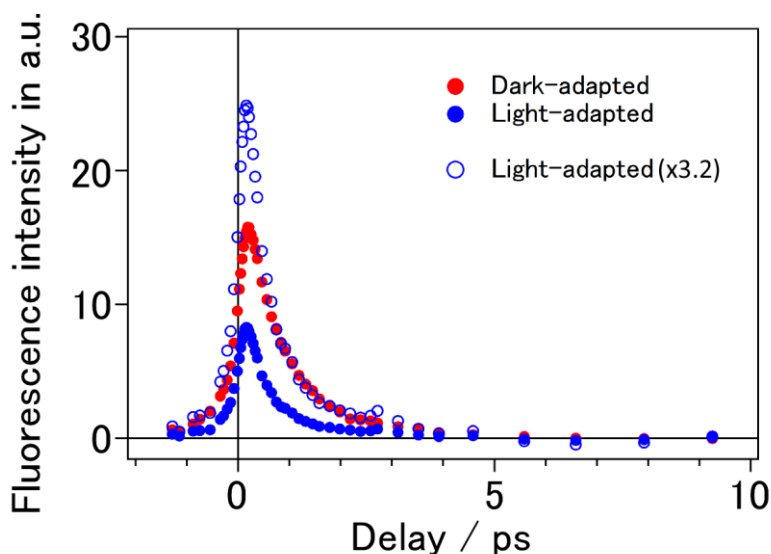


**Figure 3.5.** The fluorescence kinetics, which were obtained by integrating the fluorescence spectrum of the “Dark-adapted” and “Light-adapted” ASR samples in the 610-750 nm region. The kinetics of the “Dark-adapted” and “Light-adapted” ASR samples are shown in filled red and filled blue circles. The tail-matched “Dark-adapted” ASR kinetics (multiplied by the factor of 3.2) is shown in open blue circle. The energies of the pump and gate pulses were 40 nJ and 12  $\mu$ J, respectively. The FWHMs of the temporal profiles of these pulses were  $\sim$ 100 fs. The optical density of the sample (in the “Dark-adapted” condition) is 0.4 OD/mm at 552 nm.

### Femtosecond time-resolved Kerr-gate fluorescence signals of all-*trans* and 13-*cis* ASRs

The femtosecond time-resolved Kerr-gate fluorescence spectra of the all-*trans* and 13-*cis* ASRs were separated from the spectra measured in the “Dark-adapted” and “Light-adapted” conditions based on the all-*trans*:13-*cis* ratio in these conditions. In the “Dark-adapted” condition, the all-*trans*:13-*cis* ratio is 89:11. Therefore, assuming that the pump intensity is so weak that the number of the excited-state molecule created by the pump pulse is proportional to the optical density at the pump wavelength (555 nm), the time-resolved fluorescence spectra in the “Dark-adapted” condition can be given by

$$S_{DA}(\lambda, t) = r_{AT}^{DA} \varepsilon_{555}^{AT} s_{AT}(\lambda, t) + r_{13C}^{DA} \varepsilon_{555}^{13C} s_{13C}(\lambda, t) = 0.89 S_{AT}(\lambda, t) + 0.11 S_{13C}(\lambda, t)$$

where  $r_{AT}^{DA}$  and  $r_{13C}^{DA}$  are the molar fractions of the all-*trans* and 13-*cis* ASRs in the “Dark-adapted” condition (0.89 and 0.11, respectively),  $\varepsilon_{555}^{AT}$  and  $\varepsilon_{555}^{13C}$  are the extinction coefficients of the all-*trans* and 13-*cis* ASRs at 555 nm (excitation wavelength) and  $s_{AT}(\lambda, t)$  and  $s_{13C}(\lambda, t)$  are the time-resolved fluorescence spectra of the all-*trans* and 13-*cis* ASRs. The time-resolved fluorescence spectra were simplified by  $S_{AT}(\lambda, t) = \varepsilon_{555}^{AT} s_{AT}(\lambda, t)$  and  $S_{13C}(\lambda, t) = \varepsilon_{555}^{13C} s_{13C}(\lambda, t)$ . As well as the time-resolved fluorescence spectra in “Dark-adapted” condition, that in “Light-adapted” condition (all-*trans*:13-*cis* = 28:72) can be given by

$$S_{LA}(\lambda, t) = r_{AT}^{LA} \varepsilon_{555}^{AT} s_{AT}(\lambda, t) + r_{13C}^{LA} \varepsilon_{555}^{AT} s_{13C}(\lambda, t) = 0.28 S_{AT}(\lambda, t) + 0.72 S_{13C}(\lambda, t)$$

From these equations,

$$S_{AT}(\lambda, t) = \left(\frac{13}{11}\right) S_{DA}(\lambda, t) - \left(\frac{2}{11}\right) S_{LA}(\lambda, t), \quad S_{13C}(\lambda, t) = \left(\frac{100}{69}\right) S_{LA}(\lambda, t) - \left(\frac{31}{69}\right) S_{DA}(\lambda, t)$$

The obtained fluorescence spectrum of each isomer at selected delays is shown in Figure 3.6. The fluorescence of the all-*trans* ASR vanishes within 5 ps (Figure 3.6a). On the other hand, the 13-*cis* fluorescence almost completely decays within 1 ps. The fluorescence of the 13-*cis* ASR decays faster than that of the all-*trans* ASR, indicating that the S<sub>1</sub> lifetime of the 13-*cis* ASR is shorter than that of the all-*trans* ASR. Since the maximum S<sub>1</sub> ← S<sub>0</sub> extinction coefficient of the 13-*cis* ASR has the same order of magnitude as that of the all-*trans* ASR, their amplitudes of the time-resolved fluorescence should be comparable. However, in this study, the observed amplitude of the time-resolved fluorescence of the 13-*cis* ASR (Figure 3.6b) is

much smaller than that of the all-*trans* ASR. This is because the timescale of the fluorescence decay is comparable to the time resolution.

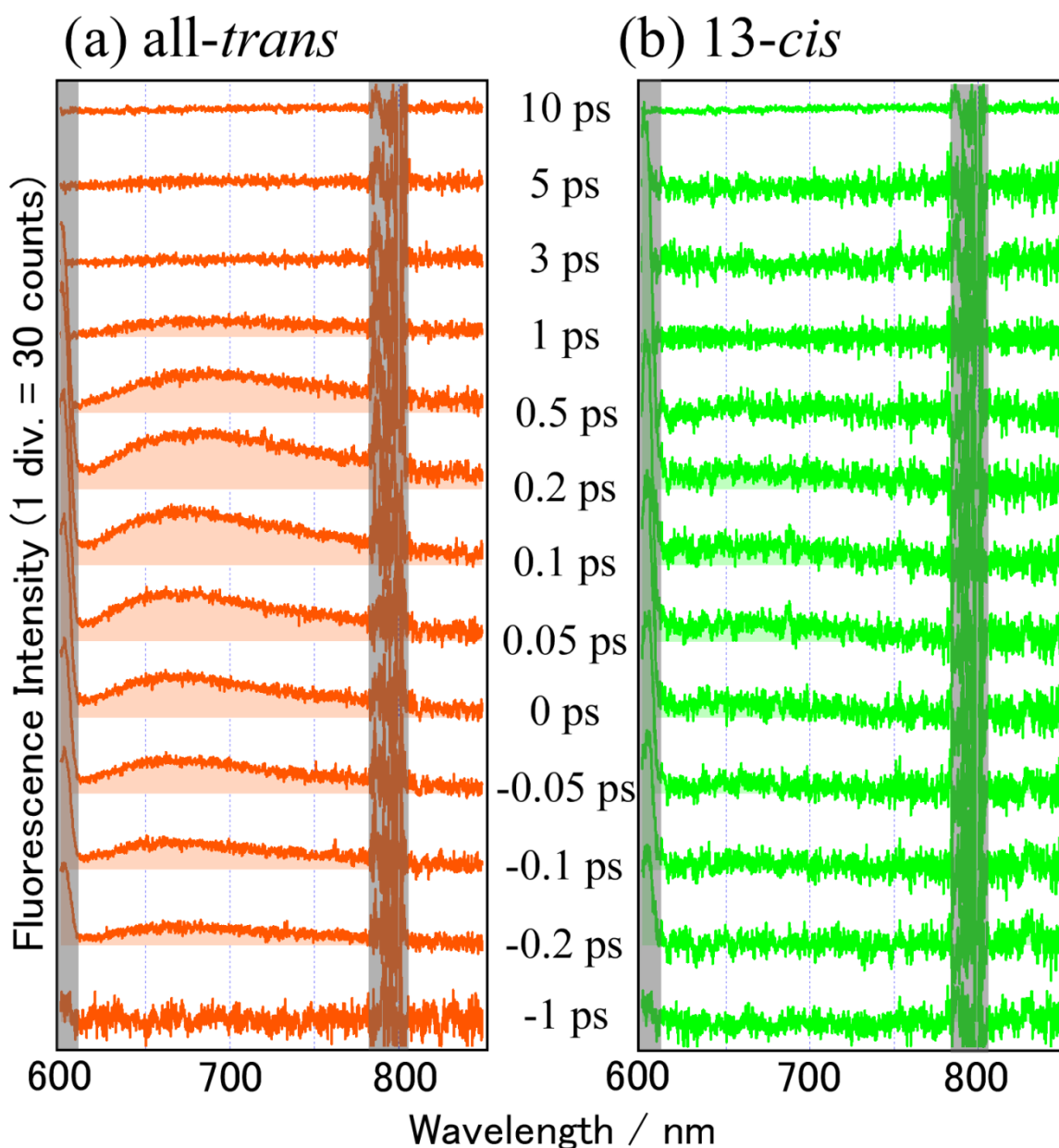


**Figure 3.6.** Femtosecond time-resolved Kerr-gate fluorescence spectra of the (a) all-*trans* (orange) and (b) 13-*cis* (green) ASRs at selected delays. The spectra in shaded wavelength regions are disturbed by the scattering of the pump pulse at 555 nm and the fundamental of the femtosecond laser at 800 nm. The energies of the pump and gate pulses were 40 nJ and 12  $\mu$ J, respectively. The FWHMs of the temporal profiles of these pulses were  $\sim$ 100 fs. The optical density of the sample (in the “Dark-adapted” condition) is 0.4 OD/ mm at 552 nm.

To extract the dynamics in the  $S_1$  state, the fluorescence kinetics of the all-*trans* and 13-*cis* ASRs are constructed by integrating the time-resolved fluorescence spectra in the 610-750 nm region. The obtained kinetics are shown in Figure 3.7. The fluorescence of the all-*trans* ASR almost completely diminishes within 5 ps, indicating that the all-*trans* ASR in the  $S_1$  state relaxes to the  $S_0$  state within this delay. To examine the dynamics of the all-*trans* ASR in the  $S_1$  state more quantitatively, the fitting analysis of the kinetics that takes the instrumental response (inset of Figure 3.2) into consideration was carried out. The kinetics was nicely reproduced by a superposition of two exponential components with time constants of 700 fs and 2 ps, suggesting that two  $S_1$  species with these lifetimes exist.

In the previous femtosecond time-resolved absorption study<sup>19</sup>, upon photoexcitation of the all-*trans* ASR, the photoproduct band showed up within 2 ps. This suggests that the 700-fs component gives rise to the photoproduct whereas the 2-ps component relaxes back to the original all-*trans*  $S_0$  state. Therefore, it is concluded that the photoisomerization of the all-*trans* retinal in ASR takes place with a time constant of 700 fs. Since the fluorescence vanished within 5 ps, the spectral change after 5 ps, which is observed in femtosecond absorption signal, is attributable to the dynamics in the ground state.

The existence of two distinct  $S_1$  states can be rationalized by either of two mechanisms shown in Figure 3.8a. In mechanism (i), the population branches in the vicinity of the Franck-Condon state, giving rise to two  $S_1$  species. In mechanism (ii), two distinct ground-state species having different chemical properties exist, and each species is excited to the  $S_1$  state in parallel, giving rise to two species in the  $S_1$  state. However, it is difficult to judge which is more likely based on the present experiment.

On the other hand, as shown in Figure 3.7b, the 13-*cis* fluorescence vanishes within 1 ps. The 13-*cis* fluorescence kinetics is reproduced by single exponential component with a time constant of 250 fs, indicating that the photoisomerization of the 13-*cis* retinal in ASR occurs with a time constant of 250 fs. This result is close to the lifetime reported in ref. 19 ( $160 \pm 30$  fs) rather than that in ref. 21 ( $<100$  fs).

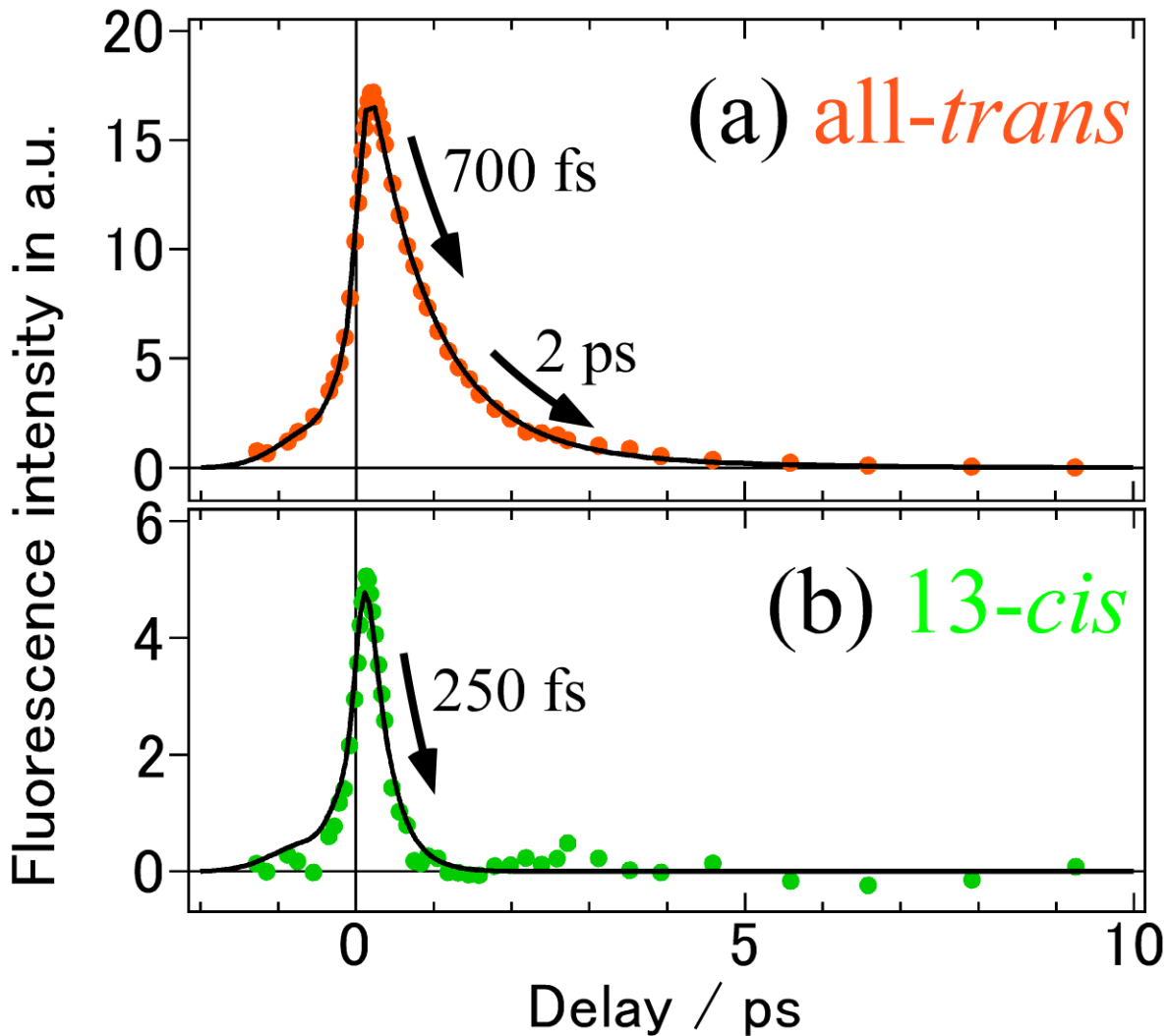
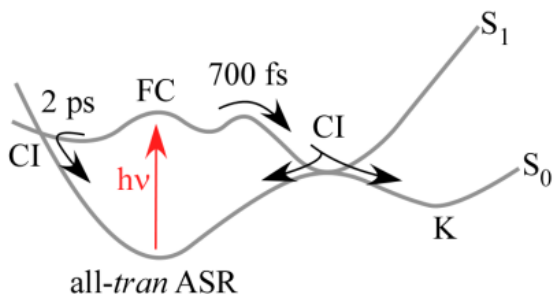


**Figure 3.7.** The fluorescence kinetics of the (a) *all-trans* and (b) *13-cis* ASRs. The black curves depict the fits. The energies of the pump and gate pulses were 40 nJ and 12  $\mu$ J, respectively. The FWHMs of the temporal profiles of these pulses were  $\sim$ 100 fs. The optical density of the sample (in the “Dark-adapted” condition) is 0.4 OD/ mm at 552 nm.

The period of the twisting motion about C<sub>13</sub>C<sub>14</sub> double bond of the all-*trans* retinal chromophore in the ASR protein is reported to be ~200 fs<sup>19</sup> based on the Fourier analysis of the beat signal due to the nuclear wavepacket motion superimposed on the femtosecond absorption kinetics. The period of the twisting motion about C<sub>13</sub>C<sub>14</sub> double bond of the 13-*cis* retinal should be comparable to that of the all-*trans* retinal in the ASR protein (~200 fs). This value is comparable to the time constant for the isomerization of the 13-*cis* retinal in the ASR protein (250 fs) obtained in this study. Therefore, the 13-*cis* retinal isomerizes almost within the period of the C<sub>13</sub>C<sub>14</sub> double bond twisting. Thus, it is possible that the S<sub>1</sub> population of the 13-*cis* retinal in ASR moves toward the conical intersection (CI in Figure 3.8) in the absence of the finite energy barrier (Figure 3.8b). If it is true, the time-resolved fluorescence spectrum of the 13-*cis* ASR is expected to exhibit a gradual red shift, because the S<sub>1</sub> and S<sub>0</sub> potentials gradually approach each other. In the present experiment, due to low S/N ratio, it was impossible to judge whether the time-resolved fluorescence spectrum takes place the gradual red shift.

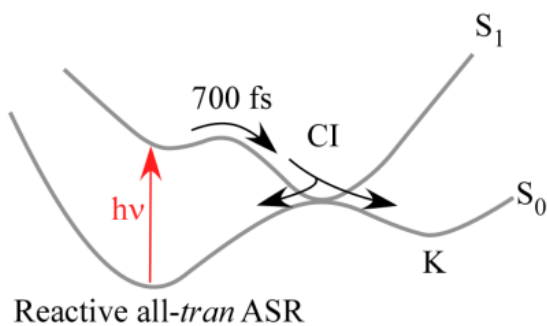
## (a) *all-trans*

### Mechanism (i)

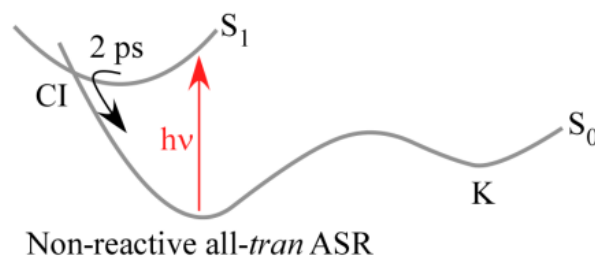


### Mechanism (ii)

#### Reactive component



#### Non-reactive component



## (b) *13-cis*

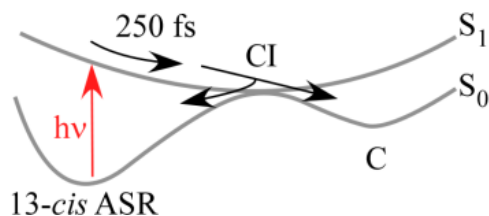


**Figure 3.8.** Schematic illustration of the relaxation pathways of the *all-trans* and *13-cis* ASRs in the S<sub>1</sub> state. (a) Two possible relaxation mechanisms of the *all-trans* ASR. (b) The relaxation pathway of the *13-cis* ASR.

From the structural viewpoint, the protein structures of the all-*trans* and 13-*cis* ASRs are similar to each other<sup>14</sup>. Therefore, the direct comparison between the fluorescence data of the all-*trans* and 13-*cis* ASRs show how the photoisomerization dynamics depends on the conformation of the chromophore in the ASR protein. The photoisomerization of the all-*trans* retinal in ASR proceeds with a time constant of 700 fs, while that of the 13-*cis* retinal takes place with a time constant of 250 fs, manifesting that the chromophore conformation is an important factor that determines the isomerization rate in the ASR protein. It has been reported that the photoisomerization process of *cis*-stilbene in solution is one order of magnitude faster than that of *trans*-stilbene ( $\sim 1$  ps vs  $\sim 30$  ps)<sup>22-23</sup>. The result presented here indicates that the same is true for the retinal in the ASR protein.

### 3.4 Conclusions

The femtosecond time-resolved fluorescence spectra of the all-*trans* and 13-*cis* ASRs were measured by femtosecond Kerr-gate fluorescence spectroscopy. Based on the fitting analysis of the fluorescence kinetics, the all-*trans* retinal in the ASR protein isomerizes with a time constant of 700 fs whereas the 13-*cis* retinal undergoes isomerization with a time constant of 250 fs. Based on these observations, it is concluded that the photoisomerization of the 13-*cis* retinal proceeds several times faster than that of the all-*trans* retinal in the ASR protein, suggesting that the chromophore conformation significantly affects the photoisomerization dynamics in the ASR protein.

### 3.5 References

- (1) Briggs, W. R.; Spudich, J. L. *Handbook of Photosensory Receptors*. Wiley, Weinheim, Germany, 2006.
- (2) Honig, B.; Greenberg, A. D.; Dinur, U; Ebrey, T. G. Visual-Pigment Spectra: Implications of the Protonation of the Retinal Schiff Base. *Biochemistry* **1976**, *15*, 4593-4599.
- (3) Oesterhelt, D. and Stoeckenius, W. Rhodopsin-like Protein from the Purple Membrane of *Halobacterium halobium*. *Nat. New Biol.* **1971**, *233*, 149-152.
- (4) Schobert, B.; Lanyi, J. K. Halorhodopsin is a Light-driven Chloride Pump. *J. Biol. Chem.* **1982**, *257*, 10306-10313.
- (5) Lozier, R. H.; Bogomolni, R. A.; Stoeckenius, W. Bacteriorhodopsin: a Light-Driven Proton Pump in *Halobacterium Halobium*. *Biophys. J.* **1975**, *15*, 955-962.
- (6) Kalisky, O.; Goldschmidt, C.; Ottolenghi, M. On the Photocycle and Light Adaptation of Dark-adapted Bacteriorhodopsin. *Biophys. J.* **1977**, *19*, 185-189.
- (7) Iwasa, T.; Tokunaga, F.; Yoshizawa, T. Photochemical Reaction of 13-*Cis*-bacteriorhodopsin Studied by Low Temperature Spectrophotometry. *Photochem. Photobiol.* **1981**, *33*, 539-545.
- (8) Gergely, C.; Ganea, C.; Váró, G. Combined Optical and Photoelectric Study of the Photocycle of 13-*cis* Bacteriorhodopsin. *Biophys. J.* **1994**, *67*, 855-861.
- (9) Bryl, K.; Taiji, M.; Yoshizawa, M.; Kobayashi, T. Light Adaptation of Dark-Adapted Bacteriorhodopsin Studied by Nanosecond Time-Resolved Absorption Spectroscopy. *Photochem. Photobiol.* **1992**, *56*, 1013-1018.
- (10) Jung, K. H.; Trivedi, V. D.; Spudich, J. L. Demonstration of a Sensory Rhodopsin in Eubacteria. *Mol. Microbiol.* **2003**, *47*, 1513–1522.
- (11) Kawanabe A.; Furutani, Y.; Jung, K. H.; Kandori, H. Photochromism of *Anabaena* Sensory Rhodopsin. *J. Am. Chem. Soc.* **2007**, *129*, 8644–8649.
- (12) Sineshchekov, O. A.; Trivedi, V. D.; Sasaki, J.; Spudich, J. L. Photochromicity of *Anabaena* Sensory Rhodopsin, an Atypical Microbial Receptor with a *cis*-Retinal Light-adapted Form. *J. Biol. Chem.* **2005**, *280*, 14663-14668.
- (13) Tahara, S.; Kato, Y.; Kandori, H.; Ohtani, H. pH-Dependent Photoreaction Pathway of the All-*Trans* Form of *Anabaena* Sensory Rhodopsin. *J. Phys. Chem. B* **2013**, *117*, 2053-2060.
- (14) Vogeley, L.; Sineshchekov, O. A.; Trivedi, V. D.; Sasaki, J.; Spudich, J. L.; Luecke, H. *Anabaena* Sensory Rhodopsin: A Photochromic Color Sensor at 2.0 Å. *Science* **2004**, *306*, 1390–1393.
- (15) Furutani, Y.; Kawanabe, A.; Jung, K. H.; Kandori, H. FTIR Spectroscopy of the All-*Trans* Form of *Anabaena* Sensory Rhodopsin at 77 K: Hydrogen Bond of a Water Between the Schiff Base and Asp75. *Biochemistry* **2005**, *44*, 12287-12296.
- (16) Kawanabe, A.; Furutani, Y.; Jung, K. H.; Kandori, H. FTIR Study of the Photoisomerization Processes in the 13-*Cis* and all-*trans* Forms of *Anabaena* Sensory Rhodopsin at 77K. *Biochemistry* **2006**, *45*, 4362-4370.

- (17) Kawanabe, A.; Furutani, Y.; Yoon, S. R.; Jung, K. H.; Kandori, H. FTIR Study of the L Intermediate of *Anabaena* Sensory Rhodopsin: Structural Changes in the Cytoplasmic Region. *Biochemistry* **2008**, *47*, 10033-10040.
- (18) Kondoh, M.; Inoue, K.; Sasaki, J.; Spudich, J. L.; Terazima, M. Transient Dissociation of the Transducer Protein from *Anabaena* Sensory Rhodopsin Concomitant with Formation of the M State Produced upon Photoactivation. *J. Am. Chem. Soc.* **2011**, *133*, 13406-13412.
- (19) Wand, A.; Rozin, R.; Eliash, T.; Jung, K. H.; Sheves, M.; Ruhman, S. Asymmetric Toggling of a Natural Photoswitch; Ultrafast Spectroscopy of *Anabaena* sensory rhodopsin. *J. Am. Chem. Soc.* **2011**, *133*, 20922-20932.
- (20) Wand, A.; Loevsky, B.; Friedman, N.; Sheves, M.; Ruhman, S. Probing Ultrafast Photochemistry of Retinal Protein in the Near-IR: Bacteriorhodopsin and *Anabaena* sensory rhodopsin vs Retinal Protonated Schiff Base in Solution. *J. Phys. Chem. B* **2013**, *117*, 4670-4679.
- (21) Cheminal, A.; Léonard, J.; Kim, S. Y.; Jung, K. H.; Kandori, H.; Haacke, S. 100 fs Photo-isomerization with Vibrational Coherence but Low Quantum Yield in *Anabaena* Sensory rhodopsin. *Phys. Chem. Chem. Phys.* **2015**, *17*, 25429-25439.
- (22) Doany, F. E.; Hochstrasser, R. M.; Greene, B. I.; Millard, R. R. Femtosecond Time-Resolved Ground-State Recovery of Cis-Stilbene in Solution. *Chem. Phys. Lett.* **1985**, *118*, 1-5.
- (23) Rothenberger, G.; Negus, D. K.; Hochstrasser, R. M. Solvent Influence on Photoisomerization Dynamics. *J. Chem. Phys.* **1983**, *79*, 5360-5367.

# Chapter 4: Ultrafast Photoreaction Dynamics of Light-Driven Sodium-Ion-Pumping Rhodopsin KR2 Revealed by Femtosecond Time-Resolved Absorption Spectroscopy

## 4.1 Introduction

Rhodopsins constitute an important group of the photoreceptor proteins that are widely distributed over the organisms including the higher animals and microbes<sup>1-3</sup>. While the animal rhodopsin primarily works as visual pigments, the microbial rhodopsin exhibits various unique functions such as the proton pump, halide ion pump, and biological light sensor<sup>1-7</sup>. From the structural viewpoint, these rhodopsins are composed of seven transmembrane- $\alpha$ -helices that possess the retinal chromophore inside. The chromophore is covalently bound to a lysine side chain via a protonated Schiff base linkage, imposing a positive charge on the chromophore. Thus, it had been believed that rhodopsins which pumps cations other than the proton does not exist because of the electronic repulsion between the positively charged chromophore and the cation. Surprisingly, however, the rhodopsins which functions as the outward light-driven sodium ion pump were recently discovered<sup>8,9</sup>, and KR2 of the marine bacterium *Krokinobacter eikastus* is the first sodium ion pump protein reported. Moreover, KR2 is recognized as a potential tool for optogenetics that allows optical control of the neural activity<sup>10-12</sup>. Therefore, KR2 is receiving considerable attention as a promising candidate for the opto-physiological applications, as well as the system to investigate the microscopic mechanism for the unique function of the cation pump<sup>8,12</sup>.

Physiological functions of the microbial rhodopsins are realized through a photocycle reaction. Upon photo-irradiation, the chromophore first undergoes ultrafast isomerization from the initial all-*trans* form to the 13-*cis* form<sup>13</sup>. This photoisomerization of the chromophore is followed by the photocycle reaction involving numbers of intermediates, such as the K, L, M, N, and O intermediates, accompanied with salient structural changes of the protein over the time

scale from nanosecond to second<sup>14-16</sup>. As with the typical rhodopsins, the K, L, M, and O intermediates were found in KR2.

Very recently, an X-ray crystallographic study has revealed the atomic-scale structure of the KR2 protein, giving detailed structural insights<sup>12,17</sup>. The reported structure of the amino acid residues around protonated retinal Schiff base (PRSB) is shown in Figure 4.1a, in comparison with that of bacteriorhodopsin (bR)<sup>18</sup> (Figure 4.1b), the well-studied microbial rhodopsin working as a light-driven proton pump. In the case of bR, the Asp85 residue acts as the counterion of the positively charged PRSB<sup>19</sup>. Upon formation of the M intermediate, the proton of the PRSB migrates to Asp85, and a subsequent relay of the protons accomplishes the proton pump from the cytoplasmic to the extracellular side<sup>20</sup>. In contrast, it was suggested that the counterion of PRSB in KR2 is Asp116. The X-ray crystallographic data suggested that Asp116 receives the proton of the PRSB and redirects to Asn112 and Ser70 in the M intermediate, opening a channel that allows a sodium ion to be transported<sup>12</sup>. This proton transfer is considered a key process, because the deprotonation of PRSB can reduce the electronic repulsion between the chromophore and the sodium ion, which enables the sodium ion transportation.

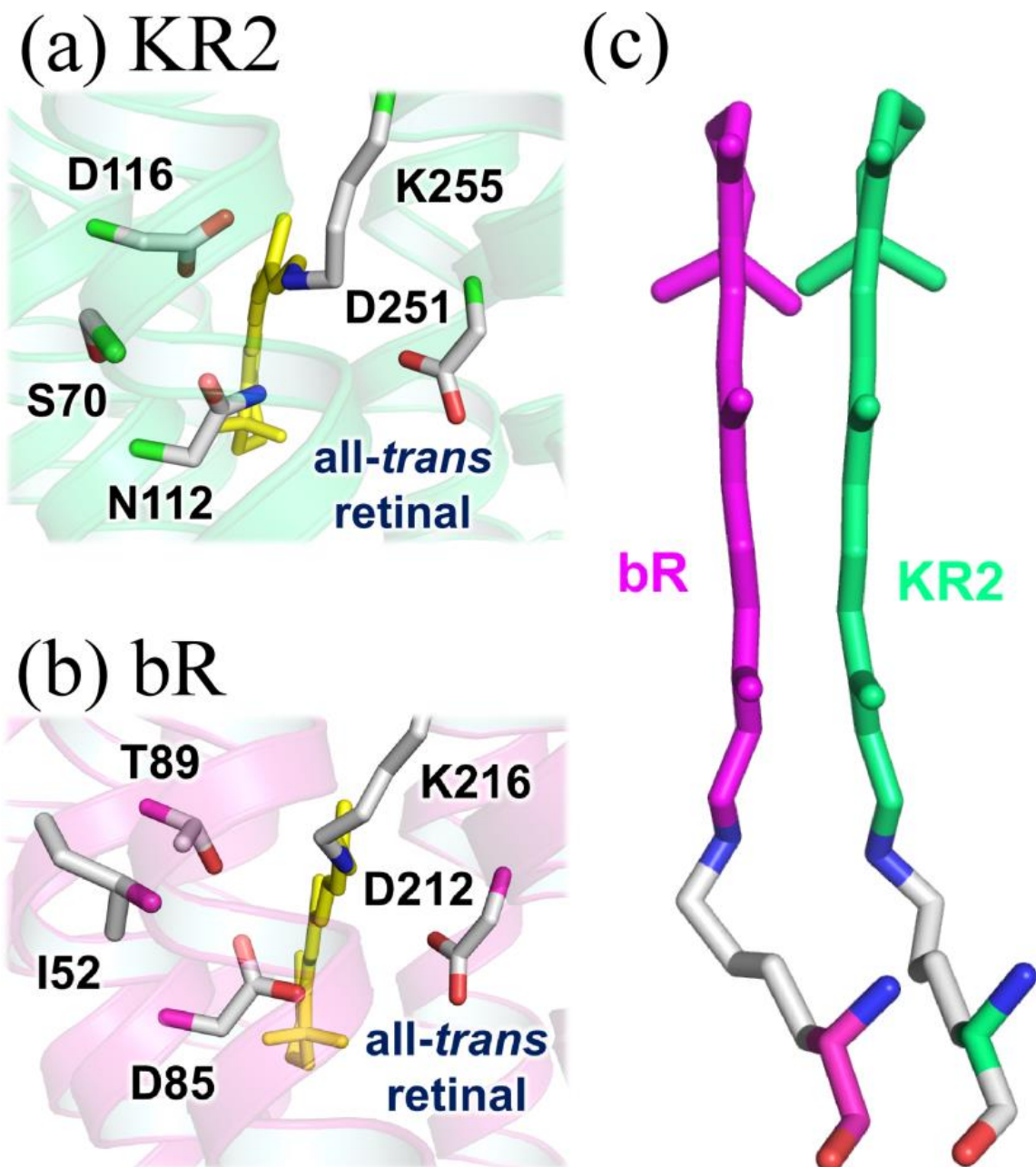


**Figure 4.1.** Schematic illustration of the molecular structure around the protonated retinal Schiff base region of (a) KR2, in comparison with that of (b) bR. The structure of KR2 is based on its crystallographic structure obtained at neutral pH<sup>12</sup> (PDB ID: 3X3C). The structure of bR was reported by Schobert et al.<sup>18</sup> (PDB ID: 1M0L). The retinal chromophore is colored in yellow. The atoms colored in green and pink correspond to the atoms connecting the side chain and the main chain of KR2 and bR, respectively. (c) Comparison of the chromophore part of the crystal structures of KR2 and bR.

The spectroscopic approach is powerful for elucidating the primary structural change of photoreceptor proteins<sup>21,22</sup>. So far, nanosecond time-resolved absorption spectroscopy on KR2 has shown a photoproduct band around 605 nm that is red-shifted from the dark-state absorption<sup>8</sup>. This photoproduct band is similar to the K-intermediate absorption of bR, suggesting that the K intermediate is also formed in KR2<sup>8,13</sup>. Fourier transform infrared spectroscopy at 77 K showed a difference spectrum between the K intermediate and the ground-state KR2 in the C-C stretch region, and demonstrated that it is also similar to the reported difference spectrum of bR<sup>13</sup>. These spectral similarities suggest that the isomerization of the chromophore from all-*trans* to 13-*cis* is involved in the formation process of the K intermediate of KR2, as in the case of bR. However, considering the unique arrangements of the amino acid residues around PRSB in KR2, it is expected that the protein environment suitable for the sodium ion pump is formed with photoexcitation, which leads to its distinct functional difference from bR. Therefore, it is important to examine the initial dynamics following the photoexcitation of the chromophore down to the formation of the K intermediate, for fully elucidating the mechanism that enables the sodium ion pump. Here, a femtosecond time-resolved absorption study of this firstly discovered sodium ion pump KR2 is reported.

## **4.2 Experimental Methods**

### **Sample preparation**

The KR2 sample was provided by Dr. Keiichi Inoue, Dr. Rei Abe-Yoshizumi and Prof. Hideki Kandori at Nagoya Institute of Technology. The sample was dissolved in a 50 mM Tris-HCl buffer at pH 8 containing 100 mM NaCl and 0.05% n-dodecyl- $\beta$ -D-maltoside (DDM).

### **Femtosecond time-resolved absorption spectroscopy**

Schematic of femtosecond absorption apparatus is depicted in Figure 4.2. The output of a Ti:sapphire amplifier system (800 nm, 1.2 mJ, 80 fs, 1 kHz, Legend Elite, Coherent) was divided into two. The 0.2 mJ portion was attenuated and focused into 3-mm-thick calcium fluoride (CaF<sub>2</sub>) to generate a white-light pulse that spectrally covers the whole visible region. The white-light pulse was divided into two, and they were used as probe and reference pulses. The

remaining 1 mJ portion was used to drive an optical parametric amplifier (TOPAS-C, Light Conversion), and its signal output at 1150 nm was frequency-doubled to generate a pump pulse at 575 nm. The pump polarization was set at the magic angle ( $54.7^\circ$ ) with respect to the horizontally polarized probe pulse. Both the pump and probe pulses were focused into a flow cell (1 mm path length), in which the sample solution was circulated. The circulation speed was optimized so that each laser shot irradiates a fresh portion of the sample. The probe pulse after passing through the sample and the reference pulse were spectrally analyzed by a polychromator (500is/sm, Chromex) equipped with a CCD camera (PIXIS-400F, Princeton Instruments). The time resolution of this measurement was evaluated as 100 fs from the FWHM of the temporal profile of a stimulated Raman gain signal due to water. The group delay dispersion of the white-light probe pulse was examined by the optical Kerr effect (OKE) measurement for the buffer, and it was used to calibrate the time origin at each wavelength.

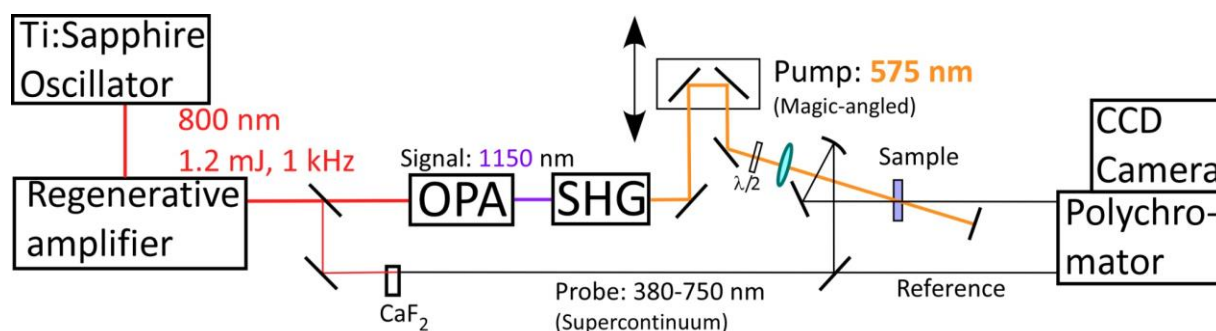


**Figure 4.2.** Schematic illustration of femtosecond time-resolved absorption apparatus.

### 4.3 Results & discussion

The steady-state absorption spectrum of KR2 in a buffer solution at pH 8 is shown at the bottom in Figure 4.3. It exhibits the absorption maximum at 525 nm due to the  $S_1 \leftarrow S_0$  transition of the retinal chromophore. In the femtosecond absorption measurement, the KR2 protein was photoexcited at the red side of the absorption (575 nm) to reduce the excess energy as much as possible. The obtained time-resolved absorption spectra in the 380-740 nm region are shown for selected delays in Figure 4.3. Immediately after photoexcitation, femtosecond absorption spectrum exhibited a positive band around 460 nm, a negative band around 550 nm and a negative band around 720 nm, which are assignable to the excited-state absorption (ESA), the ground-state bleaching (GSB), and the stimulated emission (SE), respectively. Both of the ESA and SE bands almost vanish by 1 ps, indicating that most of the excited-state population disappears within 1 ps. In accordance with the decay of the excited-state bands, another positive band gradually shows up around 620 nm, indicating the formation of photoproducts. This photoproduct absorption (PA) subsequently exhibits a ~30-nm blue shift within a few picoseconds, and becomes a long-lived band peaked around 590 nm that shows no further change within the time range of the measurements (200 ps). The blue shift of the PA band has also been observed for bR and sensory rhodopsins, and it has been attributed to the conversion from the first photoproduct (called J intermediate) to the K intermediate<sup>21,23-28</sup>. Therefore, the PA band observed at 620 nm is assignable to the J intermediate of KR2, which is subsequently relaxed to the K intermediate that exhibits the absorption maximum around 590 nm.

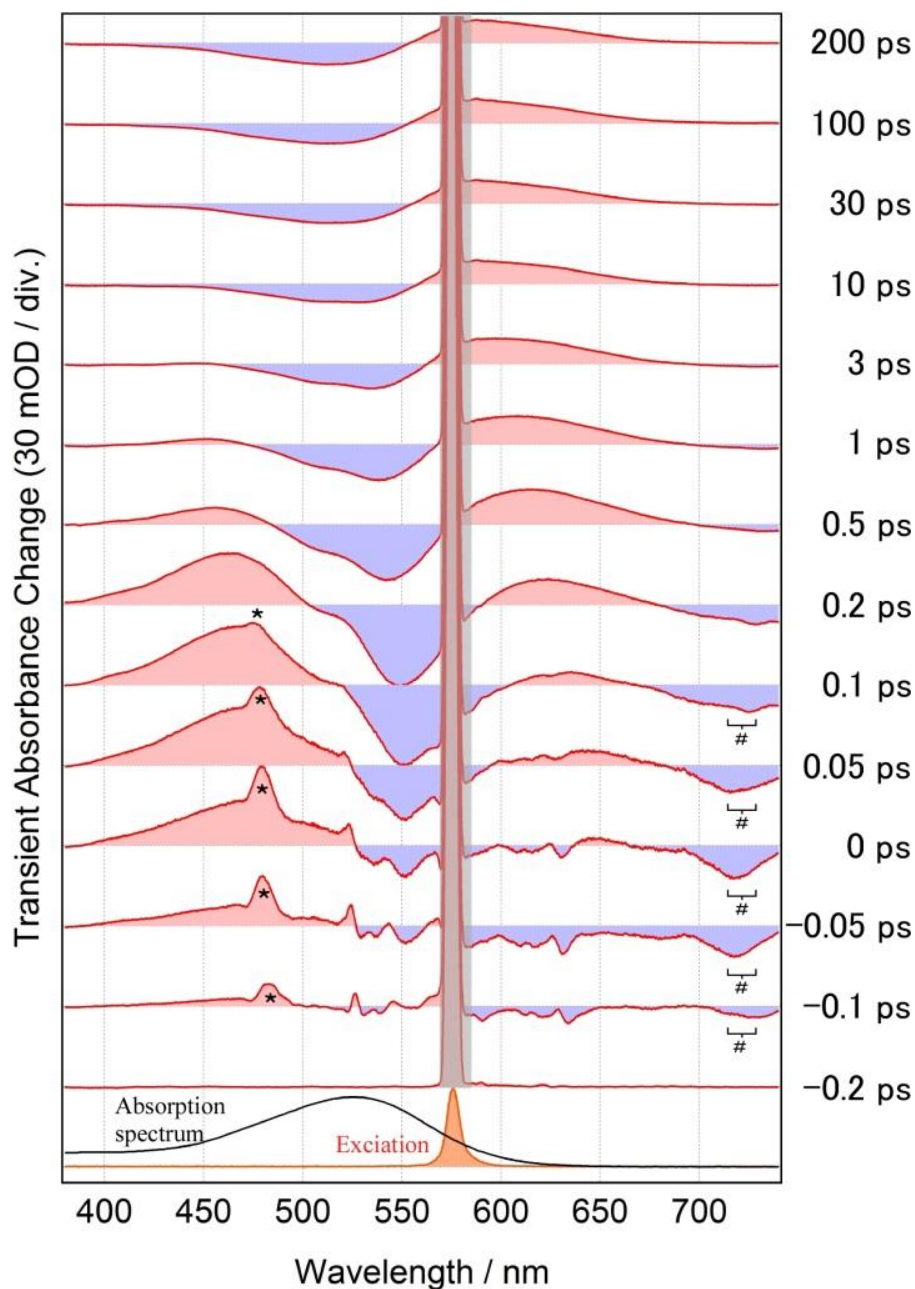


**Figure 4.3.** Femtosecond time-resolved absorption spectra of KR2 in a buffer solution at pH 8 measured with photoexcitation at 575 nm (240 nJ/pulse). The steady-state absorption spectrum of KR2 and the spectrum of the excitation pulse are also shown at the bottom. The spectral region shaded in gray is distorted by the scattering of the excitation beam. The \* marks represent spectral features due to the stimulated inverse Raman loss due to water. The # marks indicate the stimulated Raman gain signal of water that is superimposed on the stimulated emission band.

To examine the early-time dynamics more quantitatively, the time-resolved absorption data were analyzed by the global fitting analysis that takes account of the finite instrumental response. Temporal profiles of the time-resolved absorption signals at five typical wavelengths are shown in Figure 4.4 with the best fits obtained from the global analysis. The global fitting indicates that the fits using five common time constants ( $\tau_0 - \tau_4$ ) nicely reproduce the temporal profile at every wavelength, indicating that the primary dynamics of photoexcited KR2 can be accounted for by these five components. The amplitude of each component obtained by the global fitting analysis is summarized in Table 4.1. the ultrafast dynamics of KR2 is discussed based on the result of the global analysis in the following.

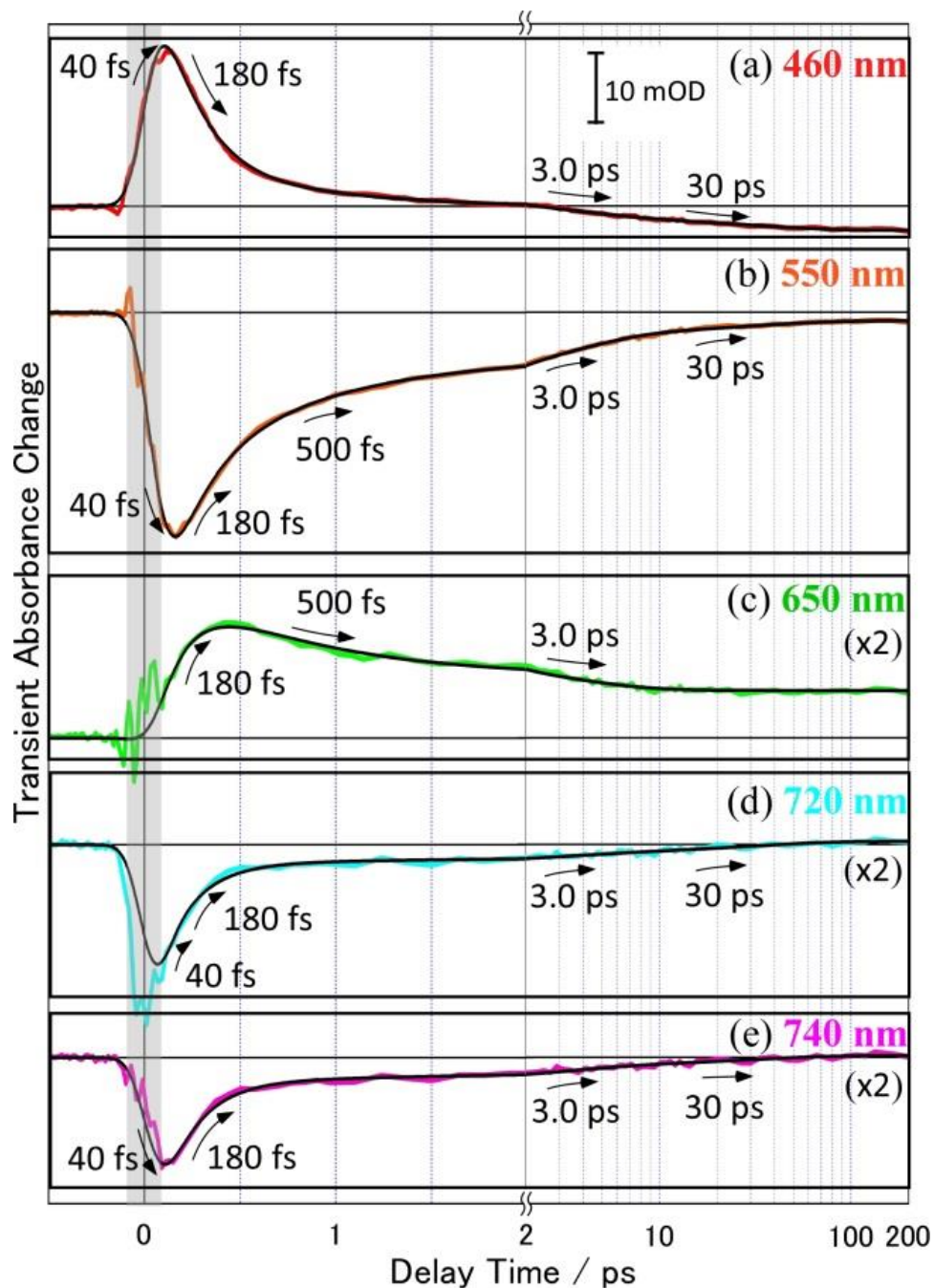


**Figure 4.4.** Temporal profiles of the femtosecond time-resolved absorption signals at (a) 460 nm, (b) 550 nm, (c) 650 nm, (d) 720 nm and (e) 740 nm measured with photoexcitation at 575 nm (240 nJ/pulse). The black solid curve drawn for each trace depicts the fits. Note that the horizontal scale is changed from the linear to the logarithmic scale after 2 ps. The time region shaded in gray is distorted by unwanted instantaneous responses, such as coherent artifacts and Raman scattering of water.

**Table 4.1.** Time constant and amplitude of each component obtained by the global fitting analysis of the femtosecond time-resolved absorption signals.

$\lambda_{\text{obs}}$	$\tau_0$ (40 fs)	$\tau_1$ (180 fs)	$\tau_2$ (500 fs)	$\tau_3$ (3.0 ps)	$\tau_4$ (30 ps)
460 nm	-0.20	0.87	0.00	0.05	0.08
550 nm	1.40	-0.56	-0.31	-0.10	-0.03
650 nm	0.00	-1.78	0.64	0.32	0.03
720 nm	-0.46	-0.48	0.00	-0.02	-0.04
740 nm	0.58	-0.87	0.00	-0.08	-0.05

Sum of the amplitudes of the decay components is normalized to 1 at each wavelength.

As clearly seen, the temporal profile of ESA at 460 nm and those of SE at 720 and 740 nm exhibit a comparable decay that is well characterized by common three time constants of  $\tau_1 = 180$  fs,  $\tau_3 = 3.0$  ps, and  $\tau_4 = 30$  ps. This implies that the decay of the  $S_1$  state of KR2 is not a simple single exponential decay but contains several components. Nevertheless, the  $\tau_1$  component (180 fs) most predominantly contributes to the signal, and this main relaxation in KR2 is substantially faster than that in bR ( $\sim 500$  fs)<sup>21,23,24,26</sup>.

In accordance with the fast relaxation of the  $S_1$  state, the PA band due to the J intermediate grows up around 620 nm, and its rise time is evaluated as  $\sim 180$  fs, as seen for the time-resolved signal at 650 nm shown in Figure 4.4c. This rise time coincides with the  $\tau_1$  component of the  $S_1$  decay, indicating that the J intermediate is directly formed through the deactivation of the  $S_1$  state with the time constant of  $\tau_1$ . In other words, the  $S_1$  population having the  $\tau_1 = 180$  fs lifetime acts as a precursor of the J intermediate, and hence this  $S_1$  state is called the reactive  $S_1$  state, hereafter. The  $S_1$  population having the  $\tau_3 = 3.0$  ps and  $\tau_4 = 30$  ps

lifetimes yields no photoproducts, because the PA signal does not show such slower rise components, so that these states are called the non-reactive  $S_1$  state.

The PA signal at 650 nm shows an apparent decay with a time constant of  $\tau_2 = 500$  fs. The wavelength of 650 nm corresponds to the red side of the PA band, and this time constant represents the blue shift of the PA band, which is readily recognized in the time-resolved spectra shown in Figure 4.3. This implies that the J intermediate is converted to the K intermediate with  $\tau_2 = 500$  fs in KR2. After the J $\rightarrow$ K conversion, the PA signal apparently shows a slight decay with a time constant of  $\sim 3$  ps. Because this time constant is very close to the  $\tau_3$  value, it is tempting to consider that the ESA of one of the non-reactive  $S_1$  population is spectrally overlapped with the PA band and is observed at this particular wavelength of 650 nm. However, it is rather considered that it is more likely that the  $\sim 3$ -ps dynamics observed at 650 nm is caused by the vibrational cooling process of the vibrationally-hot  $S_0$  state that is generated by the internal conversion of the reactive  $S_1$  population. In fact, the GSB partially recovers with  $\tau_1 = 180$  fs (Figure 4.4b), indicating that the reactive  $S_1$  population not only generates the J intermediate but also relaxes into the original  $S_0$  state by the internal conversion. It is expected that the  $S_0$  population generated by this fast internal conversion is vibrationally hot and hence shows a red-shifted absorption compared to that of the steady-state absorption of the initial  $S_0$  state. Thus, the vibrational cooling of the hot  $S_0$  population would be observed as the decrease in the absorption intensity at the longer wavelength side of the  $S_1 \leftarrow S_0$  absorption. It should be noted that an additional temporal change with a typical time constant of  $\tau_0 = 40 \pm 20$  fs is also observed immediately after photoexcitation. This ultrafast component corresponds to the blue shift of ESA and the red shift of SE, implying that it arises from the initial motion of the  $S_1$  population from the Franck-Condon state to the relaxed  $S_1$  state. A similar ultrafast spectral dynamics has also been observed for other rhodopsins<sup>26,27,29,30</sup>.

Figure 4.5 illustrates the relaxation dynamics of photoexcited KR2 from the initial photoexcitation to the formation of the K intermediate, which has been revealed by the present study. Photoexcitation at 575 nm first generates the  $S_1$  state in the Franck-Condon region, which exhibits the characteristic ESA at 460 nm and SE at 720 nm. This initial Franck-Condon state is rapidly relaxed in the  $S_1$  state with  $\tau_0 = 40$  fs, which is accompanied with the blue shift of ESA and red shift of SE. This relaxed  $S_1$  state is the precursor of the subsequent photocycle of

KR2, i.e., the reactive  $S_1$  state. The reactive  $S_1$  state undergoes the rapid internal conversion with  $\tau_1 = 180$  fs, which involves isomerization of the retinal chromophore, and is directly converted to the J intermediate exhibiting the PA band at 620 nm. The J intermediate is subsequently converted to the K intermediate with  $\tau_2 = 500$  fs, which is characterized by the  $\sim 30$ -nm blue shift of the PA band. A portion of the reactive  $S_1$  population is branched into the original  $S_0$  state upon the internal conversion, and generates the vibrationally-hot  $S_0$  population. The hot  $S_0$  population is relaxed back to the initial  $S_0$  state through the vibrational cooling that proceeds in a few picoseconds.

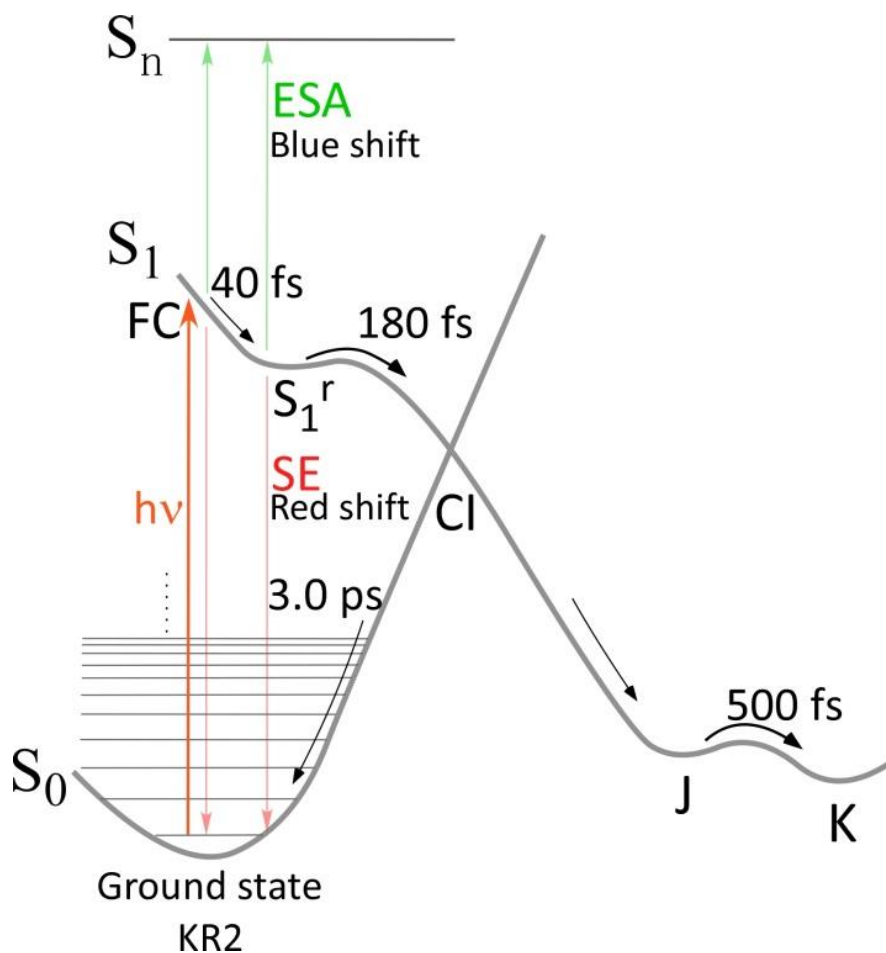


**Figure 4.5.** Schematic illustration of the primary relaxation pathway and dynamics of the reactive  $S_1$  state ( $S_1^r$ ) of the KR2 protein. The dynamics relevant to the non-reactive  $S_1$  states are not shown (see text). FC: Franck-Condon state. CI: conical intersection.

The present study showed that the  $S_1$  state of KR2 is relaxed and converted to the J intermediate with a time constant as short as 180 fs. This implies that  $S_1 \rightarrow J$  relaxation which involves the isomerization of chromophore, proceeds three times faster than the corresponding process in bR ( $\sim 500$  fs)<sup>21,23,24,26</sup>. It is considered that this substantial difference in the relaxation rate could be correlated with distinct differences in the amino-acid arrangement around the PRSB. As shown in Figure 4.1, the position of the Asp 116, the counterion of the PRSB, in KR2 is shifted toward the cytoplasmic side by one pitch of the  $\alpha$ -helix compared to that in bR, which is expected to induce some structural difference of the chromophore in KR2 and bR. In fact, the direct comparison of the crystal structures between KR2 (taken with 2.3 Å resolution) and bR (taken with 1.47 Å resolution) in Figure 4.1c seems to suggest that the Schiff base moieties of their chromophores are distorted differently<sup>12,18</sup>, although the resolutions of the crystallographic data are limited. It is considered that the distortion of the chromophore modifies the potential energy surfaces of the  $S_0$  and  $S_1$  states, including the  $S_0 - S_1$  crossing region such as the conical intersection, which facilitates the efficient  $S_1 \rightarrow J$  internal conversion in KR2. It is noteworthy that the  $J \rightarrow K$  conversion in KR2 ( $\tau_2 = 500$  fs) also proceeds remarkably faster than the corresponding process in bR ( $\sim 3$ -5 ps)<sup>24-26</sup>. This implies that the photocycle reactions in the electronically ground state are also affected by the characteristic amino-acid arrangement around PRSB.

#### 4.4 Conclusions

The ultrafast photoreaction dynamics of recently discovered sodium-ion-pumping rhodopsin KR2 at pH 8 was investigated by femtosecond time-resolved absorption spectroscopy. The obtained data show that the  $S_1$  state of KR2 deactivates and undergoes photoisomerization with a time constant of 180 fs. This process of KR2 is three times faster than that of bacteriorhodopsin. In accordance with the  $S_1 \rightarrow S_0$  internal conversion, the J intermediate is formed. The J intermediate is subsequently converted to the K intermediate, which is followed by the photocycle reaction. Based on the direct comparison of the crystal structures of KR2 and bR, it is suggested that the photoisomerization process is accelerated due to the difference in distortion of the Schiff base moieties of KR2 and bR.

## 4.5 References

- (1) Filipek, S.; Stenkamp, R. E.; Teller, D. C.; Palczewski, K. G Protein-coupled Receptor Rhodopsin: A Prospectus. *Annu. Rev. Physiol.* **2003**, *65*, 851-79.
- (2) Haupts, U.; Tittor, J.; Oesterhelt, D. Closing in on Bacteriorhodopsin: Progress in Understanding the Molecule. *Annu. Rev. Biophys. Biomol. Struct.* **1999**, *28*, 367-99.
- (3) Ernst, O. P.; Lodowski, D. T.; Elstner, M.; Hegemann, P.; Brown, L. S.; Kandori, H. Microbial and Animal Rhodopsins: Structures, Functions, and Molecular Mechanisms. *Chem. Rev.* **2014**, *114*, 126-163.
- (4) Spudich, J. L.; Yang, C. S.; Jung, K. H.; Spudich, E. N. Retinylidene Proteins: Structures and Functions from Archaea to Humans. *Annu. Rev. Cell. Dev. Biol.* **2000**, *16*, 365-92.
- (5) Racker, E.; Stoeckenius, W. Reconstitution of Purple Membrane Vesicles Catalyzing Light-driven Proton Uptake and Adenosine Triphosphate Formation. *J. Biol. Chem.* **1974**, *249*, 662-663.
- (6) Schobert, B.; Lanyi, K. Halorhodopsin is a Light-driven Chloride Pump. *J. Biol. Chem.* **1982**, *257*, 10306-10313.
- (7) Spudich, J. L.; Bogomolni, R. A. Mechanism of Colour Discrimination by a Bacterial Sensory Rhodopsin. *Nature* **1984**, *312*, 509-513.
- (8) Inoue, K.; Ono H.; Abe-Yoshizumi, R.; Yoshizawa, S.; Ito, H.; Kogure, K.; Kandori, H. A Light-driven Sodium Ion Pump in Marine Bacteria. *Nat. Commun.* **2013**, *4*, 1678.
- (9) Balashov, S. P.; Imasheva, E.S.; Dioumaev, A. K.; Wang, J. M.; Jung, K. H.; Lanyi, J. K. Light-driven Na<sup>+</sup> Pump from *Gillisia limnaea*: A high-affinity Na<sup>+</sup> Binding Site is Formed Transiently in the Photocycle. *Biochemistry*, **2014**, *53*, 7549-7561.
- (10) Boyden, E. S.; Zhang, F.; Bamberg, E.; Nagel, G.; Deisseroth, K. Millisecond-timescale, Genetically Targeted Optical Control of Neural Activity. *Nat. Neurosci.* **2005**, *8*, 1263-1268.
- (11) Chow, B. Y.; Han, X.; Dobry, A. S.; Qian, X.; Chuong, A. S.; Li, M.; Henninger, M. A.; Belfort, G. M.; Lin, Y.; Monahan, P. E.; Boyden, E. S. High-performance Genetically Targetable Optical Neural Silencing by Light-driven Proton Pumps. *Nature*, **2010**, *463*, 98-102.
- (12) Kato, H. E., Inoue, K., Abe-Yoshizumi, R.; Kato, Y.; Ono, H.; Konno, M. Hososhima, S.; Ishizuka, T.; Hoque, M. R.; Kunitomo, H.; Ito, J.; Yoshizawa, S.; Yamashita, K.; Takemoto, M.; Nishizawa, T.; Taniguchi, R.; Kogure, K.; Maturana, A. D.; Ino, Y.; Yawo, H.; Ishitani, R.; Kandori, H.; Nureki, O. Structural Basis for Na<sup>+</sup> Transport Mechanism by a Light-driven Na<sup>+</sup> Pump. *Nature* **2015**, *521*, 48-53.
- (13) Ono, H.; Abe-Yoshizumi, R.; Kandori, H. FTIR Spectroscopy of a Light-driven Compatible Sodium Ion-proton pumping Rhodopsin at 77 K. *J. Phys. Chem. B* **2014**, *118*, 4784-4792.
- (14) Lozier, R. H.; Bogomolni, R. A.; Stoeckenius, W. Bacteriorhodopsin: A Light-driven Proton Pump in Halobacterium Halobium. *Biophys. J.* **1975**, *15*, 955-962.
- (15) Váró, G.; Zimányi, L.; Fan, X.; Sun, L.; Needleman, R.; Lanyi, J. K. Photocycle of Halorhodopsin from *Halobacterium Salinarium*. *Biophys. J.* **1995**, *68*, 2062-2072.

- (16) Suzuki, D.; Furutani, Y.; Inoue, K.; Kikukawa, T.; Sakai, M.; Fujii, M.; Kandori, H.; Homma, M.; Sudo, Y. Effects of Chloride Ion Binding on the Photochemical Properties of *Salinibacter* Sensory Rhodopsin I. *J. Mol. Biol.* **2009**, *392*, 48-62.
- (17) Gushchin, I.; Shevchenko, V.; Polovinkin, V.; Kovalev, K.; Alekseev, A.; Round, E.; Borshchevskiy, V.; Balandin, T.; Popov, A.; Gensch, T.; Fahlke, C.; Bamann, C.; Willbold, D.; Büldt, G.; Bamberg, E.; Gordeliy, V. Crystal Structure of a Light-driven Sodium Pump. *Nat. Struct. Mol. Biol.* **2015**, *22*, 390-395.
- (18) Schobert, B.; Cupp-Vickery, J.; Hornak, V.; Smith, S.; Lanyi, J. Crystallographic structure of the K intermediate of bacteriorhodopsin: conservation of free energy after photoisomerization of the retinal. *J. Mol. Biol.* **2002**, *321*, 715-726.
- (19) Needleman, R.; Chang, M.; Ni, Baofu.; Váró, G.; Fornés, J.; White, S. H.; Lanyi, J. K. Properties of Asp<sup>212</sup> → Asn Bacteriorhodopsin Suggest That Asp<sup>212</sup> and Asp<sup>85</sup> Both Participate in a Counterion and Proton Acceptor Complex near the Schiff Base. *J. Biol. Chem.* **1991**, *266*, 11478-11484.
- (20) Metz, G.; Siebert, F.; Engelhard, M. Asp<sup>85</sup> is the Only Internal Aspartic Acid That Gets Protonated in the M Intermediate and the Purple-to-blue Transition of Bacteriorhodopsin A solid-state <sup>13</sup>C CP-MAS NMR investigation. *FEBS Lett.* **1992**, *303*, 237-241.
- (21) Nuss, M. C.; Zinth, W.; Kaiser, W.; Kölling, E.; Oesterhelt, D. Femtosecond Spectroscopy of the First Events of the Photochemical Cycle in Bacteriorhodopsin. *Chem. Phys. Lett.* **1985**, *117*, 1-7.
- (22) Schoenlein, R. W.; Peteanu, L. A.; Mathies, R. A.; Shank, C. V. The First Step in Vision: Femtosecond Isomerization of Rhodopsin. *Science*. **1991**, *254*, 412-415.
- (23) Pollard, H. J.; Franz, M. A.; Zinth, W.; Kaiser, W.; Kölling, E.; Oesterhelt, D. Early Picosecond Events in the Photocycle of Bacteriorhodopsin. *Biophys. J.* **1986**, *49*, 651-662.
- (24) Petrich, J. W.; Breton, J.; Martin, J. L.; Antonetti, A. Femtosecond Absorption Spectroscopy of Light-adapted and Dark-adapted Bacteriorhodopsin. *Chem. Phys. Lett.* **1987**, *137*, 369-375.
- (25) Sharkov, A. V.; Pakulev, A. V.; Chekalin, S. V.; Matveetz, Y. A. Primary Events in Bacteriorhodopsin Probed by Subpicosecond Spectroscopy. *Biochim. Biophys. Acta* **1985**, *808*, 94-102.
- (26) Mathies, R. A.; Cruz, C. H. B.; Pollard, W. T.; Shank, C. V. Direct Observation of the Femtosecond Excited-State *cis-trans* Isomerization in Bacteriorhodopsin. *Science* **1988**, *240*, 777-779.
- (27) Sudo, Y.; Mizuno, M.; Wei, Z.; Takeuchi, S.; Tahara, T. The Early Steps in the Photocycle of a Photosensor Protein Sensory Rhodopsin I from *Salinibacter Ruber*. *J. Phys. Chem. B* **2014**, *118*, 1510-1518.
- (28) Lutz, I.; Sieg, A.; Wegener, A. A.; Engelhard, M.; Boche, I.; Otsuka, M.; Oesterhelt, D.; Wachtveitl, J.; Zinth, W. Primary Reaction of Sensory Rhodopsins. *Proc. Natl. Acad. Sci. USA* **2001**, *98*, 962-967.

(29) Nakamura, T.; Takeuchi, S.; Shibata, M.; Demura, M.; Kandori, H.; Tahara, T. Ultrafast Pump-probe Study of the Primary Photoreaction Process in *Pharaonis* Halorhodopsin: Halide Ion Dependence and Isomerization Dynamics. *J. Phys. Chem. B* **2008**, *112*, 12795-12800.

(30) Dobler, J.; Zinth, W.; Kaiser, W. Excited-state of bacteriorhodopsin studied by femtosecond spectroscopy. *Chem. Phys. Lett.* **1988**, *144*, 215-210.

# Chapter 5: pH-Dependent Formation of Reactive and Non-Reactive Excited States of Sodium-Ion-Pumping Rhodopsin KR2 Revealed by Femtosecond Time-Resolved Absorption Spectroscopy

## 5.1 Introduction

In general, proteins lose their higher-order structure when pH or temperature condition is far from optimum. However, the structures of rhodopsins are reported to be robust against these chemical conditions. For example, according to the reported crystal structure, bacteriorhodopsin (bR) preserves the higher-order structure even at pH 2<sup>1</sup>. In spite of the robustness of the structure, it has been revealed that the absorption spectra and the photoreactions of rhodopsins are sensitive to the pH value. As for bR, Asp 85, the counterion of the PRSB at neutral pH, is protonated at pH below 2 (pKa ~ 2.2)<sup>2,3</sup>. The protonation of the Asp 85 induces the red shift of the S<sub>1</sub>←S<sub>0</sub> absorption spectrum (570→605 nm)<sup>4</sup>, and modifies the photoreaction. When the Asp 85 is protonated, bR does not form the M intermediate<sup>5</sup>, indicating that the protonation of the Asp 85 inhibits the photocycle reaction and eradicates the proton pump function. Not only these slow dynamics but also ultrafast dynamics is affected by pH value. The S<sub>1</sub> lifetime becomes one order of magnitude longer than that at neutral pH<sup>6,7</sup>. This shows that not only the photocycle reaction but also the photoisomerization dynamics of bR is affected by the protonation of the Asp 85.

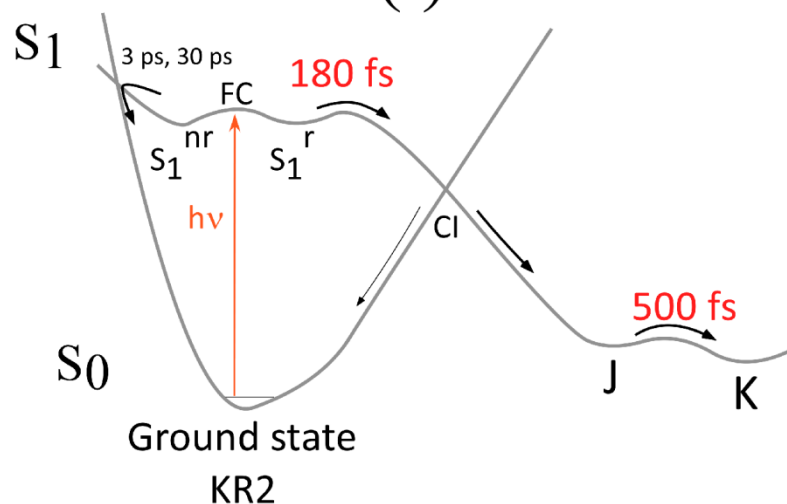
In the case of KR2, a firstly reported light-driven sodium ion pump rhodopsin, the S<sub>1</sub>←S<sub>0</sub> absorption spectrum shifts at acidic pH (525→550 nm) as in the case of bR<sup>8</sup>, indicating that the properties of the unphotolyzed state are changed from that at neutral pH. However, in spite of such a property change in the unphotolyzed state at acidic pH, the K intermediate is formed upon photoexcitation as in the case of neutral condition. As already described in the previous chapter, the femtosecond absorption data at pH 8 showed that the reactive S<sub>1</sub> state (S<sub>1</sub><sup>†</sup>) having the lifetime of  $\tau_1 = 180$  fs undergoes photoisomerization and generates the K intermediate<sup>9</sup>.

This implies that the photoexcitation of KR2 in the unphotolyzed state yields the  $S_1^f$  state also at acidic pH in spite of the change in the property of the unphotolyzed state. This fact lets us wonder what the origin of the  $S_1^f$  state is.

The photoexcitation of KR2 yields not only the  $S_1^f$  state but also the non-reactive  $S_1$  state ( $S_1^{nr}$ ) state that does not give any photoproduct and relaxes back to the original ground state. As the origin of the  $S_1^f$  and  $S_1^{nr}$  states of sensory rhodopsins, proteorhodopsin and halorhodopsin<sup>10-13</sup>, it was proposed that the  $S_1$  state in the Franck-Condon region is branched into different regions of the  $S_1$  potential energy surface, giving rise to the  $S_1^f$  and  $S_1^{nr}$  states that are relaxed to the  $S_0$  state through different pathways (Figure 5.1a). However, it is also very plausible that the initial KR2 in the  $S_0$  state has inhomogeneity, and that each component is excited separately and can show different excited-state dynamics in parallel (Figure 5.1b). These two mechanisms, i.e., branching at the Franck-Condon region in the  $S_1$  state and the inhomogeneity in the initial  $S_0$  state, are essentially different from each other.

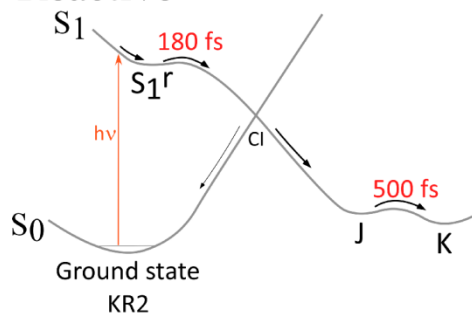
In this study, femtosecond absorption measurements at various pHs ranging from 4 to 11 were investigated to elucidate the origin of the  $S_1^f$  and  $S_1^{nr}$  states. Based on the pH titration curve of the yield of the  $S_1^f$  state, the formation mechanism of the  $S_1^f$  and  $S_1^{nr}$  is discussed.

## Mechanism (i)



## Mechanism (ii)

Reactive



Non-reactive

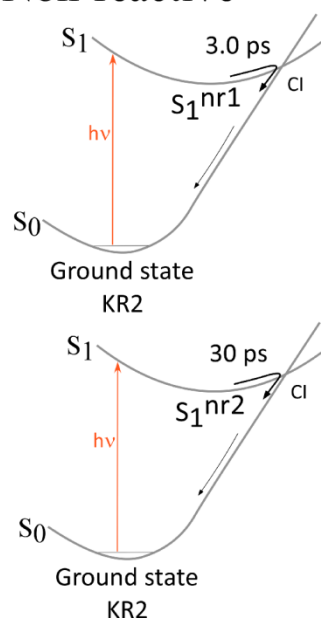


**Figure 5.1.** Schematic illustration of the two possible origins of the  $S_1^r$  and  $S_1^{nr}$  states. Mechanism (i): The branching at the Franck-Condon state generates the  $S_1^r$  and  $S_1^{nr}$  states. Mechanism (ii): Two species exist in the ground state, and the photoexcitation of each species yields the  $S_1^r$  and  $S_1^{nr}$  states. FC: Franck-Condon state, CI: conical intersection

## 5.2 Experimental methods

### Sample preparation

The KR2 and D116N samples were provided by Dr. Keiichi Inoue, Dr. Rei Abe-Yoshizumi and Prof. Hideki Kandori at Nagoya Institute of Technology. The composition of the buffer was carefully selected to keep the sodium ion concentration constant (100 mM) at each pH (Table. 5.1). The D116N mutant was dissolved in buffer at pH 8. The absorption spectrum at each pH is shown in Figure 5.2.

**Table 5.1.** Buffer composition at each pH.

pH	buffer
4-7	50 mM citrate-Tris, 100 mM NaCl, 0.05% n-dodecyl- $\beta$ -D-maltoside (DDM)
8	50 mM Tris-HCl, 100 mM NaCl, 0.05% DDM
9	50 mM Tris-citrate, 100 mM NaCl, 0.05% DDM
10	50 mM CAPS-NaOH, 89 mM NaCl, 0.05% DDM
11	50 mM CAPS-NaOH, 62 mM NaCl, 0.05% DDM

Tris: tris(hydroxymethyl) aminomethane, CAPS: N-Cyclohexyl-3-aminopropanesulfonic acid

### Femtosecond time-resolved absorption spectroscopy

The experimental method for femtosecond time-resolved absorption measurement is described in chapter 4. The pump pulse energy at each pH is summarized in Table 5.2.

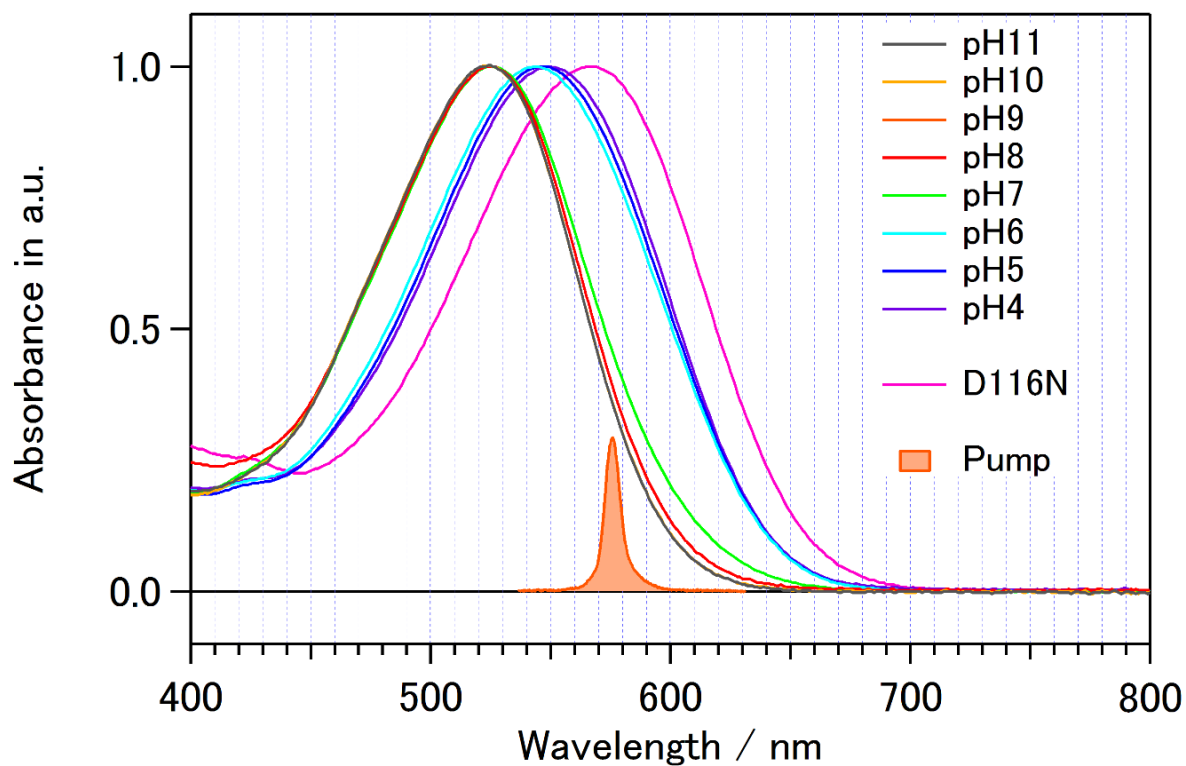


**Figure 5.2.** Absorption spectra of the KR2 samples ranging from pH 4 to 11 and D116N mutant at pH 8. The spectrum of the pump pulse used in femtosecond time-resolved absorption measurement is also shown.

**Table 5.2.** Pump energy used at each pH.

pH	Pulse energy / nJ
4	120
5	160
6-8	240
9-11	400

### 5.3 Results & discussion

Femtosecond time-resolved absorption spectra of KR2 at pH 4 are shown in Figure 5.3. Immediately after photoexcitation, a positive band around 500 nm, femtosecond absorption spectrum exhibited a negative band around 560 nm and a negative band around 720 nm, which are assignable to the excited-state absorption (ESA), the ground-state bleaching (GSB), and the stimulated emission (SE), respectively. Both ESA and SE signals persist longer than 100 ps, indicating that the excited-state population survives longer than this delay. In accordance with the decay of the excited-state bands, the recovery of the GSB takes place. After 10 ps, a positive band becomes visible around 640 nm, which is assignable to the absorption band of the long-lived photoproduct (PA), and it shows no further change within the time range of our measurements (900 ps). As compared with the time-resolved spectra at pH 8<sup>9</sup>, the amplitude of the PA band is significantly smaller at pH 4, indicating that the quantum yield of the K intermediate is lower at pH 4. This suggests that most part of the transient signal is due to the  $S_1^{\text{nr}}$  state at pH 4. The direct comparison of the femtosecond spectra at pH 4 and 8 manifests that the dynamics at pH 4 is apparently slow with respect to that at pH 8. At pH 8, the transient signal was composed of the dominant reactive  $S_1$  state ( $S_1^{\text{r}}$ ) with a lifetime of 180 fs and the minor non-reactive  $S_1$  states ( $S_1^{\text{nr}}$ ) with lifetimes of 3 ps and 30 ps<sup>9</sup>. The apparently slower dynamics at pH 4 can be rationalized by the decrease in the amplitude of the fast decaying  $S_1^{\text{r}}$  component and the increase in the slower  $S_1^{\text{nr}}$  components.

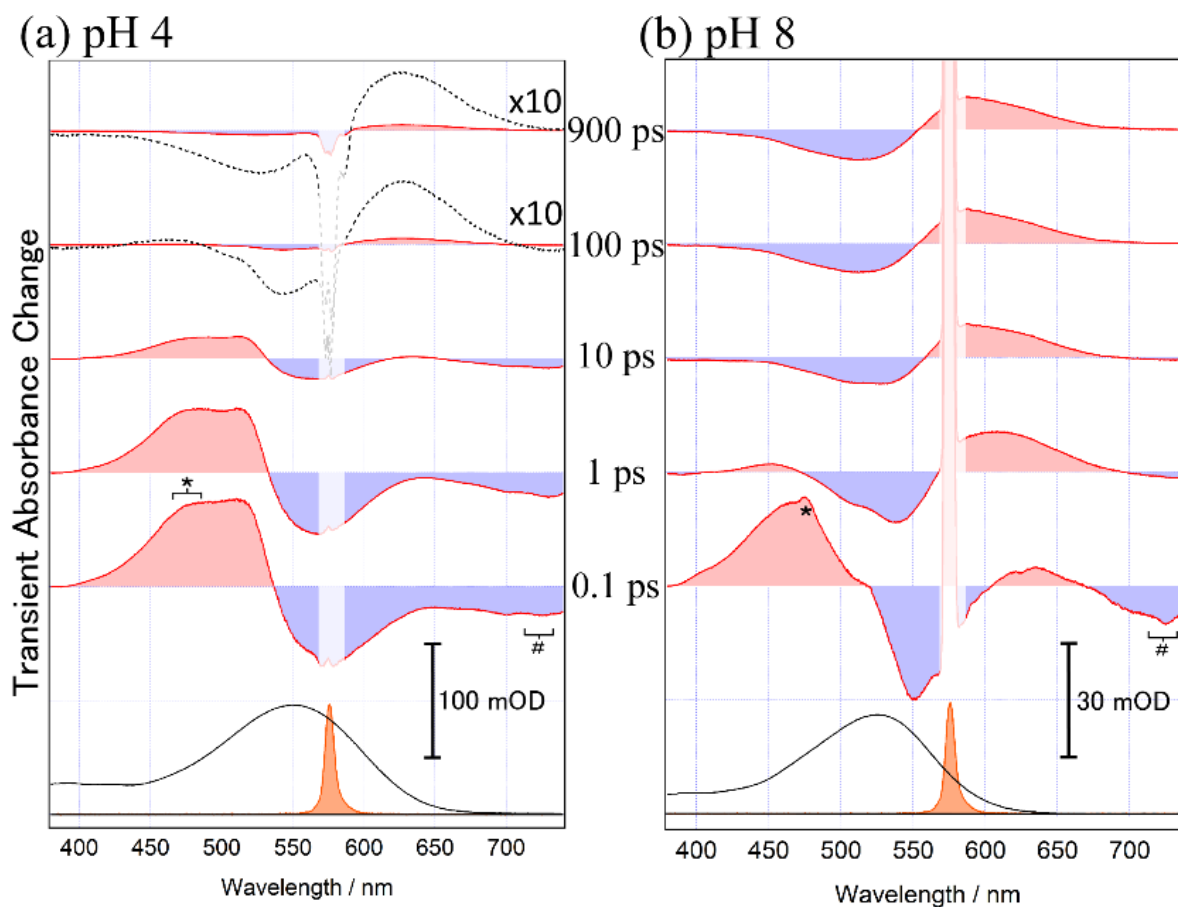


**Figure 5.3.** Femtosecond time-resolved absorption spectra of KR2 in buffer solutions at (a) pH 4 and (b) pH 8 measured with photoexcitation at 575 nm. (The pump energy is listed in Table 5.2.) The steady-state absorption spectrum of KR2 and the spectrum of the excitation pulse are also shown at the bottom. The spectral region shaded is distorted by the scattering of the excitation beam. The \* marks indicate that the stimulated inverse Raman loss due to water is superimposed on the excited-state absorption. The # marks indicate the stimulated Raman gain signal of water that is superimposed on the stimulated emission band.

To extract the  $S_1$  dynamics at pH 4 from the time-resolved spectrum, the kinetics at selected wavelengths were constructed as shown in Figure 5.4. The signals at 460 and 720 nm corresponding to the ESA and SE almost completely decayed within 200 ps. The kinetics at 650 and 720 nm clearly exhibit a subpicosecond component whose time constant is similar to the lifetime of  $S_1^r$  state at pH 8, suggesting that the  $S_1^r$  state is generated even at pH 4. For

comparison, the kinetics at pH 8 are also shown in broken gray lines in Figure 5.4. Obviously, the overall dynamics at pH 4 is apparently slow compared with that at pH 8, again implying that the fast decaying  $S_1^r$  component decreases and that the slow  $S_1^{nr}$  components increase at pH 4. To examine the dynamics at pH 4 more quantitatively, the global fitting analysis that takes account of the finite instrumental response was performed. The best fits obtained from the global analysis are shown in black lines in Figure 5.4. The global fitting indicates that the fits using five common time constants ( $\tau_0 - \tau_4$ ) nicely reproduces the temporal profiles, indicating that the primary dynamics of photoexcited KR2 at pH 4 can be accounted for by these five components. The amplitude of each component obtained by the global fitting analysis is summarized in Table 5.3. The fastest component ( $\tau_0 \sim 30$  fs) was observed as rise components of the ESA and SE. Therefore, this component is assignable to the initial relaxation toward the relaxed  $S_1$  state as in the case of KR2 at pH 8.

**Table 5.3.** Time constant and amplitude of each component obtained by the global fitting analysis of the femtosecond time-resolved absorption signals at pH 4.

$\lambda_{\text{obs}}$	$\tau_0$ (30 fs)	$\tau_1$ (180 fs)	$\tau_2$ (1.3 ps)	$\tau_3$ (7.0 ps)	$\tau_4$ (43 ps)
460 nm	-0.07	0.06	0.47	0.29	0.18
550 nm	0.23	0.00	-0.41	-0.41	-0.18
650 nm	0.00	-0.53	-0.19	-0.12	-0.16
720 nm	0.00	-0.30	-0.17	-0.32	-0.21
740 nm	0.11	-0.29	-0.18	-0.32	-0.21

Sum of the amplitudes of the decay components is normalized to 1 at each wavelength.

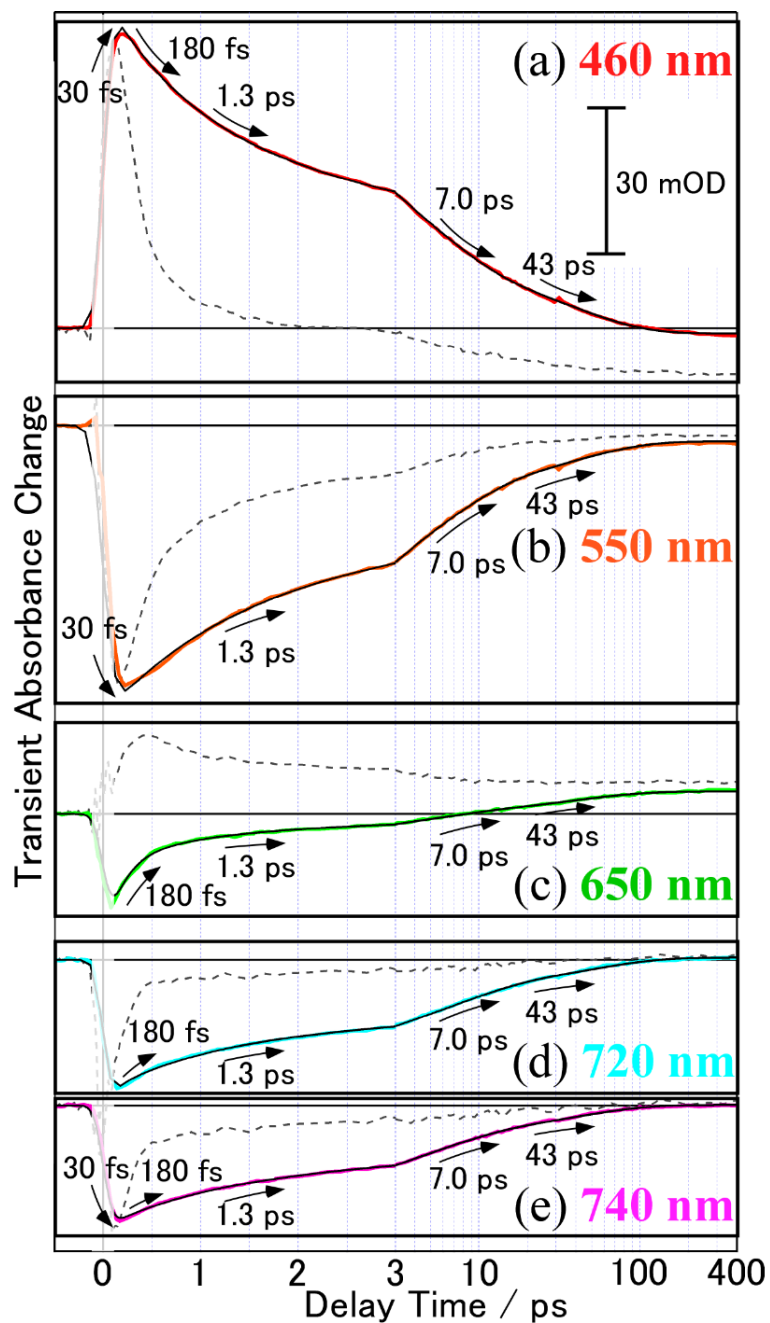


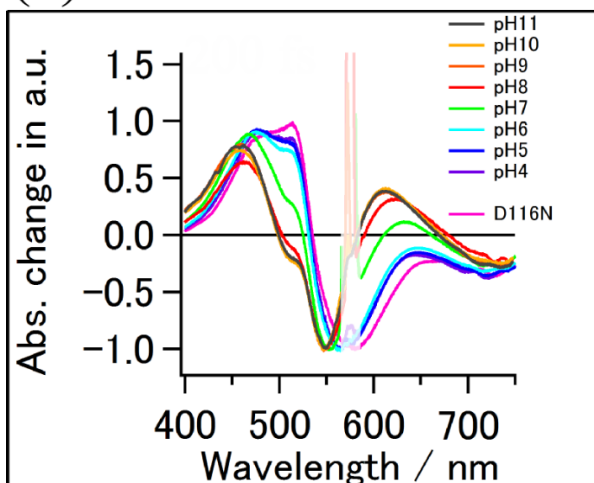
**Figure 5.4.** Temporal profiles of the femtosecond time-resolved absorption signals at pH 4 at (a) 460 nm, (b) 550 nm, (c) 650 nm, (d) 720 nm and (e) 740 nm with photoexcitation at 575 nm. (The pump energy is listed in Table 5.2.) The black solid curve drawn for each trace depicts the fits. The gray dashed lines are normalized kinetics at pH 8. Note that the horizontal scale is changed from the linear to the logarithmic scale after 3 ps. The time region shaded is distorted by unwanted instantaneous responses, such as coherent artifacts and Raman scattering of water.

The kinetics of ESA at 460 nm and those of SE at 720 and 740 nm exhibit a comparable decay that is characterized by common four time constants of  $\tau_1 = 180$  fs,  $\tau_2 = 1.3$  ps,  $\tau_3 = 7.0$  ps, and  $\tau_4 = 43$  ps. The  $\tau_1 = 180$  fs component was assigned to the deactivation of the  $S_1^r$  state at pH 8. The amplitude of this component at pH 4 is smaller than that at pH 8, indicating that the yields of the  $S_1^r$  state decreases at pH 4.

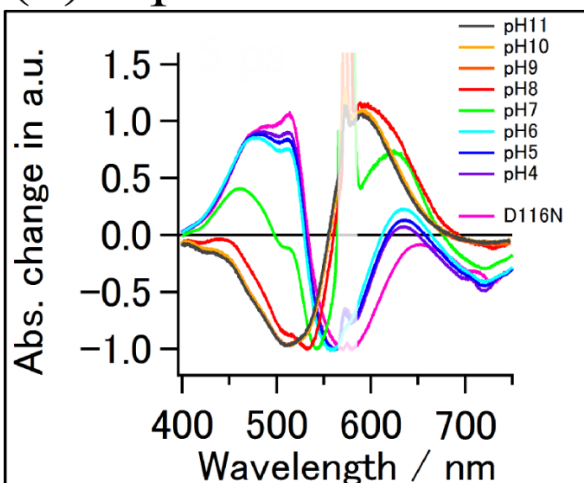
The normalized time-resolved spectra at selected delays and the kinetics at selected wavelengths at pHs ranging from 4 to 11 are shown in Figure 5.5 and 5.6. Those of D116N mutant are also shown. As clearly seen, at pH below 7, the time-resolved spectra and the kinetics approach those of D116N mutant, indicating that the negative charge of the side chain of the Asp 116 is neutralized. This suggests that the side chain of the Asp 116 is protonated at pH below 7. This observation is consistent with those reported in the pH titration experiment of KR2 using steady-state absorption spectrum.

The K-intermediate absorption band observed at long delay is pH-dependent, indicating that not only the shape of the absorption spectrum of the ground-state KR2 but also that of the K intermediate is pH dependent.

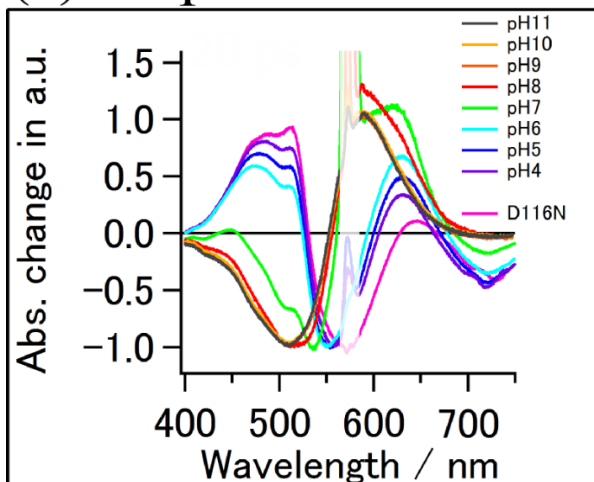
(a) 200 fs



(b) 5 ps



(c) 20 ps



(d) 200 ps

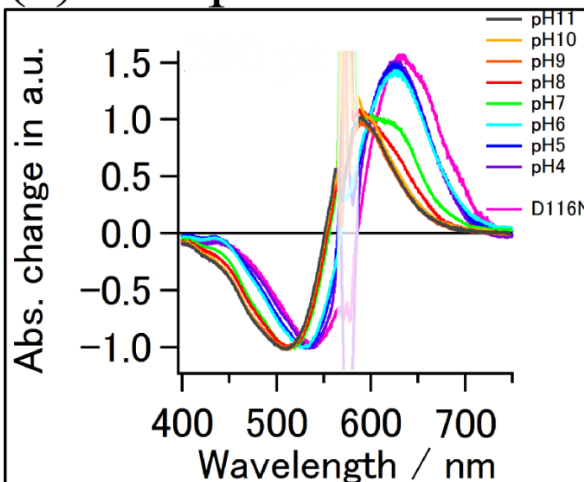


**Figure 5.5.** Femtosecond time-resolved absorption spectra at (a) 200 fs, (b) 5 ps, (c) 20 ps, and (d) 200 ps at pHs ranging from 4 to 11. Each spectrum is normalized at the peak of the bleaching (500-550 nm). The spectral region shaded is distorted by the scattering of the excitation beam.

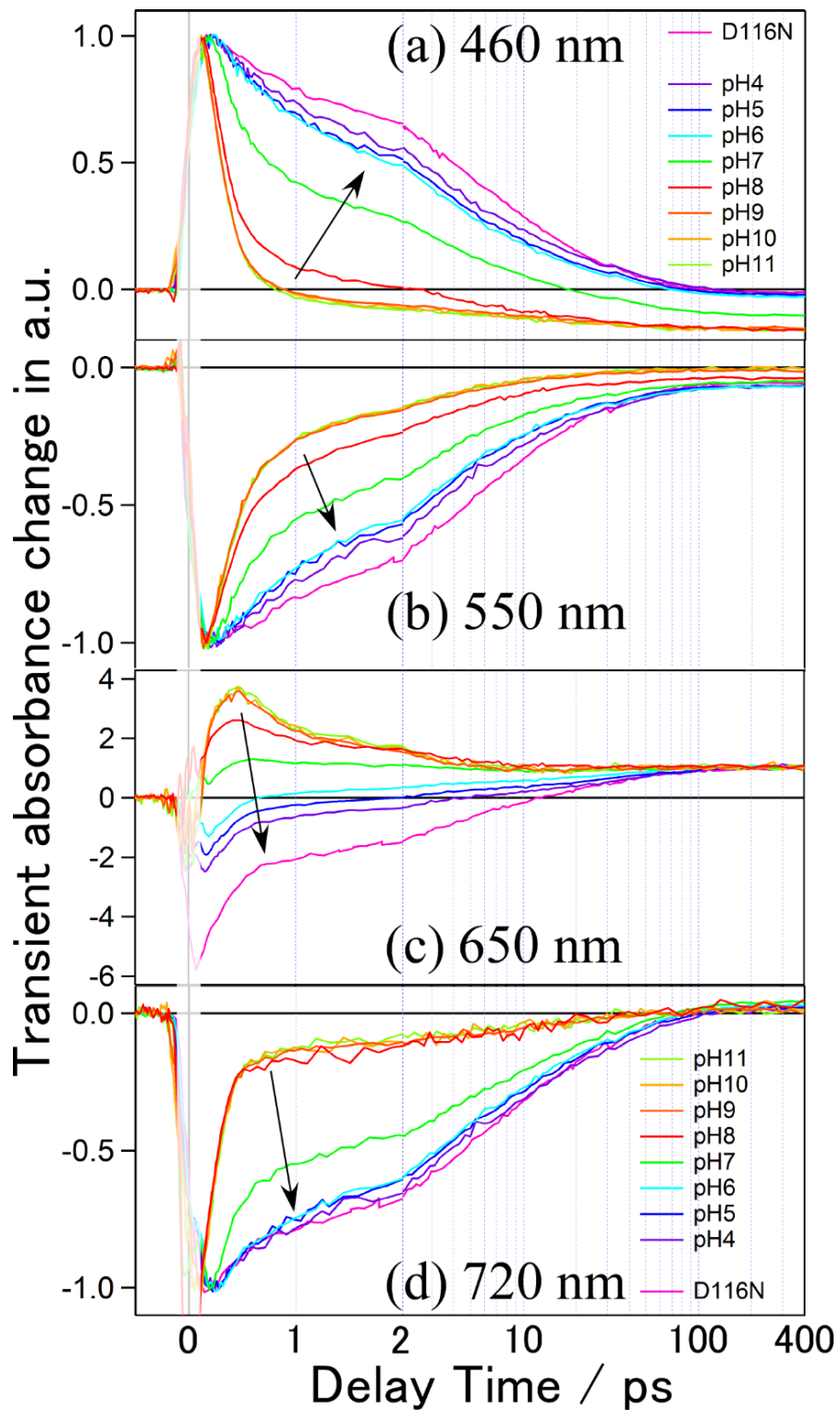


**Figure 5.6.** Temporal profiles at (a) 460, (b) 550, (c) 650, and (d) 720 nm at pHs ranging from 4 to 11. Each kinetics is normalized at the peak. The time region shaded is distorted by unwanted instantaneous responses, such as coherent artifacts and Raman scattering of water.

The pH dependence of the quantum yield of the K intermediate ( $\Phi_K$ ) is important to evaluate the reactivity at each pH. Here, we assume that (1) the maximum value of the PA band is proportional to the yield of the K intermediate, and that (2) the maximum value of the GSB is proportional to the number of the molecules excited. Based on these assumptions, the maximum value of the PA divided by the maximum value of the GSB is expected to be proportional to the  $\Phi_K$ . This value was calculated at each pH value to examine the pH dependence of the  $\Phi_K$ . This value is plotted against pH value in Figure 5.7. Obviously, this value drops at pH below 7, indicating the decrease in  $\Phi_K$ . The  $\Phi_K$  plot was compared with a curve representing the degree of the deprotonation of Asp 116, which is evaluated based on the pH dependence of the  $S_1 \leftarrow S_0$  absorption in the previous study<sup>8</sup> (Figure 5.7). The pH dependence of the  $\Phi_K$  coincides with this curve, indicating that the protonation of Asp 116 induces decrease in the  $\Phi_K$ . This suggests that the interaction between the PRSB and the Asp 116 is an important factor that determines whether the chromophore can undergo photoisomerization in the KR2 protein.

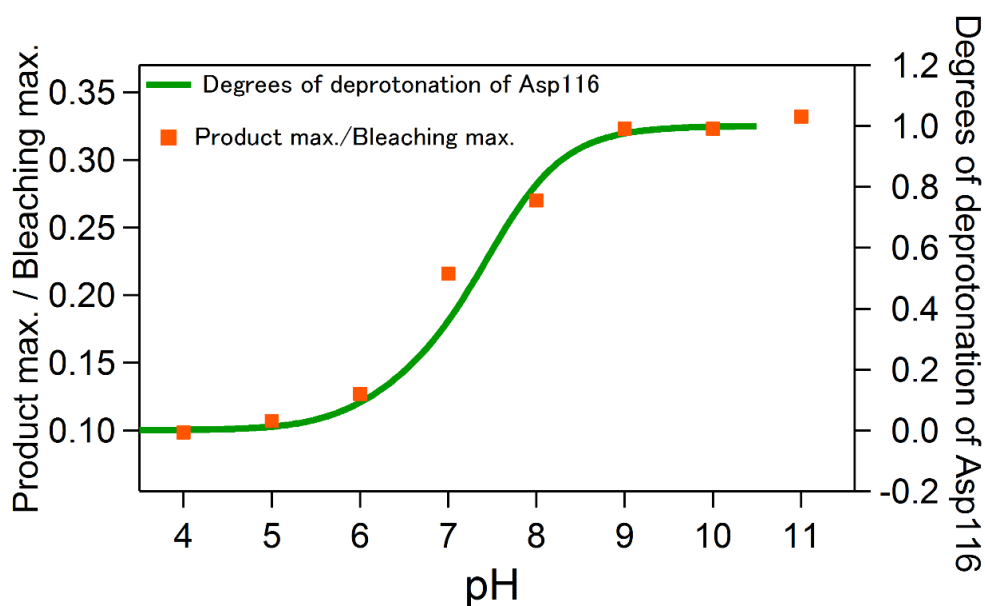


**Figure 5.7.** pH dependence of the quantum efficiency for the K formation. The value shown in orange plot is proportional to the quantum yield of the K intermediate. The green line shows the pH titration curve obtained from the pH dependence of the  $S_1 \leftarrow S_0$  absorption spectrum in the previous study.

The decrease in  $\Phi_K$  indicates that the protonation of Asp 116 decreases the yield of the  $S_1^f$  state (and increases the yield of the  $S_1^{nr}$  state). To examine the pH dependence of the yield of the  $S_1^f$  state, the amplitude of each component at 720 nm was extracted by the global fitting analysis at all pHs. The global fitting analysis showed that the five components are needed to reproduce the time-resolved absorption signal. The time constant and the amplitude of each component are summarized in Figure 5.8. Each time constant ( $\tau_0 - \tau_4$ ) is insensitive to pH value. As with KR2 at pH 4 and 8, the fastest component ( $\tau_0 \sim 30 - 60$  fs, shown in black plot and line in Figure 5.8) does not correspond to the deactivation process of the  $S_1$  state. Thus, this component is not referred in the following discussion. Only amplitude of the 180-fs component decreases at pH below 7 as with the  $\Phi_K$ , while the others increase. By comparing with the pH-dependent behavior of the  $\Phi_K$  (Figure 5.7), it is further confirmed that the 180-fs component corresponds to the deactivation of the  $S_1^f$  state that undergoes photoisomerization and generates the K intermediate. On the other hand, other components increases at pH below 7, and does not positively correlate with the  $\Phi_K$ . Therefore, the components other than the 180-fs component are assigned to the  $S_1^{nr}$  components.

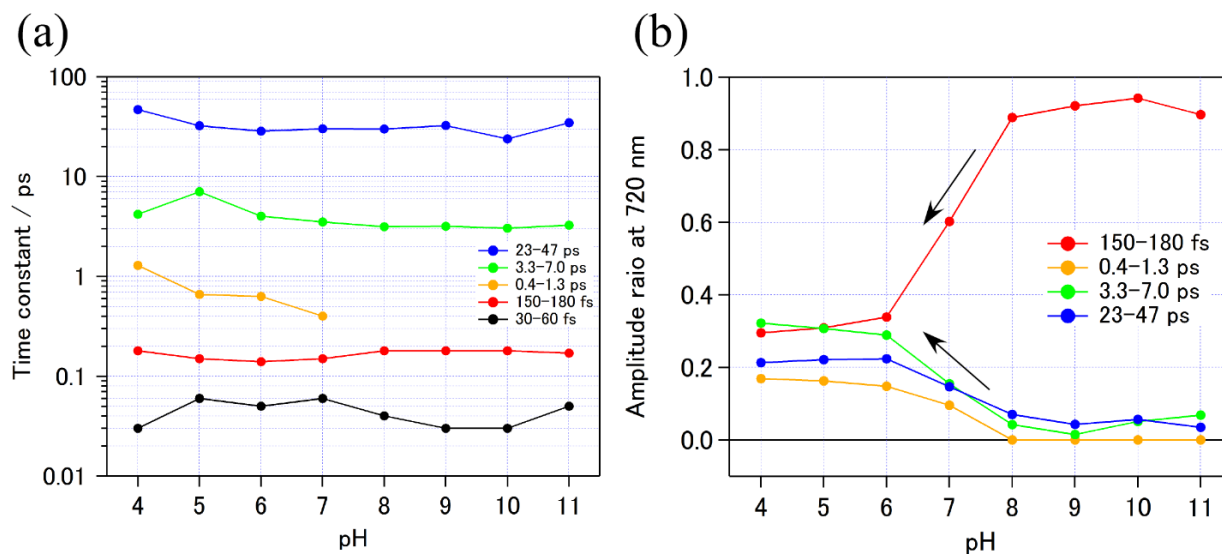


**Figure 5.8.** pH dependence of the (a) amplitude and (b) time constant of each component

The pH dependence of the amplitude of the  $S_1^f$  component (180-fs component) correlates well with the degree of the deprotonation of Asp 116 (Figure 5.9), suggesting that the  $S_1^f$  component is primarily yielded by the photoexcitation of the KR2 in the  $S_0$  state whose Asp 116 is deprotonated. On the other hand, the yields of the  $S_1^{nr}$  states increase upon the protonation of the Asp 116 (Figure 5.8), indicating that the  $S_1^{nr}$  states are mainly generated by the photoexcitation of the KR2 having the protonated Asp 116. In other words, KR2's having the deprotonated and protonated Asp 116 coexist and hold the pH-dependent equilibrium, and each species is photoexcited in parallel, yielding the  $S_1^f$  and  $S_1^{nr}$  states, respectively.

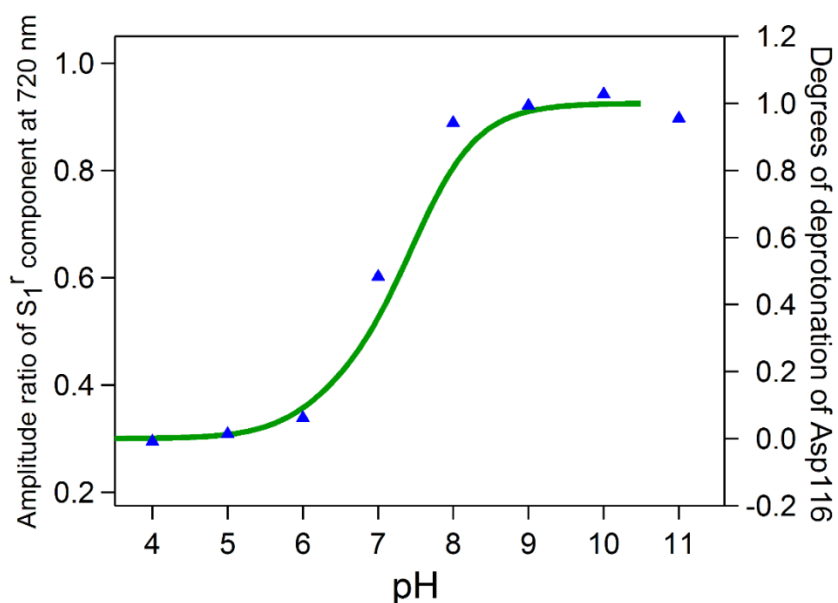


**Figure 5.9.** pH dependence of the amplitude of the  $S_1^f$  component (Blue triangle,  $\tau_0 \sim 150$  -180 fs). The green line shows the pH titration curve obtained from the pH dependence of the  $S_1 \leftarrow S_0$  absorption spectrum in the previous study.

At pH below 5, Asp 116 is expected to be completely protonated, implying that the Asp 116 does not work as a counterion of the PRSB. Under this condition, another aspartic acid residue (Asp 251) is one of the candidates for the counterion. However, the  $S_1^f$  does not vanish at pH below 5 (Figure 5.9), suggesting that the  $S_0$  state which generates the  $S_1^f$  state at acidic pH exists even at acidic pH. This implies that a fraction of KR2 has the deprotonated Asp 116

even at pH 5, giving rise to the generation of the  $S_1^r$  state. Also at pH above 10, it is expected that the  $S_1^{nr}$  states diminish. However, the obtained data manifest that the  $S_1^{nr}$  states are generated at this pH (Figure 5.8b). This seems to suggest that, even at pH above 10, a fraction of KR2 has the protonated Asp 116. Therefore, the existence of the small amount of the  $S_1^r$  and  $S_1^{nr}$  states at pH 5 and 10 is probably due to the existence of KR2's whose Asp 116 has different accessibility to the proton in the bulk. This hypothesis can be examined by steady-state vibrational spectroscopies or nuclear magnetic resonance spectroscopies.

## 5.4 Conclusions

The pH dependence of the ultrafast photoreaction of sodium-ion-pumping rhodopsin KR2 was investigated by femtosecond time-resolved absorption measurement. The obtained data clearly show that the quantum yield of the K intermediate decreases at pH below 7. Asp 116, the counterion of the PRSB at pH 8, is protonated at pH below 7. These facts suggest that the interaction between the Asp 116 and the PRSB is important for KR2 to undergo photoisomerization. The fitting analysis of the kinetics suggests that the yield of the reactive  $S_1$  state ( $S_1^r$ ) also decreases at pH below 7. The pH dependence of the yield of the  $S_1^r$  coincides with the degree of the deprotonation of Asp 116, suggesting that the  $S_1^r$  component is mainly yielded from the KR2 molecules possessing the deprotonated Asp 116. On the other hand, the  $S_1^{nr}$  components are primarily generated from those possessing the protonated Asp 116. Therefore, the sample is generally a mixture of the KR2 molecules having the protonated and deprotonated Asp 116, and each component is excited in parallel, and show the reactive and non-reactive dynamics, respectively.

## 5.5 References

- (1) Okumura, H.; Murakami, M.; Kouyama, T., Crystal Structures of Acid Blue and Alkaline Purple Forms of Bacteriorhodopsin. *J. Mol. Biol.* **2005**, *351*, 481-495.
- (2) Jonas, R.; Ebrey, T. G., Binding of a Single Divalent Cation Directly Correlates with the Blue-to-Purple Transition in Bacteriorhodopsin. *Proc. Natl. Acad. of Sci. USA* **1991**, *88*, 149-153.
- (3) Hiroyuki OHTANI, M. I., Hiroyasu ITOH, Yoshihiro TAKIGUCHI,; TSUCHIYA, T. U. a. Y., Picosecond Fluorescence Spectroscopy of Purple Membrane in Halobacterium Halobium with a Photon-Counting Streak Camera. *Chem. Phys. Lett.* **1990**, 493-498.
- (4) Mowery, P. C.; Lozier, R. H.; Chae, Q.; Tseng, Y.-W.; Taylor, M.; Stoeckenius, W., Effect of Acid Ph on the Absorption Spectra and Photoreactions of Bacteriorhodopsin. *Biochemistry* **1979**, *18*, 4100-4107.
- (5) Ohtani, H.; Kobayashi, T.; Iwai, J.; Ikegami, A., Picosecond and Nanosecond Spectroscopies of the Photochemical Cycles of Acidified Bacteriorhodopsin. *Biochemistry* **1986**, *25*, 3356-3363.
- (6) Kobayashi, T.; Terauchi, M.; Kouyama, T.; Yoshizawa, M.; Taiji, M., Femtosecond Spectroscopy of Acidified and Neutral Bacteriorhodopsin. *Proc. SPIE Laser Application in Life Sciences* **1991**, *1403*, 407-416.
- (7) Chang, C. H.; Jonas, R.; Govindjee, R.; Ebrey, T. G., Regeneration of Blue and Purple Membranes from Deionized Bleached Membranes of Halobacterium Halobium. *Photochem. and Photobiol.* **1988**, *47*, 261-265.
- (8) Inoue, K.; Ono, H.; Abe-Yoshizumi, R.; Yoshizawa, S.; Ito, H.; Kogure, K.; Kandori, H., A Light-Driven Sodium Ion Pump in Marine Bacteria. *Nat. Commun.* **2013**, *4*, 1678.
- (9) Tahara, S.; Takeuchi, S.; Abe-Yoshizumi, R.; Inoue, K.; Ohtani, H.; Kandori, H.; Tahara, T., Ultrafast Photoreaction Dynamics of a Light-Driven Sodium-Ion-Pumping Retinal Protein from *Krokinobacter Eikastus* Revealed by Femtosecond Time-Resolved Absorption Spectroscopy. *J. Phys. Chem. Lett.* **2015**, 4481-4486.
- (10) Sudo, Y.; Mizuno, M.; Wei, Z.; Takeuchi, S.; Tahara, T.; Mizutani, Y., The Early Steps in the Photocycle of a Photosensor Protein Sensory Rhodopsin I from *Salinibacter Ruber*. *The J. Phys. Chem. B* **2014**, *118*, 1510-1518.
- (11) Takumi Nakamura, S. T., Mikihiro Shibata, Makoto Demura, Hideki Kandori,; Tahara, a. T., Ultrafast Pump-Probe Study of the Primary Photoreaction Process in Pharaonis Halorhodopsin: Halide Ion Dependence and Isomerization Dynamics. *J. Phys. Chem. B* **2008**, 12795–12800.
- (12) Huber, R.; Köhler, T.; Lenz, M. O.; Bamberg, E.; Kalmbach, R.; Engelhard, M.; Wachtveitl, J., Ph-Dependent Photoisomerization of Retinal in Proteorhodopsin†. *Biochemistry* **2005**, *44*, 1800-1806.
- (13) Kandori, H.; Yoshihara, K.; Tomioka, H.; Sasabe, H., Primary Photochemical Events in Halorhodopsin Studied by Subpicosecond Time-Resolved Spectroscopy. *J. Phys. Chem.* **1992**, *96*, 6066-6071.



# Chapter 6: Structural Dynamics of Barrierless Photoisomerization Revealed by Femtosecond Stimulated Raman Spectroscopy

## 6.1 Introduction

In thermal isomerization reaction, reactants and products are separated by an energy barrier. Therefore, only reactants which gain the sufficient thermal energy can surmount the energy barrier, and after that, form isomerized product on the time scale of the nuclear motion. For this reason, molecules are not accumulated in “isomerizing” states, which correspond to the states on the barrier, making the spectroscopic observation of the “isomerizing” states difficult. On the other hand, the ultrafast photoisomerizations of some molecules such as cyanine dyes, *cis*-stilbene and visual rhodopsin<sup>1-4</sup> allegedly take place in the absence of the finite energy barrier (barrierless photoisomerization). In barrierless photoisomerization, the reactant molecules synchronously isomerize on the time scale of the nuclear motion. Therefore, substantial amount of molecules can transiently populate in the “isomerizing” states, enabling us to observe them. Based on this observation, it can be verified what kind of structural events occur in the process of the isomerization.

1,1'-Diethyl-4,4'-cyanine (1144C) is one of the cyanine dyes<sup>3, 5-21</sup> which undergoes barrierless photoisomerization about a center CC double bond which is linking two quinoline rings in the  $S_1$  state (Figure 6.1). On the basis of the previous experimental and theoretical studies, the photoisomerization process of 1144C in the  $S_1$  state is described as following. (i) After pretwisted<sup>20</sup>  $S_1$  population is created in the Franck-Condon region, it moves toward the relaxed  $S_1$  state accompanied by the twisting<sup>6-8, 21</sup> in a barrierless fashion. (ii) Subsequently, the population stays in the relaxed  $S_1$  state, where the  $S_1 \rightarrow S_0$  internal conversion efficiently proceeds, and finally (iii) the  $S_1 \rightarrow S_0$  internal conversion takes place, yielding the *cis* form of 1144C.

Recently, using pump-dump-probe scheme<sup>22, 23</sup>, the stimulated emission kinetics of 1144C were observed<sup>18</sup>. The stimulated emission kinetics exhibited a rise component whose

time constant becomes longer as the dump wavelength gets longer, suggesting that the red shift of the stimulated emission spectrum takes place. This indicates that the  $S_1$ - $S_0$  energy difference gets smaller as the twisting proceeds in process (i). In addition, this study also demonstrated that the decay rate of the stimulated emission is insensitive to the dump wavelength, indicating that the distribution of the population spreads on the  $S_1$  potential. The spreading of the distribution is primarily the consequence of the dynamics involving various structural changes and fluctuations. However, the electronic spectroscopy such as pump-dump-probe spectroscopy is insensitive to the structural dynamics. Therefore, the electronic spectroscopy does not show how the distribution moves and spreads on the  $S_1$  potential.

Femtosecond stimulated Raman spectroscopy (FSRS)<sup>24-27</sup> is a powerful tool to obtain the structural information of the transient species. In this method, a narrowband picosecond Raman pump pulse, which is resonant with the electronic transition of the transient species, and a supercontinuum probe pulse simultaneously irradiate the transient species, enabling us to measure the resonantly enhanced stimulated Raman spectra of these species. Therefore, if the Raman pump wavelength is chosen so as to be resonant with the  $S_1 \rightarrow S_0$  stimulated emission at the middle point of the reaction pathway (i.e. “isomerizing” state) on the barrierless  $S_1$  potential of 1144C, it is expected that the FSRS spectrum of the “isomerizing” 1144C in the  $S_1$  state can be obtained. Moreover, scanning the Raman pump wavelength yields the FSRS spectra of the transient species at all the regions of the reaction coordinate, and the “movie” of the photoisomerization process may be constructed.

In this study, using visible-to-near-IR tunable femtosecond stimulated Raman setup, FSRS measurements were carried out at six Raman pump wavelengths ranging from 740 to 1100 nm to capture the structural dynamics during the barrierless photoisomerization of a cyanine dye in the  $S_1$  state. Based on the obtained data, the structural dynamics of the cyanine molecules during the barrierless photoisomerization is discussed.

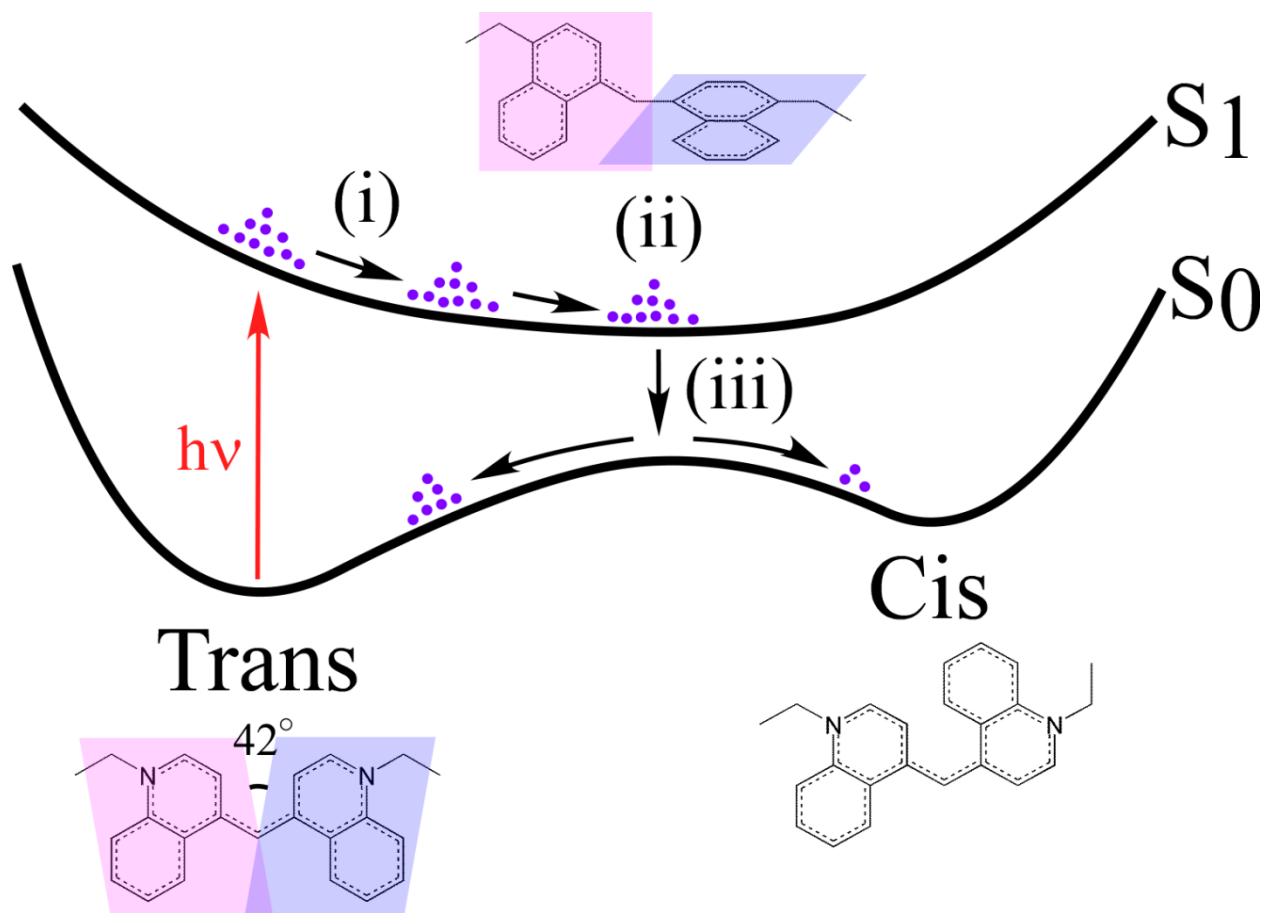


**Figure 6.1.** Schematic illustration of the barrierless photoisomerization process of 1144C.

## 6.2 Experimental methods

### Sample preparation

1,1'-Diethyl-4,4'-cyanine (1144C) iodide (Sigma Aldrich) was used as receive. The methanol (Spectrum grade, Nacalai Tesque) solution of 1144C iodide with an absorbance of 0.8 OD / 0.2 mm at 610 nm was prepared and used in the following experiments.

### Visible and near-infrared femtosecond absorption spectroscopy

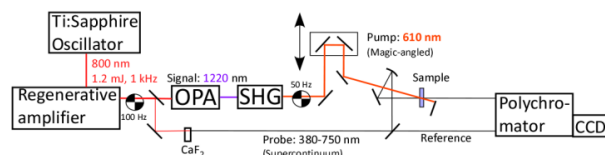
The experimental apparatus of visible and near-infrared femtosecond absorption spectroscopy are depicted in Figure 6.2a and b. An optical parametric amplifier (TOPAS-C, Light Conversion) was driven by the output of a Ti:sapphire amplifier system (800 nm, 1.2 mJ, 80 fs, 1 kHz, Legend Elite, Coherent), and its idler output (2320 nm) was attenuated and focused into a c-cut 2-mm-thick Sapphire plate to generate a single-filament near-infrared supercontinuum probe pulse. The probe pulse is divided into two, and they are used as probe and reference pulses. The signal output (1220 nm) was frequency-doubled to generate an actinic pump pulse at 610 nm. The polarization of the actinic pump pulse was set to the magic angle ( $54.7^\circ$ ) with respect to the horizontally polarized probe pulse. The probe and actinic pump (200 nJ/pulse) pulses were focused into a sample solution, which is continuously circulated in a flow cell with an optical length of 0.2 mm. The circulation speed was adjusted to allow the sample solution in the excited volume to be replaced with respect to each laser shot. The probe pulse after passing through the sample and the reference pulse were analyzed by a polychromator (300 grooves/mm, SP2150, Acton) equipped with a 512-channel InGaAs array (G9212-512S, Hamamatsu). The group delay dispersion of the near-infrared supercontinuum probe pulse was evaluated by the coherent artifact of the methanol, and it was used to calibrate the time origin at each wavelength. The time resolution of this measurement was evaluated to be 100 fs from the temporal profile of the coherent artifact.

## Visible and near-infrared femtosecond stimulated Raman spectroscopy

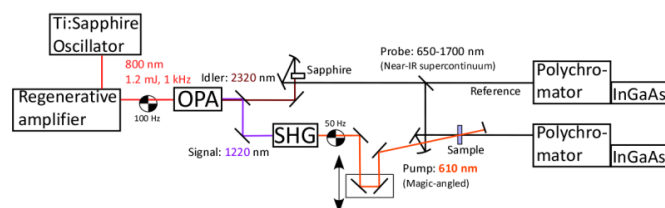
The experimental apparatus of visible and near-infrared femtosecond absorption spectroscopy are depicted in Figure 6.2c and d. The output of a Ti:sapphire amplifier system (800 nm, 8.0 mJ, 100 fs, 1 kHz, Legend Elite Duo, Coherent) was divided into three portions. The 4.0 mJ portion was used to drive an optical parametric amplifier, and its signal output (1220 nm) was frequency-doubled to generate an actinic pump pulse at 610 nm. The 3.0 mJ portion was converted to a 400-nm picosecond pulse by sum frequency generation of positively and negatively chirped 800-nm pulses (SHBC, Light Conversion). The 400-nm picosecond pulse was used to drive a picosecond optical parametric amplifier (TOPAS-400-WL, Light Conversion), and its signal output was used as a Raman pump pulse at 740 and 780 nm (13,514 and 12,821  $\text{cm}^{-1}$ , respectively). The leftover 800-nm output of the amplifier was focused into a 3-mm-thick calcium fluoride ( $\text{CaF}_2$ ) to generate a visible supercontinuum pulse. The visible supercontinuum pulse was introduced to a prism compressor so that the group delay dispersion is compensated, yielding a probe pulse with a group delay difference less than 20 fs over the probed wavelength region. The leftover 800-nm component contaminated in the supercontinuum was removed after the supercontinuum is dispersed by the second prism of the compressor. The polarization of the actinic pump pulse was set to the magic angle ( $54.7^\circ$ ) with respect to the horizontally polarized probe pulse. The actinic pump (600 nJ/pulse), Raman pump (0.5  $\mu\text{J}$ /pulse) and probe pulses are focused into a sample solution, which is continuously circulated in a flow cell with an optical length of 0.2 mm. The probe pulse after passing through the sample was analyzed by a polychromator (1200 g/mm, iHR320, Horiba) equipped with an electronically cooled 1340-channel CCD camera (PIXIS-400F, Princeton Instruments). The probe spectrum in the anti-Stokes region was detected. The time resolution of this measurement was evaluated to be 100 fs from the temporal profile of the optical Kerr effect signal. The frequency resolution was evaluated to be 20  $\text{cm}^{-1}$  from the FWHM of the 1035- $\text{cm}^{-1}$  stimulated Raman band of the methanol. The experimental setup of near-IR FSRS is the same as that of the visible one with a few exceptions. The near-IR supercontinuum probe pulse was generated by focusing the signal output (1220 nm) of the optical parametric amplifier into a c-cut 2-mm-thick sapphire plate. The residual of the signal output contaminated in the supercontinuum was eliminated by a near-infrared bandpass filter (RT-830, HOYA). The idler

output of the picosecond optical parametric amplifier was used as the Raman pump pulse at 836 (11,962  $\text{cm}^{-1}$ , 0.5  $\mu\text{J}$ ), 902 (11,086  $\text{cm}^{-1}$ , 0.6  $\mu\text{J}$ ), 983 (10,173  $\text{cm}^{-1}$ , 0.6  $\mu\text{J}$ ) and 1100 nm (9,091  $\text{cm}^{-1}$ , 2  $\mu\text{J}$ ). The group delay difference was evaluated to be less than 20 fs over the probed wavelength region by the OKE measurement. The frequency resolution was evaluated to be 20  $\text{cm}^{-1}$ .

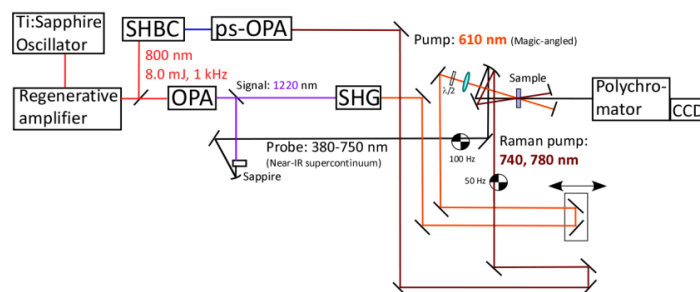
(a) Visible femtosecond absorption setup



(b) Near-IR femtosecond absorption setup



(c) Visible femtosecond stimulated Raman setup



(d) Near-IR femtosecond stimulated Raman setup

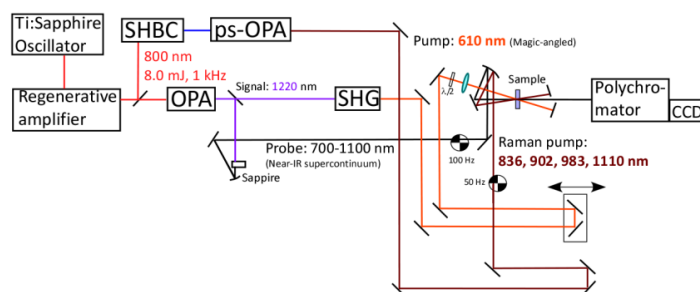


**Figure 6.2.** Schematic illustration of visible and near-infrared (a-b) transient absorption and (c-d) femtosecond stimulated Raman setup.

## Data processing

Not only the stimulated Raman signal due to the photoexcited 1144C, but also those of the methanol and unexcited 1144C are superimposed on the raw FSRS spectra (Figure 6.3a). Therefore, the subtraction of these backgrounds is requisite to obtain the net FSRS spectra. The FSRS measurements of the methanol solution of 1144C and methanol were carried out without actinic pump pulse, yielding the stimulated Raman spectrum of the methanol solution of the ground-state 1144C and methanol (Figure 6.3a), respectively. Then, the stimulated Raman spectrum of the ground-state 1144C was obtained by subtracting the stimulated Raman spectrum of the methanol from the stimulated Raman spectrum of the methanol solution of the ground-state 1144C. The stimulated Raman spectrum of the methanol solution of the ground-state 1144C was subtracted from the raw FSRS spectra at negative delays, and the net FSRS spectra at these delays were obtained. Considering the depletion of the  $S_0$ -state population caused by the photoexcitation, the stimulated Raman spectrum of the ground-state 1144C multiplied by a factor of 0.9 and that of the methanol were subtracted from the raw FSRS spectra at positive delays, yielding the baseline-unsubtracted spectra at these delays (Figure 6.3b). After these procedures, the baseline, which comes from the scattering of the Raman pump and deexcitation of the  $S_1$ -state population owing to the irradiation of the Raman pump, was evaluated by the polynomial fitting of the spectra (Figure 6.3b), and it was subtracted from the baseline-unsubtracted spectra.

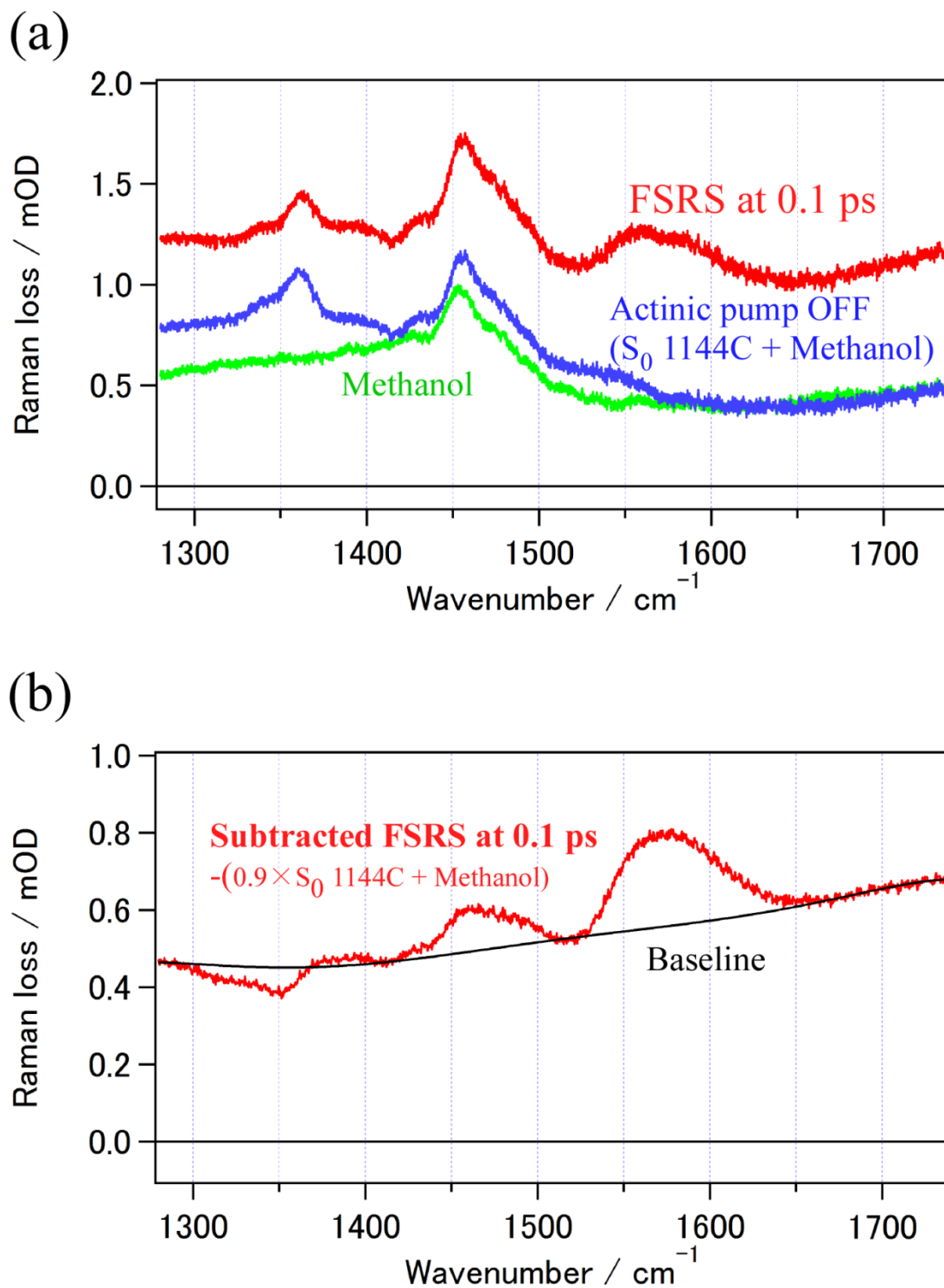


**Figure 6.3.** (a) The raw FSRS spectra of the methanol solution of 1144C at 0.1ps (red), without actinic pump pulse (blue) and the methanol without actinic pump pulse measured at 1100 nm (green). (b) The baseline-unsbtracted spectrum obtained by subtracting the methanol spectrum and the stimulated Raman spectrum of the ground-state 1144C multiplied by a factor of 0.9.

## Theoretical calculations

All the calculations were carried out using Gaussian09<sup>28</sup>. The molecular structure of 1144C was first constructed using MolStudioR4. To obtain the molecular structure in the  $S_0$  state, the optimization was carried out at B3LYP/6-311+G(d,p) level with the PCM correction (Methanol). Using the optimized structure, the off-resonant  $S_0$  Raman spectrum of 1144C was calculated at B3LYP/6-311+G(d,p) level with the PCM correction (Methanol).

The molecular structure of the relaxed  $S_1$  state was constructed by twisting about one of the center C=C bonds of the  $S_0$  structure by 48 degrees, and the structure was optimized at TD-B3LYP/6-31+G(d) level, yielding the structure in the relaxed  $S_1$  state. The frequencies of vibrations in the relaxed  $S_1$  state were calculated at TD-B3LYP/6-31+G(d) level. The  $S_1 \rightarrow S_0$  resonance Raman intensity of each mode is proportional to the square of the gradient of the  $S_0$  potential along the coordinate of each mode at the nuclear coordinate of the relaxed  $S_1$  state<sup>29-31</sup>. To calculate the gradient, first, the molecular structures which is positively and negatively displaced from the structure in the relaxed  $S_1$  state along the coordinate of vibrational mode (by normal coordinates multiplied by factors of  $\alpha = \pm 0.01$ ). The SCF energies for these structures were calculated at B3LYP/6-31+G(d) level. The difference between these energies was divided by the displacement between these structures, and the gradient at the nuclear coordinate of the relaxed  $S_1$  state is obtained. The same applies for each vibration.

## 6.3 Results & discussion

### Femtosecond time-resolved visible and near-infrared absorption measurement

Transient absorption spectra in UV-to-NIR region were measured. In Figure 6.4a, transient absorption spectra are represented in a contour plot. Transient absorption spectra at selected delays are shown in Figure 6.4b. After photoexcitation, a broad  $S_1 \rightarrow S_0$  stimulated emission band is observed in the VIS-to-NIR region ( $> 650$  nm). The decay of the stimulated emission and the recovery of the  $S_0$  bleaching take place concomitantly within 5 ps, indicating that the population created in the  $S_1$  state relaxes to the  $S_0$  state by this delay. In addition to these spectral features, a relatively narrow  $S_n \leftarrow S_1$  absorption band is observed around 1000 nm. This absorption band decays much faster than the stimulated emission band, suggesting that it is attributable to the  $S_n \leftarrow S_1$  absorption of the population in the vicinity of the Franck-Condon state.

To extract the dynamics in the  $S_1$  state, the temporal profiles of the transient absorption signals at selected wavelengths were analyzed, which are shown with colored lines in Figure 6.4c. The fitting analysis of the kinetics at each wavelength was performed with a bi-exponential function convoluted with a Gaussian instrumental response function having a 100-fs FWHM, reproducing nicely at each wavelength as shown in a black line in Figure 6.4c. Based on the fitting results, these profiles show a sub-picosecond rise followed by a picosecond decay. At wavelengths shorter than 900 nm, the time constant for the decay of the stimulated emission increases from 0.6 ps to 1.3 ps as the probe wavelength becomes longer. It suggests that the  $S_1$  population migrates from the probed potential region into the other potential region within the  $S_1$  lifetime. On the other hand, the stimulated emission kinetics at wavelengths longer than 900 nm decay with a common time constant of 1.3 ps, which coincide with that of the  $S_0$  recovery, indicating that the relaxed  $S_1$  state is observed in this wavelength region. Moreover, the time constant for the sub-picosecond rise increases with the increase in the probe wavelength, indicating the gradual red shift of the stimulated emission band. This indicates that the  $S_1$ - $S_0$  energy difference gradually decreases as the structure of 1144C evolves on the  $S_1$  potential, strongly supporting that the structural evolution of 1144C in the  $S_1$  state is taken place in a barrierless fashion.

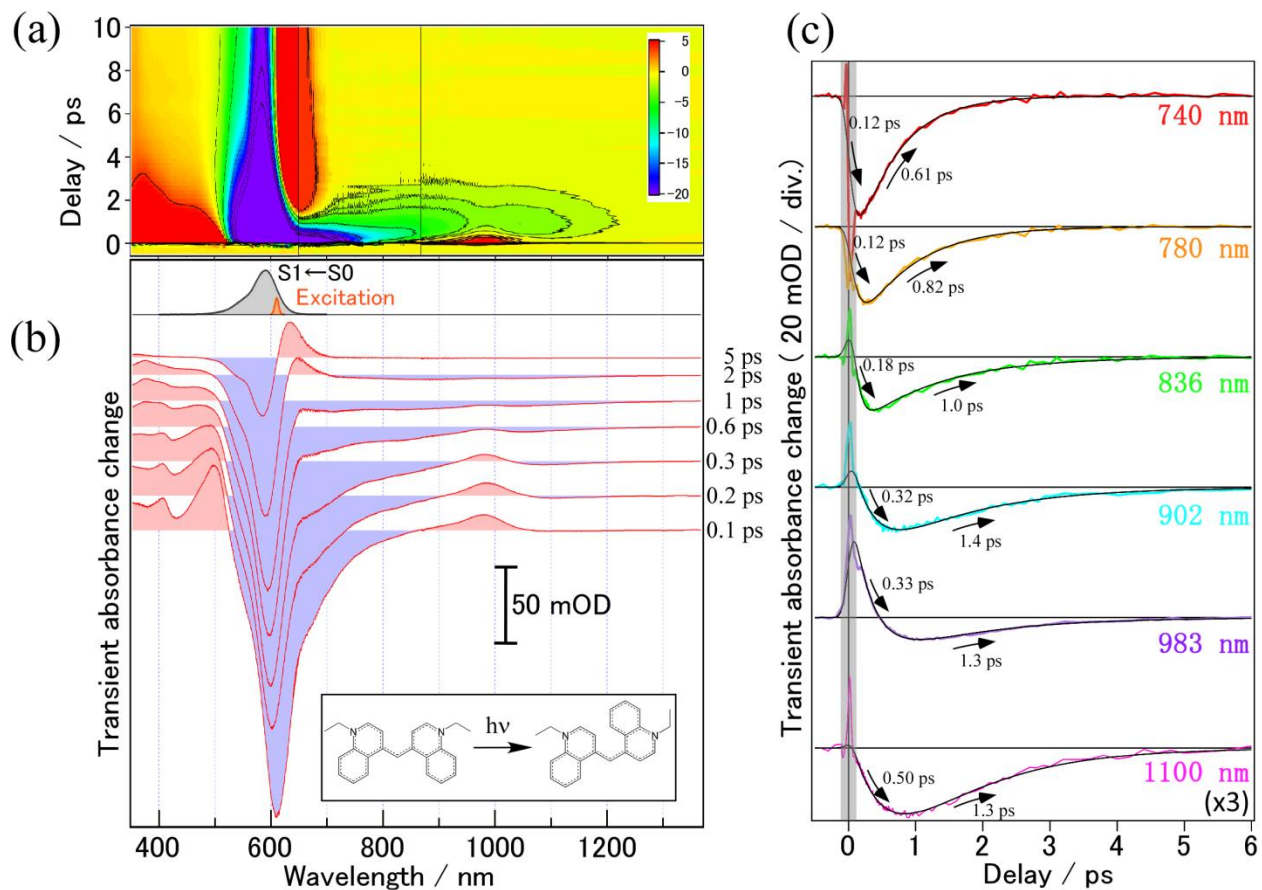


**Figure 6.4.** Femtosecond transient absorption. (a) The spectra represented as a contour plotted against wavelength and delay. The vertical lines represent the seam between two different spectra. (b) The spectra at selected delays. (c) The kinetics at selected wavelengths. The energy and FWHM of the actinic pump pulse were 200 nJ / pulse and  $\sim 100$  fs, respectively.

## Femtosecond stimulated Raman measurement using 740-nm Raman pump

FSRS measurement was carried out using 740-nm Raman pump. Since the Raman pump is resonant with the  $S_1 \rightarrow S_0$  stimulated emission, the Raman loss signals are expected to be observed in anti-Stokes region<sup>32</sup>. The obtained anti-stokes spectrum exhibited Raman loss bands at 1010, 1460, 1555 and 1640  $\text{cm}^{-1}$  and a dispersive band at  $\sim 1350 \text{ cm}^{-1}$  as shown in Figure 6.5a. The appearance of a mode-specific dispersive band at  $\sim 1350 \text{ cm}^{-1}$  might be due to the contribution from a resonantly enhanced inverse-Raman-like nonlinear process from the vibrationally excited state (See Appendix). The FSRS signal almost completely decays within 2 ps without changing its shape. Not only the frequency but also the intensity pattern of the FSRS spectra is similar to that of the  $S_1 \leftarrow S_0$  resonance Raman spectrum (Figure 6.5a). This indicates that the obtained FSRS spectra reflect the structural dynamics in the vicinity of the Franck-Condon state.

To make vibrational assignments of these bands, the  $S_0$  Raman spectrum was calculated at B3LYP/6-311+G(d,p) level with the PCM correction (Methanol) using Gaussian09<sup>28</sup>. The calculated spectrum nicely reproduced both off-resonant  $S_0$  stimulated Raman spectrum measured with the 740-nm Raman pump and  $S_1 \leftarrow S_0$  resonance Raman spectrum in the 1000-1700  $\text{cm}^{-1}$  region as shown in Supporting figure 6.1. Based on the calculated result, the bands observed in  $\sim 1100\text{-}1200 \text{ cm}^{-1}$ ,  $\sim 1200\text{-}1500 \text{ cm}^{-1}$  and  $1500\text{-}1700 \text{ cm}^{-1}$  regions were assigned to hydrogen-in-plane vibrations, skeletal stretching involving the stretching of the center CC double bond and quinoline ring stretching vibrations, respectively. Here, the Raman bands in  $1500\text{-}1700 \text{ cm}^{-1}$  region (Figure 6.5b) are discussed to make vibrational assignments of the quinoline ring stretching bands. The Raman bands in this region are also reproduced by the calculation (Figure 6.5b, black bars and gray curve are calculated spectra with and without taking the  $20\text{-cm}^{-1}$  bandwidth into consideration.). In this wavenumber region, an intense band at 1543  $\text{cm}^{-1}$  and a band at 1631  $\text{cm}^{-1}$  were observed in the off-resonant  $S_0$  stimulated Raman spectrum measured with the 740-nm Raman pump and the  $S_1 \leftarrow S_0$  resonance Raman spectrum. By comparing them with the calculated result, the 1543- $\text{cm}^{-1}$  band is assignable to a quinoline ring stretching (1540  $\text{cm}^{-1}$  in calculation), whereas 1631- $\text{cm}^{-1}$  band is attributed to another quinoline ring stretching (1637  $\text{cm}^{-1}$  in calculation) as shown in Figure 6.5c. These bands are called Q1

and Q2 bands, hereafter. (The experimentally obtained and calculated frequencies of these two vibrations are summarized in Table 6.1).

Based on the assignments of the vibrational bands observed in the  $S_1 \leftarrow S_0$  resonance Raman spectrum, the 1555- $\text{cm}^{-1}$  and 1640- $\text{cm}^{-1}$  bands in the FSRS spectrum are assigned to the Q1 and Q2 vibrations in the  $S_1$  state shown in Figure 6.5c. The frequencies of the Q1 and Q2 bands in the  $S_1$  state are also summarized in Table 6.1.

**Table 6.1.** The experimental and calculated frequencies of the Q1 band Q2 bands.

Wavenumber / $\text{cm}^{-1}$	Q1 band	Q2 band
$S_1 \leftarrow S_0$ resonance Raman and $S_0$ non-resonant stimulated Raman	1543 $\text{cm}^{-1}$	1631 $\text{cm}^{-1}$
Calculated $S_0$ Raman	1540 $\text{cm}^{-1}$	1637 $\text{cm}^{-1}$
$S_1$ FSRS at $\lambda_R=740$ nm at 0.1 ps	1555 $\text{cm}^{-1}$	1640 $\text{cm}^{-1}$
$S_1$ FSRS at $\lambda_R=1100$ nm at 0.1 ps	1575 $\text{cm}^{-1}$	N.D.
$S_1$ FSRS at $\lambda_R=1100$ nm at 2 ps	1600 $\text{cm}^{-1}$	N.D.

The  $S_1 \leftarrow S_0$  resonance Raman was measured with the 514-nm cw pump.  $S_0$  non-resonant stimulated Raman was measured with the 740-nm Raman pump. The calculated  $S_0$  Raman was obtained at B3LYP/6-311+G(d,p) level with the PCM correction (Methanol). N.D.: not detected

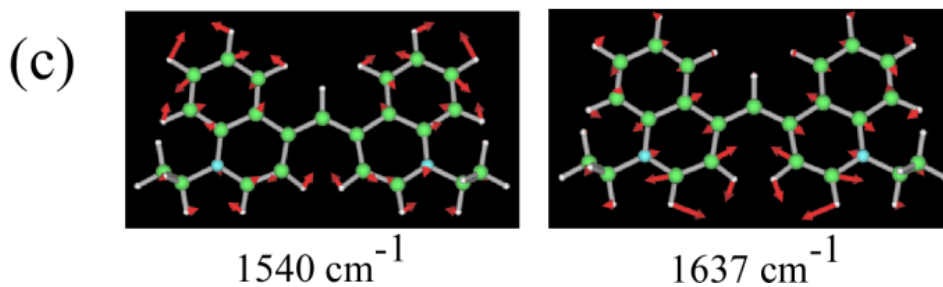
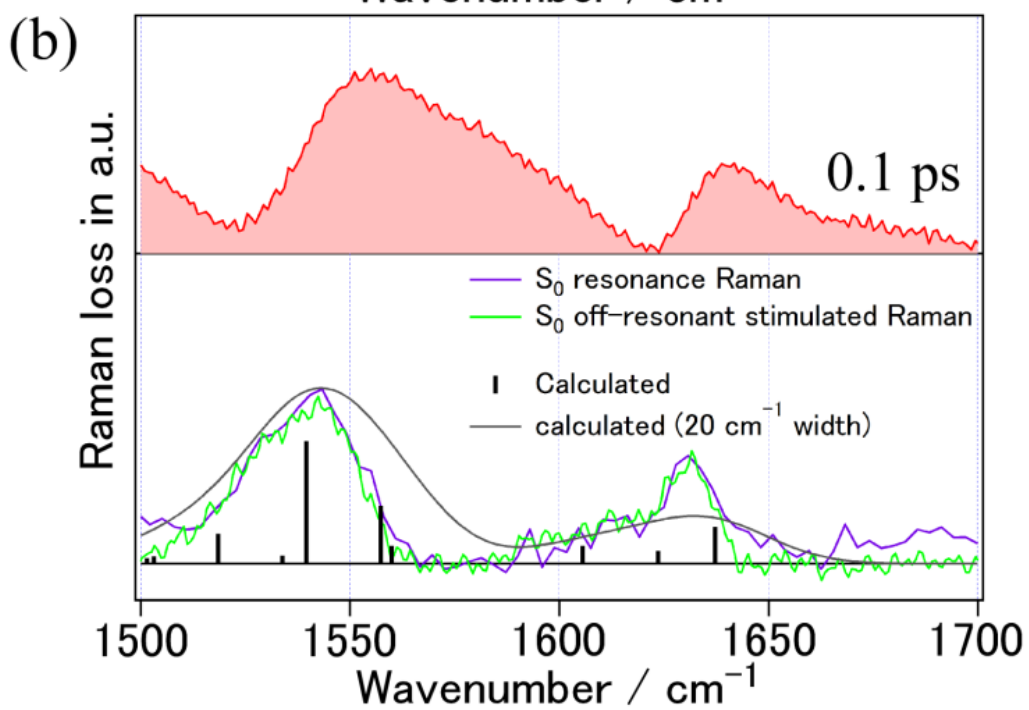
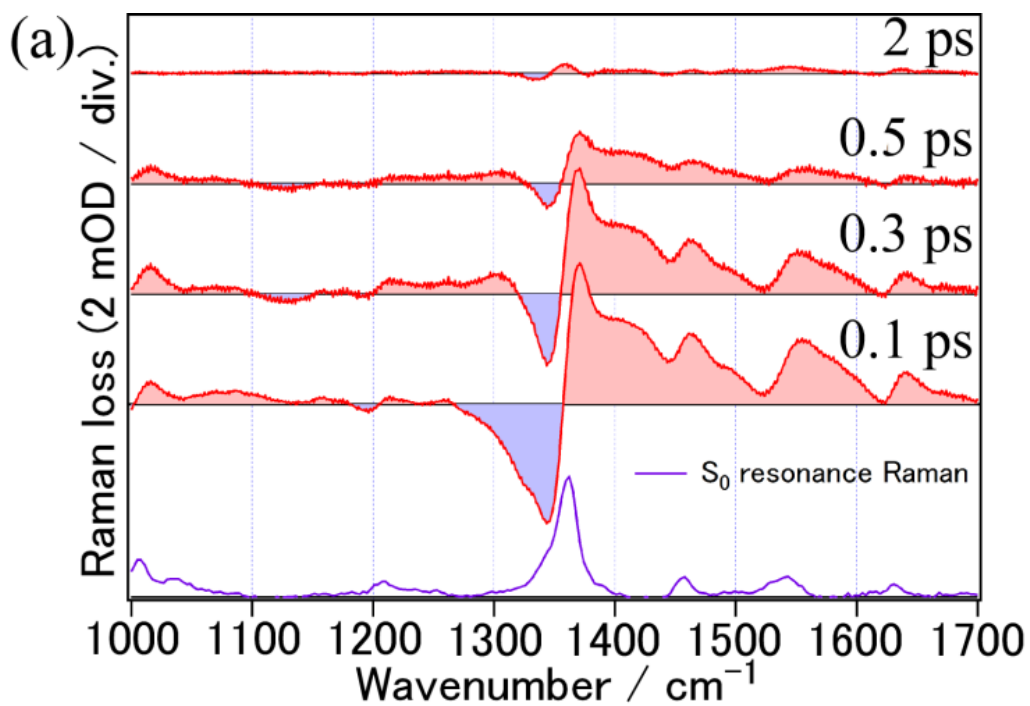


**Figure 6.5.** (a) Femtosecond stimulated Raman spectra at selected delays obtained with 740-nm Raman pump and steady-state resonance Raman spectrum obtained with 514-nm cw pump in 1000-1700  $\text{cm}^{-1}$  region are shown in red lines and purple line, respectively. (b) The comparison between the spectrum at 0.1 ps and the steady-state  $S_1 \leftarrow S_0$  resonance Raman (purple), the steady-state non-resonant stimulated Raman obtained with the 740-nm Raman pump (green), and the steady-state non-resonant Raman spectrum calculated at B3LYP/6-311+G(d,p) level with the PCM correction (black bars) in 1500-1700  $\text{cm}^{-1}$  region. The scaling factor for the calculated Raman spectrum was 0.99. The calculated steady-state non-resonant Raman spectrum that takes the bandwidth (20  $\text{cm}^{-1}$ ) into consideration is also shown in gray line. (c) The normal modes corresponding to the calculated 1540 and 1637  $\text{cm}^{-1}$  bands. The energy and duration of the actinic pump were 200 nJ / pulse and  $\sim 100$  fs, respectively. The energy and duration of the Raman pump were 0.5  $\mu\text{J}$ /pulse and  $\sim 1.8$  ps, respectively.

## Femtosecond stimulated Raman measurement using 1100-nm Raman pump

FSRS spectra at selected delays measured by means of 1100-nm Raman pump are shown in Figure 6.6a. Raman loss bands at 1460 and  $\sim 1600\text{ cm}^{-1}$  and a dispersive band at  $\sim 1350\text{ cm}^{-1}$  are observed. Surprisingly, the spectral feature in 1500-1700  $\text{cm}^{-1}$  region at 0.1 ps is significantly different from that obtained with the 740-nm Raman pump. A Raman loss band, which is considered to correspond to the 1555- $\text{cm}^{-1}$  quinoline ring stretching (Q1) band observed at 740 nm, showed up at 1575  $\text{cm}^{-1}$ . In addition, the 1640- $\text{cm}^{-1}$  (Q2) band was absent. These differences indicate that the structure observed at 1100 nm is different from what is observed at 740 nm. In addition, differently from the 740-nm spectra, the Raman signals persist up to 5 ps. This temporal behavior reflects the lifetime of the relaxed  $S_1$  state.

It is notable that the peak frequency of the Q1 band obviously increases from 1575  $\text{cm}^{-1}$  (at 0.1 ps) to 1600  $\text{cm}^{-1}$  (at 2 ps) on sub-picosecond timescale. This peak shift was clearly recognized even before the subtraction of the baseline (Supporting figure 6.2). The frequencies of the Q1 and Q2 at 0.1 ps and 2 ps bands are summarized in Table 6.1.

To elucidate the origin of the upshift of the Q1 band, the resonance Raman spectrum of the relaxed  $S_1$  state was calculated. The frequencies of vibrations were calculated at TD-B3LYP/6-31+G(d) level<sup>28</sup>. The resonance Raman intensity of each mode is calculated by calculating the gradient of the  $S_0$  potential along each vibrational mode at the nuclear coordinate of the relaxed  $S_1$  state<sup>29-31</sup>. As compared with the calculated result, it is considered that the Q1 band is composed of several bands assignable to the quinoline ring stretching modes (Figure 6.6b). In fact, the calculated spectrum, which takes the 40- $\text{cm}^{-1}$  bandwidth of each band into consideration, reproduced the shape of the Q1 band at 2 ps nicely (Figure 6.6b).

The vibration corresponding to the 1550- $\text{cm}^{-1}$  (calculated, Figure 6.6c) band in the calculated relaxed  $S_1$  state is very similar to the 1540- $\text{cm}^{-1}$  (calculated, Figure 6.5c) vibration in the  $S_0$  state. This vibration is observed dominantly in the 740-nm FSRS spectra, whereas the Raman intensity of this vibration is weak relative to that of the  $\sim 1600\text{-cm}^{-1}$  bands (calculated, Figure 6.5c) in the calculated relaxed  $S_1$  spectrum. Therefore, it is concluded that the relative Raman intensity of this band gradually decreases with respect to those of the  $\sim 1600\text{-cm}^{-1}$  bands concomitantly with the twisting motion, giving rise to the apparent upshift of the Q1 band. The

relative intensity change of the Raman bands indicates the relative  $S_1$ - $S_0$  displacement change of each mode. This suggests that the structure of the quinoline ring gradually changes with the twisting. In other words, the position of this band can be a “marker” of the degree of the twisting about CC double bond.

The data presented here suggests the structural change of the quinoline ring in the course of the twisting. 1144C has a positive charge, and possesses the  $C_2$  symmetry in the  $S_0$  state and the Franck-Condon state. Thus, in these states, both quinoline rings are equivalent, and the charge should be equally distributed on these quinoline rings. However, the symmetry lowering from  $C_2$  to  $C_1$  due to the twisting motion about the center CC double bond takes place in the  $S_1$  state. It is considered that such a structural change induces the imbalance of the charge distributions of two quinoline rings, i.e., the formation of the twisted intramolecular charge transfer (TICT)-like state<sup>33</sup>, giving rise to the structural change of the quinoline rings. In fact, the Mulliken charge analysis suggested the charge imbalance in the  $C_1$ -symmetric relaxed  $S_1$  state (Figure 6.7).

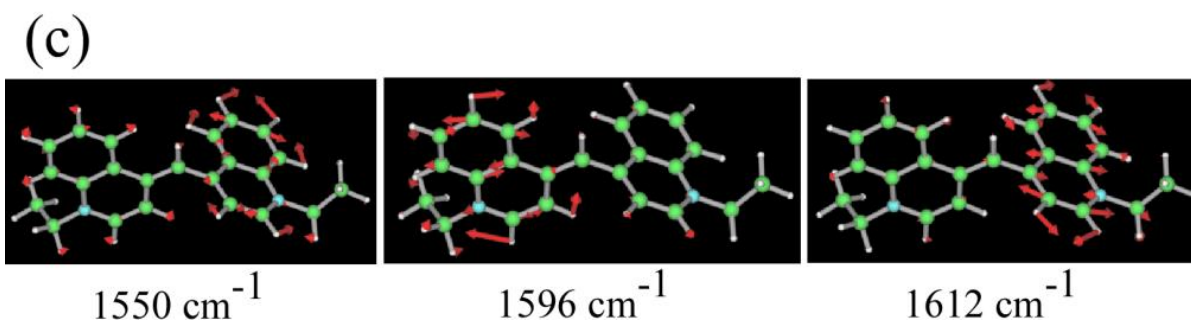
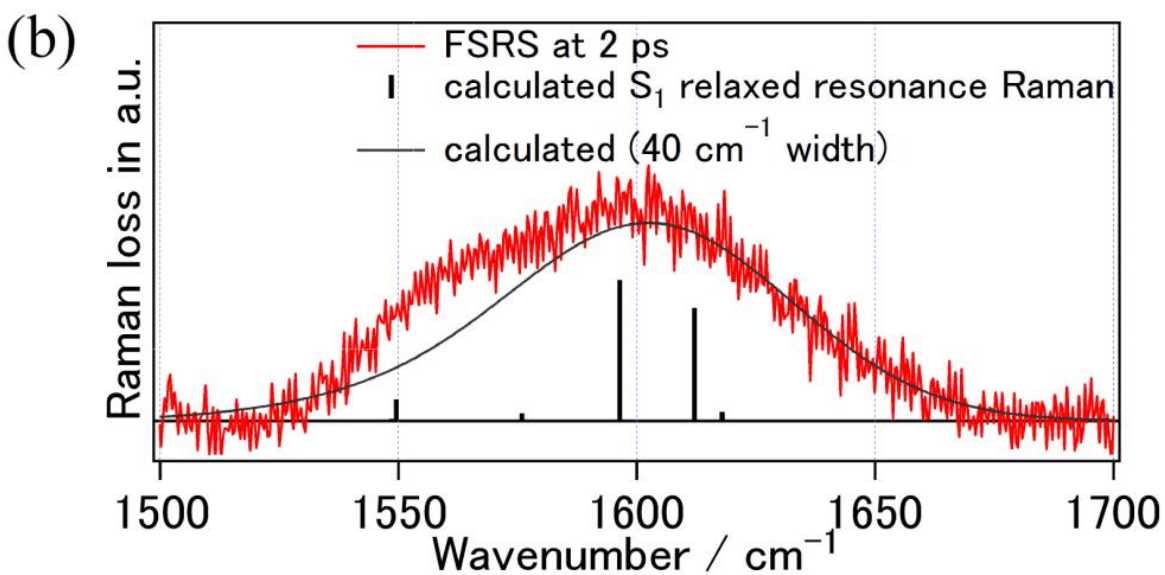
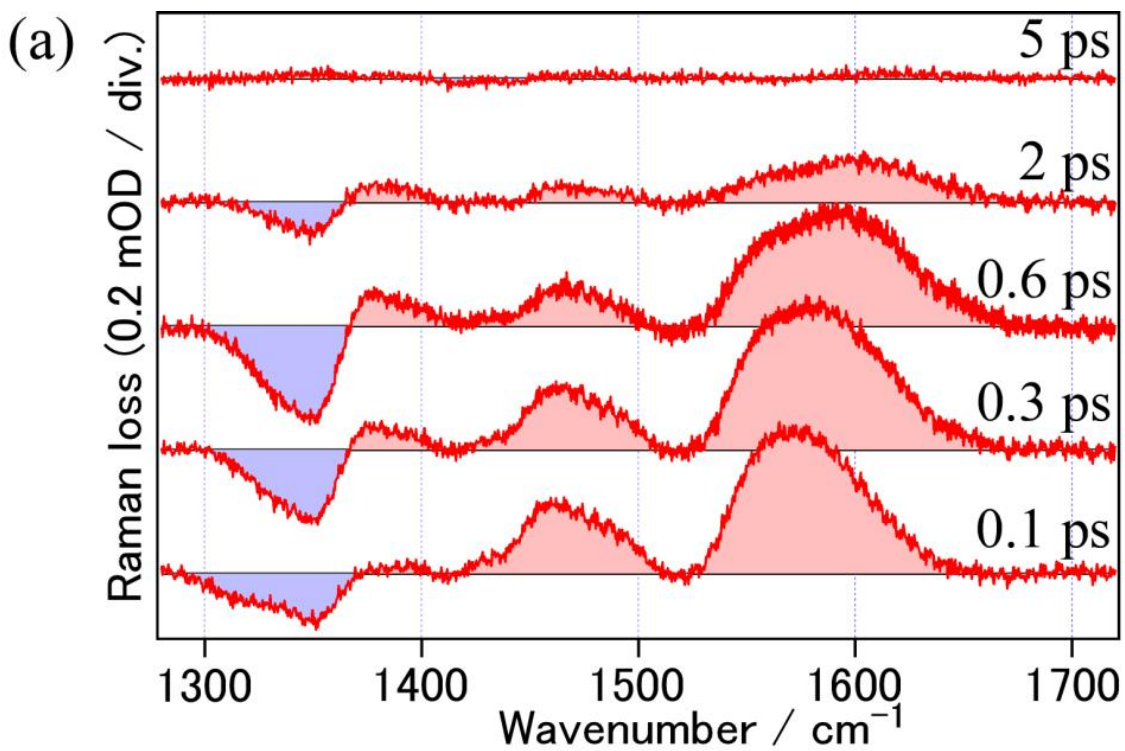


**Figure 6.6.** (a) Femtosecond stimulated Raman spectra at selected delays obtained with 1100-nm Raman pump. (b) The comparison between the spectrum at 2 ps and the resonance Raman spectrum of the relaxed  $S_1$  state calculated at TD-B3LYP/6-31+G(d) level (black bars) in 1500-1700  $\text{cm}^{-1}$  region. The scaling factor for the calculated Raman spectrum was 0.977. The calculated resonance Raman spectrum of the relaxed  $S_1$  state that takes the bandwidth (40  $\text{cm}^{-1}$ ) into consideration is also depicted with black line. (c) The normal modes corresponding to 1550, 1596 and 1612  $\text{cm}^{-1}$  bands. The energy and duration of the actinic pump were 200 nJ / pulse and  $\sim 100$  fs, respectively. The energy and duration of the Raman pump were 2  $\mu\text{J}$ /pulse and  $\sim 1.7$  ps, respectively.

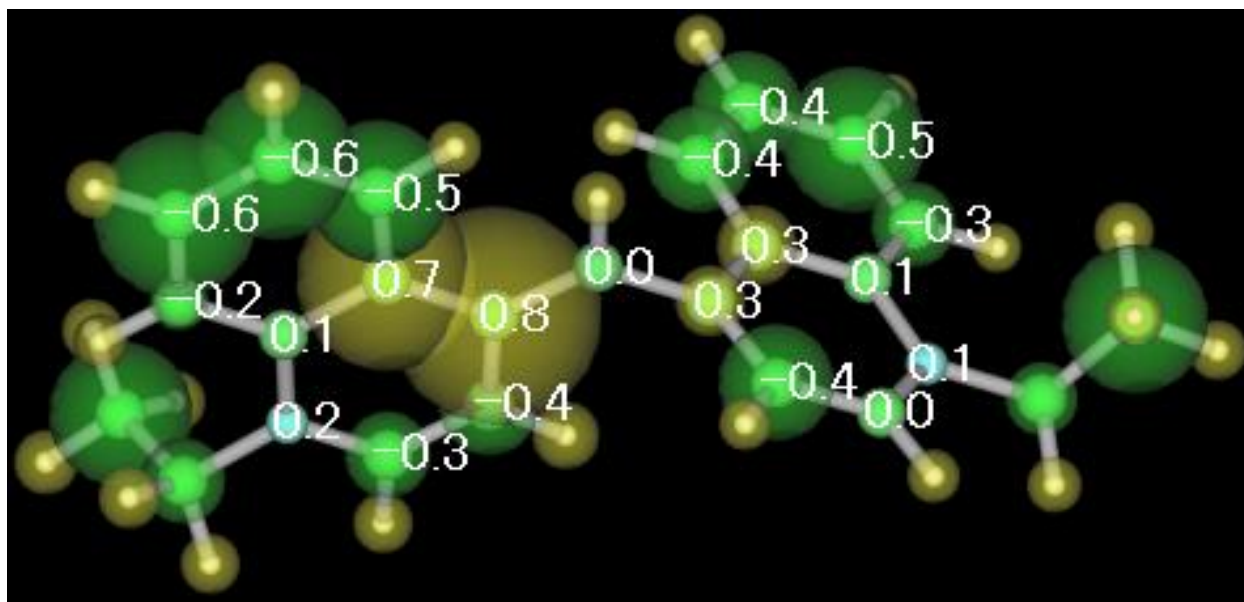


**Figure 6.7.** Mulliken charge in the relaxed  $S_1$  state calculated at TD-B3LYP/6-31+G(d) level. Yellow and green spheres indicate the distributions of the positive and negative charges, respectively.

### **Raman pump wavelength dependence of the FSRS spectrum**

FSRS spectra were measured at six Raman pump wavelengths ranging from 740 to 1100 nm. The normalized FSRS spectra at selected delays at each wavelength were shown in Figure 6.8. The Q1 band was observed irrespective of the Raman pump wavelength. At 740, 780 and 836 nm, this band exhibited no change in shape. On the other hand, at other wavelengths, this band exhibited upshift as well as that at 1100 nm. The Q1 band, which is composed of several quinoline ring stretching bands, appears at higher frequency as the Raman pump wavelength longer. In addition, the Q2 band becomes weaker. These Raman pump wavelength dependences were clearly recognized even before the subtraction of the baseline (Supporting figure 6.3). These demonstrate that different Raman pump wavelengths enable us to observe the Raman signal of the population in different region of the  $S_1$  potential energy surface which corresponds to different structure. The upshift of the Q1 band is a marker band of the degree of the twisting. Therefore, the Raman pump dependence of the FSRS spectrum indicates that more twisted 1144C is observed as the Raman pump wavelength becomes longer. Therefore, it is concluded that the twisting motion of 1144C gradually occurs in the  $S_1$  state.

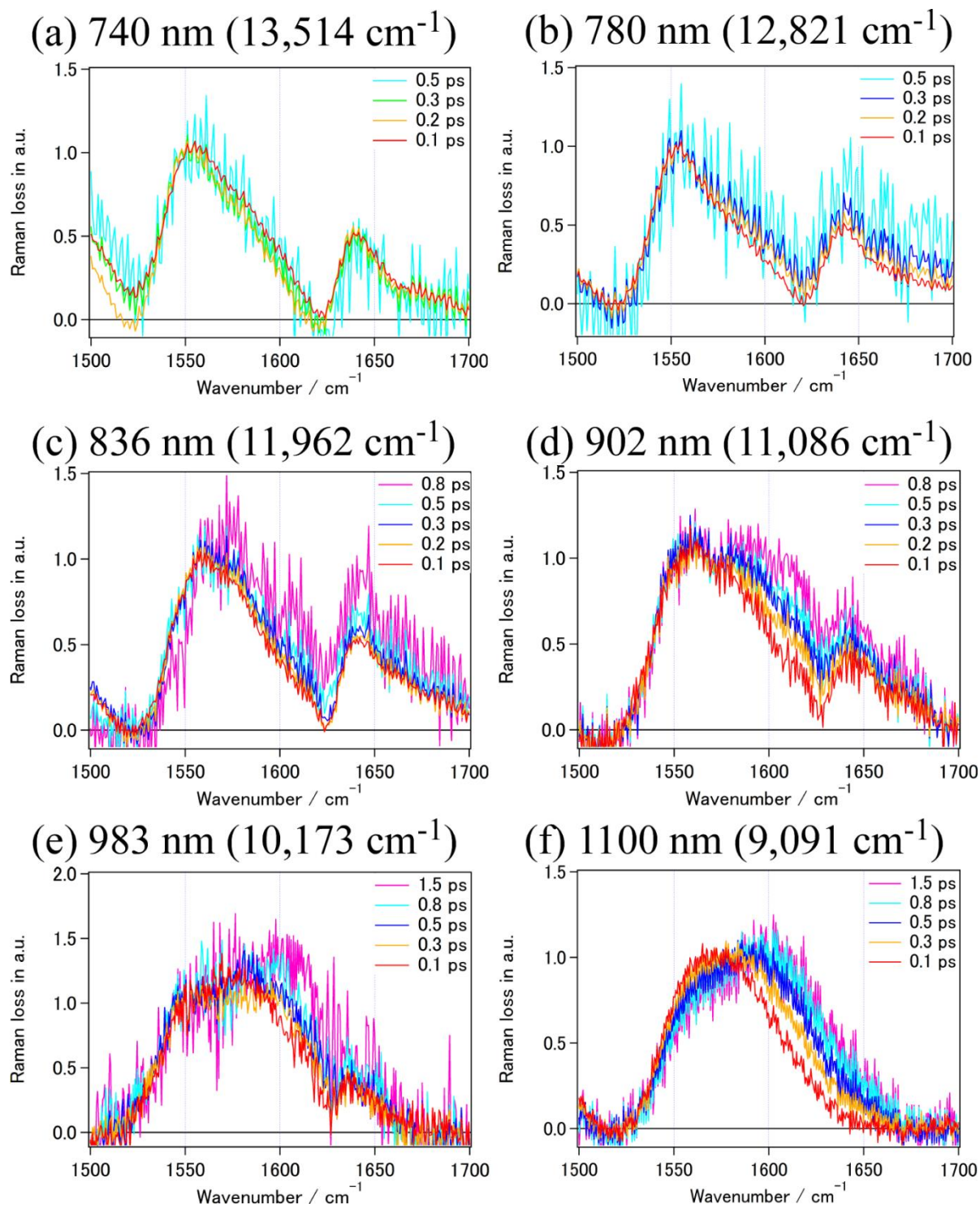


**Figure 6.8.** The normalized FSR spectra in 1500-1700  $\text{cm}^{-1}$  region at selected delays at (a) 740, (b) 780, (c) 836, (d) 902, (e) 983 and (f) 1100 nm. The experimental conditions are described in “Experimental methods” section.

It should be noted that the Raman signal whose spectral shape is dependent on the Raman pump wavelength was observed at each wavelength at 0.1 ps, suggesting that the population distributes inhomogeneously in the  $S_1$  state along the twisting coordinate even at the early delay. To visualize the distribution of the  $S_1$  population, two-dimensional spectra at selected delays were constructed as shown in Figure 6.9. (The FSRS spectrum at each Raman pump wavelength at selected delays, which is used to construct the 2D spectrum, is shown in Supporting figure 6.4.) The horizontal and vertical axes are the frequencies of the Raman pump and Raman shift, respectively. The FSRS spectrum at each Raman pump wavelength is normalized by the peak amplitude of the Q1 band at 0.1 ps. At 0.1 ps, two-dimensional peak of the Q1 band, which is slightly tilted, is spreading along the Raman pump frequency axis, indicating that the cyanine molecules are distributed inhomogeneously along the twisting coordinate. The spreading of the wavepacket observed by pump-dump-probe spectroscopy suggests that the structural distribution gradually gets wider<sup>18</sup>. However, since the electronic spectroscopy does not give any structural information, it was unable to elucidate how the structural distribution spreads on the multidimensional potential surface. In the present study, using FSRS technique, it was uncovered that the distribution of the 1144C created on the  $S_1$  potential spreads along the twisting coordinate.

At 0.3 ps, the Q1 band diminished at the Raman pump frequency higher than  $12000\text{ cm}^{-1}$ , indicating that the cyanine molecules in the vicinity of the Franck-Condon state were twisted and moved toward the relaxed  $S_1$  state. At 0.8 ps, the Raman signals at Raman pump frequency higher than  $12000\text{ cm}^{-1}$  decayed further, and a further peak shift of the Q1 band was observed, indicating that the cyanine molecules were twisted even more, and the population, which exhibit the stimulated emission in the wavenumber region of  $>12000\text{ cm}^{-1}$ , significantly decreased. Finally, at 2 ps, the Raman signals were observed only in the wavenumber region of  $<12000\text{ cm}^{-1}$ , and the peak frequency of the Q1 band upshifted more than  $20\text{ cm}^{-1}$  with respect to that at 0.1 ps, suggesting that most of the cyanine molecules are in the relaxed  $S_1$  state. The distribution dynamics of 1144C suggested by the 2D spectra is described in Figure 6.10.

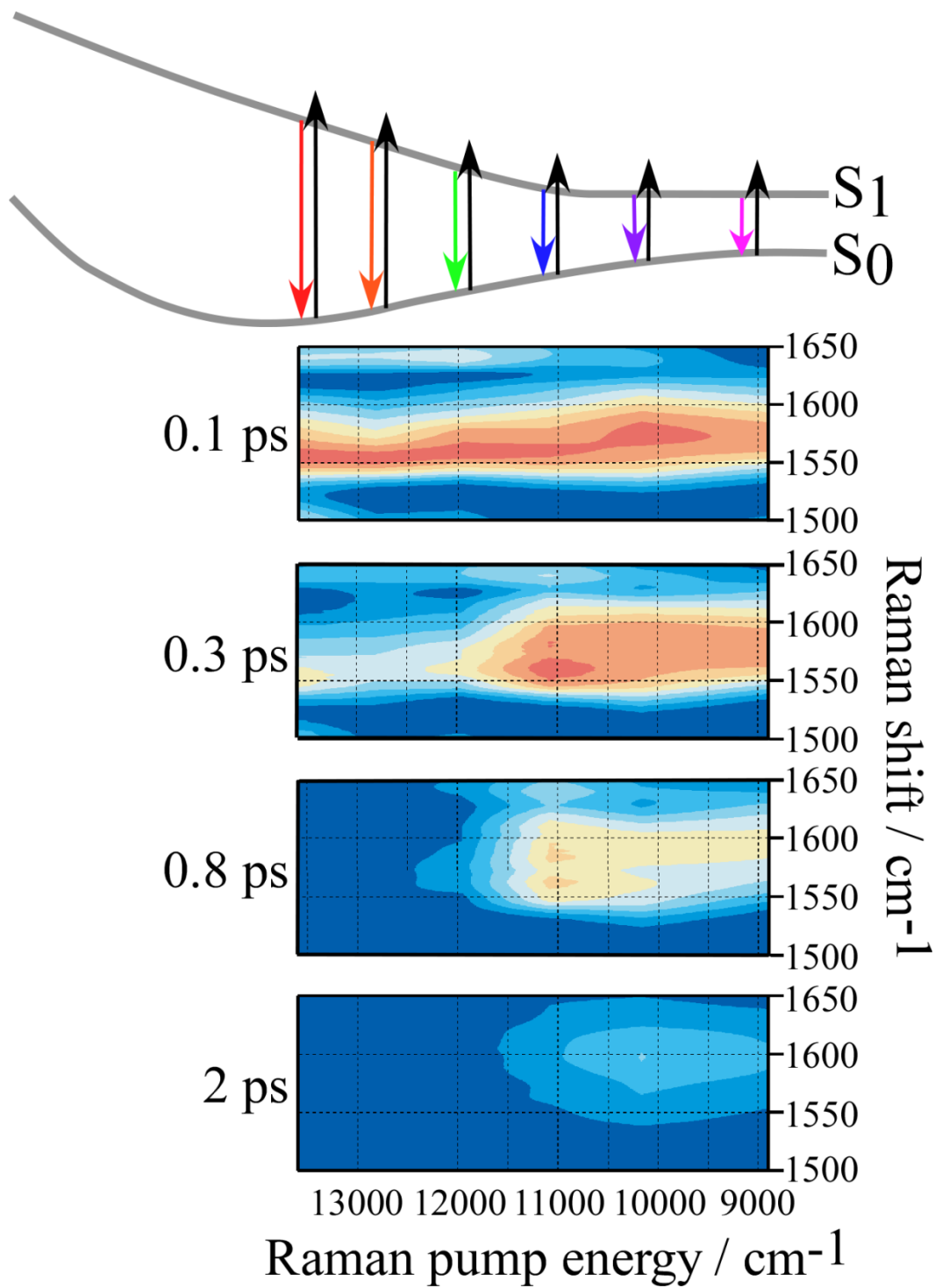


**Figure 6.9.** The 2D representation of the FSR spectra at each delay time. The FSR spectra are normalized at peak value at 0.1 ps, and the same factors were multiplied at each delay. The horizontal axis is the frequency of the Raman pump. The vertical axis corresponds to the Raman shift. The experimental conditions are described in “Experimental methods” section.

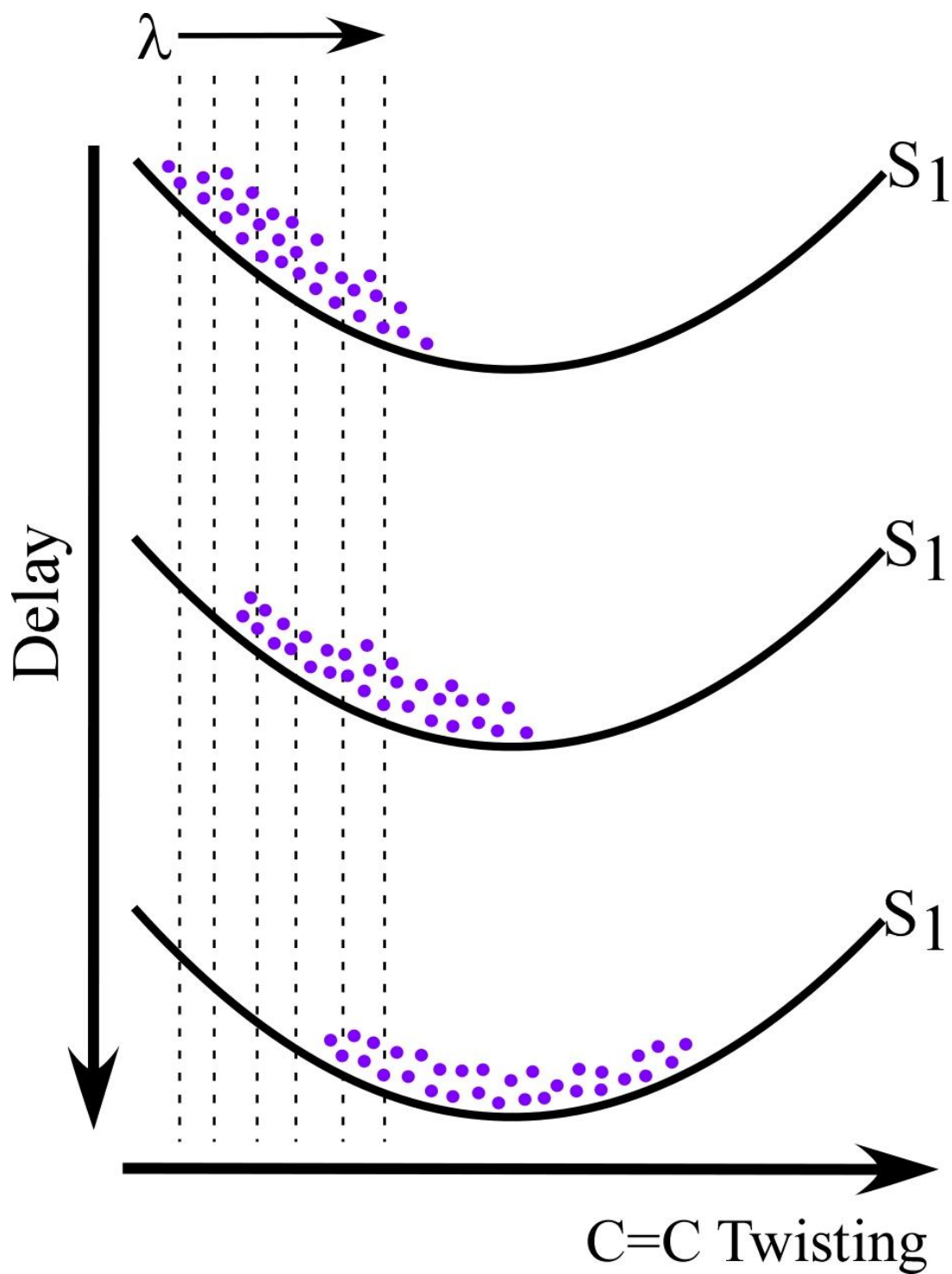


**Figure 6.10.** Schematic illustration of the dynamics of the structural distribution of 1144C in the  $S_1$  state suggested by the present experimental data.

The spectral shift observed at fixed Raman pump wavelength is rationalized by taking account for the finite bandwidth of the stimulated emission arising from the  $S_1$  population on a certain region of the potential energy surface. It is natural to think that the Raman signal of the cyanine molecules whose center wavelength of the stimulated emission is longer or shorter than that of the Raman pump can be also detected. Therefore, it is considered that the ensemble having a finite distribution of the degree of the twisting should be detected even at one Raman pump wavelength. For this reason, the obtained spectra at a fixed Raman pump wavelength also should reflect the dynamics of the distribution, giving rise to the spectral shift of the Q1 band due to the twisting motion.

The transient absorption and FSRS spectra measured at  $<900$  nm decayed faster than the  $S_1$  deactivation ( $\sim 1.3$  ps), suggesting that the molecules in the potential region where exhibits the  $S_1 \rightarrow S_0$  stimulated emission at  $<900$  nm rapidly change their structure. This indicates that the potential in the vicinity of the Franck-Condon state is steep. In such potential region, the stimulated emission wavelength drastically changes, making the potential range observed by a narrowband Raman pump limited. The narrow observation window due to the steepness of the potential in  $<900$  nm region can rationalize that the spectral shape observed at 740, 780 and 836 nm Raman pump wavelengths exhibited no change. On the other hand, the FSRS spectra measured at 902, 983 and 1100 nm which exhibited the Raman pump wavelength dependence of the spectral shape decayed with a lifetime of the  $S_1$  state. This suggests that the distribution inhomogeneously spreads among the probed region. This implies that this potential region is considerably flat compared with the vicinity of the Franck-Condon state.

In the previous study of the 1144C in ethylene glycol<sup>18</sup>, the faster decay at short wavelengths was not observed, differently from the present study. This difference can be rationalized by considering the difference in the dynamics in the vicinity of the Franck-Condon state between different solvents. The dynamics in the vicinity of the Franck-Condon state should be dependent on the solvent, because the symmetry of 1144C should be lowered ( $C_2 \rightarrow C_1$ ) by the fluctuation due to the solvent.

Finally, it should be noted that the near-IR FSRS can be a promising method to elucidate the structural distribution dynamics in the potential region where two electronic potential approaches such as in the vicinity of the conical intersection<sup>34</sup>.

## 6.4 Conclusions

The structural dynamics of the barrierless photoreaction of 1,1'-diethyl-4,4'-cyanine (1144C) in the  $S_1$  state was investigated by femtosecond stimulated Raman spectroscopy (FSRS). The FSRS spectra were measured at six Raman pump wavelengths ranging from 740 to 1100 nm. The Raman pump wavelength dependence of the FSRS spectrum at 0.1 ps shows that the quinoline ring stretching band ( $1550\text{-}1600\text{ cm}^{-1}$ ) appears at higher frequency with increasing Raman pump wavelength. This observation manifests that this method can capture the structural dynamics during photoisomerization, and that the structural change of the quinoline ring takes place concomitantly with the isomerization of the cyanine dye. Moreover, the gradual twisting of the inhomogeneously distributed cyanine molecules in the  $S_1$  state was visualized based on the Raman pump wavelength dependence of the time-resolved spectra.

## 6.5 References

- (1) Bagchi, B.; Fleming, G. R., Dynamics of activationless reactions in solution. *J. Phys. Chem.* **1990**, *94*, 9-20.
- (2) Saltiel, J.; Waller, A. S.; Sears, D. F., The temperature and medium dependencies of cis-stilbene fluorescence. The energetics of twisting in the lowest excited singlet state. *J. Am. Chem. Soc.* **1993**, *115*, 2453-2465.
- (3) Åkesson, E.; Bergström, H.; Sundström, V.; Gillbro, T., Photochemical isomerization in the absence of a potential barrier. *Chem. Phys. Lett.* **1986**, *126*, 385-393.
- (4) Bagchi, B.; Fleming, G. R.; Oxtoby, D. W., Theory of electronic relaxation in solution in the absence of an activation barrier. *J. Chem. Phys.* **1983**, *78*, 7375-7385.
- (5) Åberg, U.; Sundström, V., Photochemical isomerization in the absence of a potential barrier: origin of wavelength-dependent ground-state recovery kinetics. *Chem. Phys. Lett.* **1991**, *185*, 461-467.
- (6) Åberg, U.; Åkesson, E.; Sundström, V., Excited state dynamics of barrierless isomerization in solution. *Chem. Phys. Lett.* **1993**, *215*, 388-394.
- (7) Yartsev, A.; Alvarez, J.-L.; Åberg, U.; Sundström, V., Overdamped wavepacket motion along a barrierless potential energy surface in excited state isomerization. *Chem. Phys. Lett.* **1995**, *243*, 281-289.
- (8) Alvarez, J.-L.; Yartsev, A.; Åberg, U.; Åkesson, E.; Sundström, V., Resolving the Turnover of Temperature Dependence of the Reaction Rate in Barrierless Isomerization. *J. Phys. Chem. B* **1998**, *102*, 7651-7658.
- (9) Sanchez-Galvez, A.; Hunt, P.; Robb, M. A.; Olivucci, M.; Vreven, T.; Schlegel, H. B., Ultrafast Radiationless Deactivation of Organic Dyes: Evidence for a Two-State Two-Mode Pathway in Polymethine Cyanines. *J. Am. Chem. Soc.* **2000**, *122*, 2911-2924.
- (10) Xu, Q.-H.; Fleming, G. R., Isomerization Dynamics of 1,1'-Diethyl-4,4'-Cyanine (1144C) Studied by Different Third-Order Nonlinear Spectroscopic Measurements. *J. Phys. Chem. A* **2001**, *105*, 10187-10195.
- (11) Improta, R.; Santoro, F., A Theoretical Study on the Factors Influencing Cyanine Photoisomerization: The Case of Thiacyanine in Gas Phase and in Methanol. *J. Chem. Theor. Comput.* **2005**, *1*, 215-229.
- (12) Dietzek, B.; Brüggemann, B.; Pascher, T.; Yartsev, A., Mechanisms of Molecular Response in the Optimal Control of Photoisomerization. *Phys. Rev. Lett.* **2006**, *97*.
- (13) Dietzek, B.; Christensson, N.; Pascher, T.; Pullerits, T.; Yartsev, A., Ultrafast Excited-State Isomerization Dynamics of 1,1'-Diethyl-2,2'-Cyanine Studied by Four-Wave Mixing Spectroscopy. *J. Phys. Chem. B* **2007**, *111*, 5396-5404.
- (14) Dietzek, B.; Pascher, T.; Yartsev, A., Tracking Ultrafast Excited-State Bond-Twisting Motion in Solution Close to the Franck–Condon Point. *J. Phys. Chem. B* **2007**, *111*, 6034-6041.
- (15) Dietzek, B.; Yartsev, A.; Tarnovsky, A. N., Watching Ultrafast Barrierless Excited-State Isomerization of Pseudocyanine in Real Time. *J. Phys. Chem. B* **2007**, *111*, 4520-4526.

- (16) Dietzek, B.; Brüggemann, B.; Persson, P.; Yartsev, A., On the excited-state multi-dimensionality in cyanines. *Chem. Phys. Lett.* **2008**, *455*, 13-19.
- (17) Dietzek, B.; Tarnovsky, A. N.; Yartsev, A., Visualizing overdamped wavepacket motion: Excited-state isomerization of pseudocyanine in viscous solvents. *Chem. Phys.* **2009**, *357*, 54-62.
- (18) Wei, Z.; Nakamura, T.; Takeuchi, S.; Tahara, T., Tracking of the Nuclear Wavepacket Motion in Cyanine Photoisomerization by Ultrafast Pump–Dump–Probe Spectroscopy. *J. Am. Chem. Soc.* **2011**, *133*, 8205-8210.
- (19) Weigel, A.; Pfaffe, M.; Sajadi, M.; Mahrwald, R.; Improta, R.; Barone, V.; Polli, D.; Cerullo, G.; Ernsting, N. P.; Santoro, F., Barrierless photoisomerisation of the "simplest cyanine": Joining computational and femtosecond optical spectroscopies to trace the full reaction path. *Phys. Chem. Chem. Phys.* **2012**, *14*, 13350-13364.
- (20) Yoshioka, H.; Nakatsu, K., Crystal structures of two photographic sensitizing dyes, 1,1'-diethyl-2,2'-cyanine bromide and 1,1'-diethyl-4,4'-cyanine bromide. *Chem. Phys. Lett.* **1971**, *11*, 255-258.
- (21) Åberg, U.; Åkesson, E.; Alvarez, J. L.; Fedchenia, I.; Sundström, V., Femtosecond spectral evolution monitoring the bond-twisting event in barrierless isomerization in solution. *Chem. Phys.* **1994**, *183*, 269-288.
- (22) Ruhman, S.; Hou, B.; Friedman, N.; Ottolenghi, M.; Sheves, M., Following Evolution of Bacteriorhodopsin in Its Reactive Excited State via Stimulated Emission Pumping. *J. Am. Chem. Soc.* **2002**, *124*, 8854-8858.
- (23) Kennis, J. T. M.; Larsen, D. S.; van Stokkum, I. H. M.; Vengris, M.; van Thor, J. J.; van Grondelle, R., Uncovering the hidden ground state of green fluorescent protein. *Proc. Natl. Acad. Sci. USA* **2004**, *101*, 17988-17993.
- (24) Yoshizawa, M.; Kurosawa, M., Femtosecond time-resolved Raman spectroscopy using stimulated Raman scattering. *Phys. Rev. A* **1999**, *61*, 013808.
- (25) Kukura, P.; McCamant, D. W.; Yoon, S.; Wandschneider, D. B.; Mathies, R. A., Structural Observation of the Primary Isomerization in Vision with Femtosecond-Stimulated Raman. *Science* **2005**, *310*, 1006-1009.
- (26) Kukura, P.; McCamant, D. W.; Mathies, R. A., Femtosecond Stimulated Raman Spectroscopy. *Annu. Rev. Phys. Chem.* **2007**, *58*, 461-488.
- (27) Takaya, T.; Iwata, K., Relaxation Mechanism of  $\beta$ -Carotene from S<sub>2</sub> (1B<sub>u</sub><sup>+</sup>) State to S<sub>1</sub> (2A<sub>g</sub><sup>-</sup>) State: Femtosecond Time-Resolved Near-IR Absorption and Stimulated Resonance Raman Studies in 900–1550 nm Region. *J. Phys. Chem. A* **2014**, *118*, 4071-4078.
- (28) Frisch, M. J.; Trucks, G. W.; Schlegel, H. B.; Scuseria, G. E.; Robb, M. A.; Cheeseman, J. R.; Scalmani, G.; Barone, V.; Mennucci, B.; Petersson, G. A.; Nakatsuji, H.; Caricato, M.; Li, X.; Hratchian, H. P.; Izmaylov, A. F.; Bloino, J.; Zheng, G.; Sonnenberg, J. L.; Hada, M.; Ehara, M.; Toyota, K.; Fukuda, R.; Hasegawa, J.; Ishida, M.; Nakajima, T.; Honda, Y.; Kitao, O.; Nakai, H.; Vreven, T.; Montgomery Jr., J. A.; Peralta, J. E.; Ogliaro, F.; Bearpark, M. J.; Heyd, J.; Brothers, E. N.; Kudin, K. N.; Staroverov, V. N.; Kobayashi, R.; Normand, J.; Raghavachari, K.;

Rendell, A. P.; Burant, J. C.; Iyengar, S. S.; Tomasi, J.; Cossi, M.; Rega, N.; Millam, N. J.; Klene, M.; Knox, J. E.; Cross, J. B.; Bakken, V.; Adamo, C.; Jaramillo, J.; Gomperts, R.; Stratmann, R. E.; Yazyev, O.; Austin, A. J.; Cammi, R.; Pomelli, C.; Ochterski, J. W.; Martin, R. L.; Morokuma, K.; Zakrzewski, V. G.; Voth, G. A.; Salvador, P.; Dannenberg, J. J.; Dapprich, S.; Daniels, A. D.; Farkas, Ö.; Foresman, J. B.; Ortiz, J. V.; Cioslowski, J.; Fox, D. J. *Gaussian 09*, Gaussian, Inc.: Wallingford, CT, USA, 2009.

(29) Lee, S.-Y.; Heller, E. J., Time-dependent theory of Raman scattering. *J.Chem. Phys.* **1979**, *71*, 4777.

(30) Eric J. Heller, R. L. S., and David Tannor, Simple Aspects of Raman Scattering. *J. Phys. Chem.* **1982**, *1982*, 1822-1833.

(31) Myers, A. B.; Harris, R. A.; Mathies, R. A., Resonance Raman excitation profiles of bacteriorhodopsin. *J. Chem. Phys.* **1983**, *79*, 603.

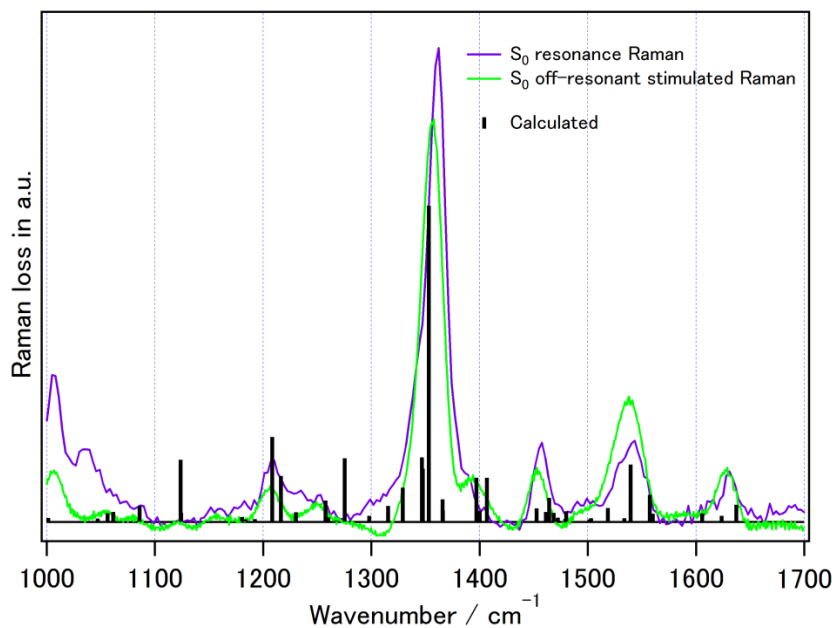
(32) Nakamura, R.; Hamada, N.; Abe, K.; Yoshizawa, M., Ultrafast Hydrogen-Bonding Dynamics in the Electronic Excited State of Photoactive Yellow Protein Revealed by Femtosecond Stimulated Raman Spectroscopy. *J. Phys. Chem. B* **2012**, *116*, 14768-14775.

(33) Rettig, W., Charge Separation in Excited States of Decoupled Systems—TICT Compounds and Implications Regarding the Development of New Laser Dyes and the Primary Process of Vision and Photosynthesis. *Angew. Chem. Int. Ed.* **1986**, *25*, 971-988.

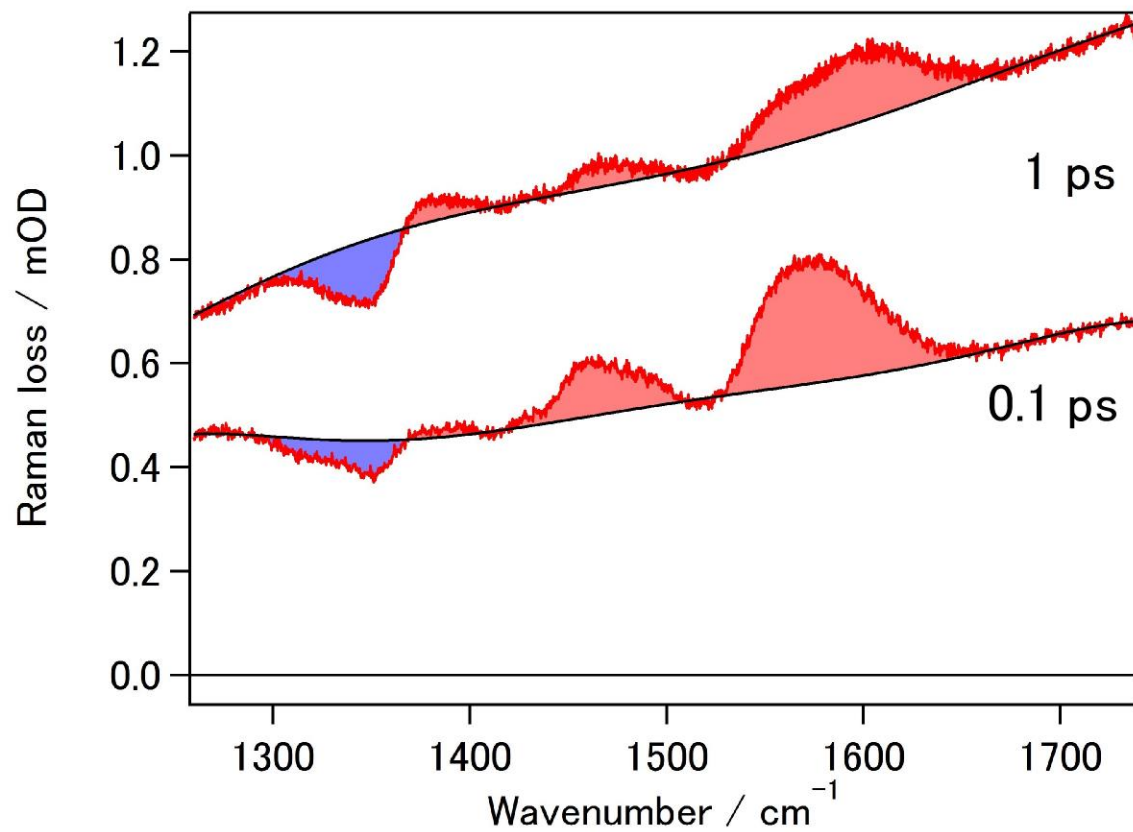
(34) Polli, D.; Altoe, P.; Weingart, O.; Spillane, K. M.; Manzoni, C.; Brida, D.; Tomasello, G.; Orlandi, G.; Kukura, P.; Mathies, R. A.; Garavelli, M.; Cerullo, G., Conical intersection dynamics of the primary photoisomerization event in vision. *Nature* **2010**, *467*, 440-443.

## 6.6 Appendix

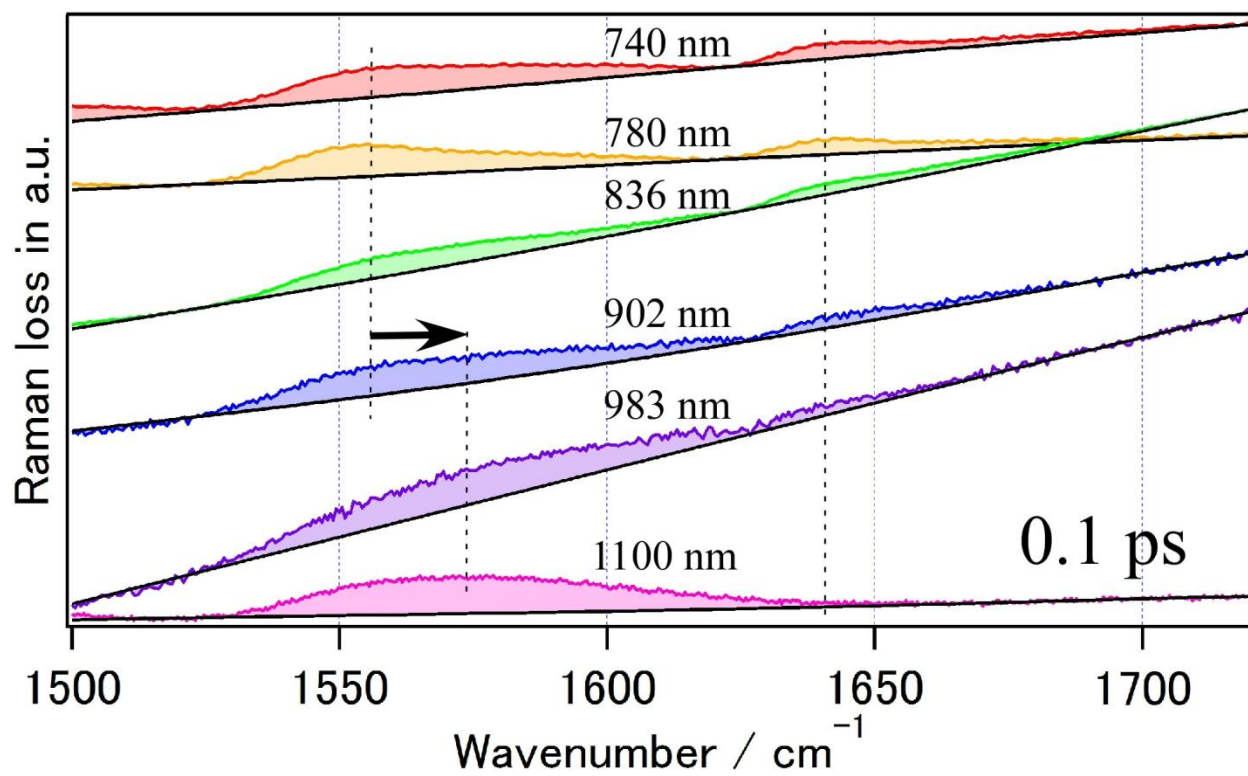
### Appendix1: Supporting figures



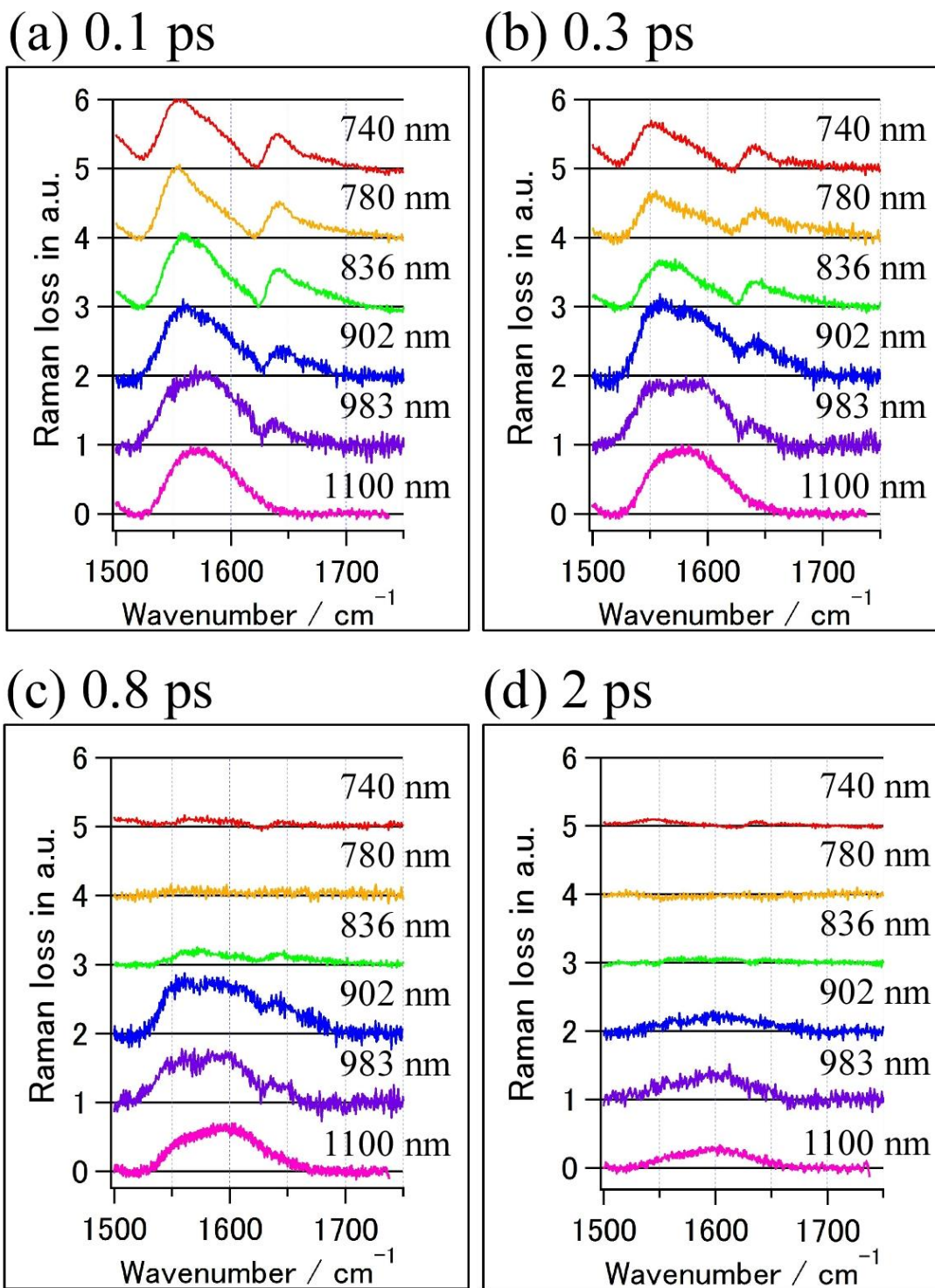
**Supporting figure 6.1.** Comparison of the experimentally and theoretically obtained Raman spectra of 1144C in the  $S_0$  state. The  $S_0$  state resonance Raman spectrum was obtained by 514-nm cw excitation. The  $S_0$  state off-resonant stimulated Raman spectrum was obtained by 740-nm Raman pump (0.5  $\mu\text{J}$  / pulse). The calculated non-resonant Raman spectrum was obtained at B3LYP/6-311+G(d,p) level with the PCM correction (black bars).



**Supporting figure 6.2.** Comparison of the baseline-unsubtracted FSRS spectra at 0.1 ps and 1 ps measured with the 1100-nm Raman pump ( $2 \mu\text{J} / \text{pulse}$ ).



**Supporting figure 6.3.** Comparison of the baseline-unsubtracted FSRS spectrum at 0.1 ps measured at each Raman pump wavelength. The measurement conditions are described in “Experimental methods” section.



**Supporting figure 6.4.** Comparison of the FSRS spectrum at (a) 0.1, (b) 0.3, (c) 0.8, and (d) 2 ps measured at each Raman pump wavelength. The measurement conditions are described in “Experimental methods” section.

## Appendix2: Inverse-Raman-Like Process from vibrationally excited state

In this chapter, a dispersive line at  $\sim 1350 \text{ cm}^{-1}$  observed in the FSRS spectrum was observed, and assigned to an inverse-Raman-like process from vibrationally excited state.

Based on the density matrix treatment of the third-order nonlinear process, the nonlinear spectroscopic signals can be calculated<sup>1,2</sup>. Here, the expression of the inverse-Raman-like process is described. Before discussing this process, the expression of the stimulated Raman scattering (SRS) is derived for comparison.

Because the signal is detected in the direction of the probe  $\mathbf{k}_{\text{Pr}}$ , considering the phase-matching condition, what we can detect is the radiation from the third order nonlinear polarization created by the interaction between the sample and the three electric fields  $E_p \exp(-i\omega_p t + i\mathbf{k}_p \cdot \mathbf{or})$ ,  $E_R^* \exp(-i\omega_R t + i\mathbf{k}_R \cdot \mathbf{or})$  and  $E_R \exp(i\omega_R t - i\mathbf{k}_R \cdot \mathbf{or})$ . Therefore, third-order nonlinear susceptibility  $\chi^{(3)}(\nu_R)$  responsible for the detected signal has the frequencies  $\omega_{\text{Pr}}$ ,  $\omega_R$  and  $-\omega_R$  as parameters. The experimentally observed  $\Delta A(\nu_R, \Delta T)$  is proportional to third-order nonlinear susceptibility  $\chi^{(3)}(\nu_R; \omega_{\text{Pr}}, \omega_R, -\omega_R)$  because

$$\Delta A(\nu_R, \Delta T) = -\log \frac{I_{ON}(\nu_R, \Delta T)}{I_{OFF}(\nu_R, \Delta T)} = -\log \frac{|E_{\text{Pr}} + E_{\mathbf{k}_{\text{Pr}}}^{(3)}|^2}{|E_{\text{Pr}}|^2} \sim \frac{2 \text{Re}(E_{\text{Pr}}^* E_{\mathbf{k}_{\text{Pr}}}^{(3)})}{|E_{\text{Pr}}|^2} \propto \text{Im} \chi^{(3)}(\nu_R; \omega_{\text{Pr}}, \omega_R, -\omega_R)$$

where  $E_{\text{Pr}}$  and  $E_{\mathbf{k}_{\text{Pr}}}^{(3)}$  are the electric fields of the probe and the radiation from the third-order nonlinear polarization in the direction of the probe  $\mathbf{k}_{\text{Pr}}$ . Therefore, the calculation of the  $\text{Im} \chi^{(3)}(\nu_R)$  directly gives the expression of the signal. However,  $\chi^{(3)}(\nu_R; \omega_{\text{Pr}}, \omega_R, -\omega_R)$  is composed of multiple terms which are responsible for distinct spectroscopic signals including SRS (and hot luminescence terms). This is because there are  $3! = 6$  orders of three interactions of the electric fields. Herein, only the representation of the  $\chi^{(3)}(\nu_R)$  responsible for the stimulated Raman signal is calculated.

Although there are some different ways to calculate<sup>1,2</sup>, a method developed by Albrecht is used here<sup>2</sup>. In this calculation, the following assumptions were made.

- The interaction between molecule and electric fields of the lights is so weak that the change in quantum state of molecule due to the perturbation is small.
- The size of the molecule is negligibly small with respect to the wavelength of the Raman pump and the probe.
- The Raman pump and the probe is continuous wave.
- Only three vibronic states  $S_{1,v=0}$ ,  $S_{1,v=1}$  and  $S_{0,v=v'}$  are involved.
- The initial state is  $S_{1,v=0}$ .
- The Raman signal is detected in anti-*Stokes* region.
- The Raman pump is resonant with the  $S_1 \rightarrow S_0$  stimulated emission.
- The electronic and vibrational coherences are lost in exponential fashion.

The diagram of the SRS of the  $S_1$  state is represented in Figure 6A.

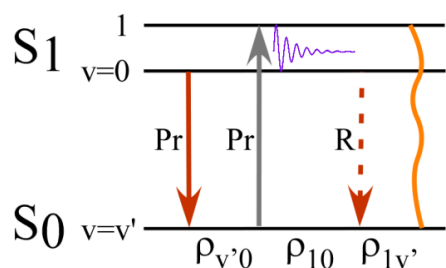


**Figure 6A.** Time-evolution diagram of density matrix corresponding to the SRS process starting from the  $S_1$  state. The Brown and gray arrows represent the interaction of the Raman pump and probe, respectively. The solid and broken arrows indicate the evolution of ket and sides of density matrix, respectively. Orange vertical wavy line indicates the third-order nonlinear polarization. Purple wavy line indicates the vibrational coherence.  $\rho$  at the bottom of the figure indicates the Liouville state. The SRS is detected in anti-Stokes region using Raman pump resonant with the  $S_1$ - $S_0$  stimulated emission.

From this diagram,  $\chi^{SRS}(\nu_R)$  and  $\text{Im} \chi^{SRS}(\nu_R)$  are obtained as follows

$$\chi^{SRS}(\nu_R) = \frac{N\eta^{-3}|\mu_{1\nu'}\mu_{\nu'0}|^2}{(\omega_{0\nu'} - \omega_R + i\Gamma_{0\nu'})(\omega_{10} - \nu_R + i\Gamma_{10})(\omega_{1\nu'} - \omega_R - \nu_R - i\Gamma_{1\nu'})}$$

$$\text{Im} \chi^{SRS}(\nu_R) = \frac{N\eta^{-3}|\mu_{1\nu'}\mu_{\nu'0}|^2}{|\omega_{0\nu'} - \omega_R + i\Gamma_{0\nu'}|^2 |\omega_{10} - \nu_R + i\Gamma_{10}|^2}$$

where  $\mu_{1\nu'}$  and  $\mu_{\nu'0}$  are the amplitude of the transition dipole moments associated with the transitions  $S_{1,\nu=1} - S_{0,\nu=\nu'}$  and  $S_{0,\nu=\nu'} - S_{1,\nu=0}$ ,  $\omega$ 's are energy differences between two states and  $\Gamma_{0\nu'}$  and  $\Gamma_{10}$  are electronic and vibrational dephasing rates associated with two states. Therefore,  $\Delta A(\nu_R, \Delta T)$  responsible for the stimulated Raman signal is positive (Raman loss) and Lorentzian function with respect to  $\nu_R$ .

Next, the origin of a dispersive line at  $\sim 1350 \text{ cm}^{-1}$  observed in FSRS spectrum is discussed. It should be noted that only  $\sim 1350\text{-cm}^{-1}$  band appears dispersive, whereas the other bands are not. Because of this mode specificity, it can be considered that only  $\sim 1350\text{-cm}^{-1}$  mode is vibrationally excited whereas the others are in the lowest vibrational level.

The vibrationally excited state is expected to exhibit the inverse-Raman-like signal. The diagram for this process is depicted in Figure 6B.

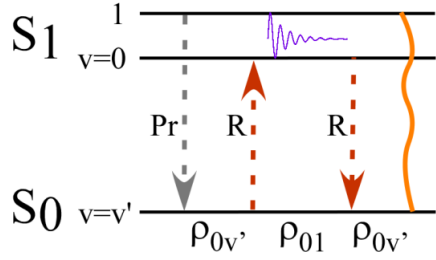


**Figure 6B.** Time-evolution diagram of density matrix corresponding to the inverse-Raman-like process from the vibrationally excited  $S_1$  state. The Brown and gray arrows represent the interaction of the Raman pump and probe, respectively. The solid and broken arrows indicate the evolution of ket and sides of density matrix, respectively. Orange vertical wavy line indicates the third-order nonlinear polarization. Purple wavy line indicates the vibrational coherence.  $\rho$  at the bottom of the figure indicates the Liouville state. The SRS is detected in anti-Stokes region using Raman pump resonant with the  $S_1$ - $S_0$  stimulated emission.

From this diagram,  $\chi^{IRS(v=1)}(\nu_R)$  and  $\text{Im} \chi^{IRS(v=1)}(\nu_R)$  are obtained as follows

$$\chi^{IRS(v=1)}(\nu_R) = \frac{N\eta^{-3} |\mu_{1v'} \mu_{10}|^2}{(\omega_{1v'} - \omega_R - \nu_R - i\Gamma_{1v'})^2 (\omega_{10} - \nu_R + i\Gamma_{10})}$$

$$\text{Im} \chi^{IRS(v=1)}(\nu_R) = \frac{N\eta^{-3} |\mu_{1v'} \mu_{10}|^2}{|\omega_{1v'} - \omega_R - \nu_R - i\Gamma_{1v'}|^4 |\omega_{10} - \nu_R + i\Gamma_{10}|^2} \cdot [-\{(\omega_{1v'} - \omega_R - \nu_R)^2 - \Gamma_{1v'}^2\} \Gamma_{10} + 2\Gamma_{1v'} (\omega_{1v'} - \omega_R - \nu_R) (\omega_{10} - \nu_R)]$$

The expression in the [ ] is quadratic with respect to the  $\nu_R$ . Therefore,  $\Delta A(\nu_R, \Delta T) \propto \text{Im} \chi^{IRS(v=1)}(\nu_R)$  can be both positive and negative.

## References

- (1) Mukamel, S. Principles of Nonlinear Optical Spectroscopy **1999**,
- (2) Lee, D.; Albrecht, A. C. A Unified View of Raman, Resonance Raman, and Fluorescence Spectroscopy (and Their Analogues in Two-Photon Absorption). *Advances in Infrared and Raman Spectroscopy* **1985**, *12*, 179-213.



## Chapter 7: General Conclusions

In this dissertation, the photoisomerization reactions of the retinal chromophore in microbial rhodopsins and a cyanine dye in solution are studied by femtosecond electronic and vibrational spectroscopy. In chapters 3 to 5, microbial rhodopsins, *Anabaena* sensory rhodopsin (ASR) and KR2, were studied by femtosecond time-resolved fluorescence and absorption spectroscopy. In chapter 6, the structural dynamics during photoisomerization of a cyanine dye was studied by femtosecond stimulated Raman spectroscopy.

In chapter 3, femtosecond time-resolved Kerr-gate fluorescence measurements of all-*trans* and 13-*cis* ASR were carried out. Femtosecond Kerr-gate fluorescence measurement revealed that, in ASR, the photoisomerization of the 13-*cis* retinal proceeds with a time constant of 250 fs whereas that of the all-*trans* retinal takes place with a time constant of 700 fs. As in the case of the photoisomerizations of PRSB in solution, it was revealed that *cis-trans* photoisomerization is faster than *trans-cis* photoisomerization for PRSB in the ASR proteins.

In chapter 4, femtosecond time-resolved absorption measurement of KR2 at physiological pH (pH 8) was carried out. It was found that KR2 in the  $S_1$  state deactivates with a time constant of 180 fs and relaxes to the J intermediate, indicating that the photoisomerization takes place with a time constant of 180 fs. This photoisomerization process in KR2 is several times faster than that in bacteriorhodopsin (500 fs). Based on the comparison of the chromophore structure of KR2 and bacteriorhodopsin, it was suggested that the difference in distortions of the Schiff base in KR2 and bacteriorhodopsin gives rise to the faster photoisomerization of KR2.

In chapter 5, pH dependence of the primary process of KR2 was examined by femtosecond time-resolved absorption measurements of KR2. The data showed that, upon the protonation of Asp 116 (the counterion of the PRSB), the yield of the reactive  $S_1$  state that generates the K intermediate decreases while the yields of the non-reactive  $S_1$  states that do not generate any photoproduct increase. This indicates that KR2's having the deprotonated and protonated Asp116 coexist in the  $S_0$  state, giving rise to the reactive and non-reactive  $S_1$  states by

photoexcitation, respectively. This indicates that the interaction between the PRSB and the Asp 116 plays a critical role in the initial isomerization process of KR2.

Through chapters 3, 4 and 5, it is concluded that the photoisomerization dynamics of the chromophore in the protein is significantly affected by the various factors such as the initial structure of the chromophore and the interaction with surroundings.

In chapter 6, it was demonstrated that the continuous structural change in the course of the photoisomerization process can be tracked based on the Raman pump wavelength dependence of the FSRS spectrum, taking a cyanine dye as an example.

In this dissertation, ultrafast spectroscopic studies of photoisomerization of two rhodopsins and a cyanine dye are described. It was shown that various factors influence the photoisomerization dynamics in rhodopsins. An approach using FSRS to track the structural change of “isomerizing” molecules was also described. In the latter part, in particular, observation of the structural dynamics on the barrierless excited-state potential energy surface, which is essentially equivalent to the structural change in the transition state in the chemical reactions, was successfully captured.

Although the experimental observation of the photoisomerization in general molecules using femtosecond spectroscopy is still challenging, the molecules undergoing barrierless photoisomerization, such as cyanine dyes, provide an opportunity to directly capture the molecule during the isomerization process and to obtain deep insight for the dynamics and mechanism of the photoisomerization processes. In addition, femtosecond vibrational spectroscopy that is sensitive to the change of molecular structure will provide information about the multidimensionality of isomerization reaction and involvement of nuclear coordinates other than the rotation of the C=C bond. Furthermore, it should be noted that understanding of the dynamics in the vicinity of the conical intersection is also very important, and ultrafast spectroscopy would provide us an opportunity to tackle this critically important but very difficult problem in understanding the mechanism of photoisomerization reactions

# List of Publications

## Original paper

Tahara, S.; Takeuchi, S.; Abe-Yoshizumi, R.; Inoue, K.; Ohtani, H.; Kandori, H.; Tahara, T. Ultrafast Photoreaction Dynamics of a Light-Driven Sodium-Ion-Pumping Retinal Protein from *Krokinobacter eikastus* Revealed by Femtosecond Time-Resolved Absorption Spectroscopy. *J. Phys. Chem. Lett.* **2015**, *6*, 4481-4486.

## Reference paper

Tahara, S.; Kato, Y.; Kandori, H.; Ohtani, H. pH-Dependent Photoreaction Pathway of the All-trans form of *Anabaena* Sensory Rhodopsin. *J. Phys. Chem. B* **2013**, *117*, 2053-60.

# Acknowledgements

This study was carried out under the supervisions of Prof. Hiroyuki Ohtani and Prof. Tahei Tahara. The author thanks them for providing an opportunity to accomplish this study.

The author also would like to thank Dr. Satoshi Takeuchi for his helpful suggestions and discussions. The author also has enjoyed many discussions with Dr. Hikaru Kuramochi and Dr. Tomotsumi Fujisawa.

The author learned about the preparation of the protein sample from Mr. Yoshitaka Kato, Mr. Takuya Ishimoto, Dr. Tatsuya Niwa, and Prof. Hideki Taguchi.

The KR2 samples were provided by Dr. Keiichi Inoue, Dr. Rei-Abe Yoshizumi and Prof. Hideki Kandori.

Finally, the author also would like to thank my parents Mrs. Keiko Tahara and now-dead Keiji Tahara for their encouragements and various supports.